ABSTRACT

Title of Dissertation: PASSIVE SCALAR DISPERSION IN A TURBULENT MIXING LAYER

Ning Li, Doctor of Philosophy, 2004

Dissertation directed by: Professor James M. Wallace
Department of Mechanical Engineering

Experimental and numerical studies of spatially developed turbulent mixing layers with passive scalar concentrations was performed. In the experiment, a mixing layer was created by an S-shaped splitter plate in a wind tunnel, with a velocity ratio of 2:1. A concentration field was realized by injecting incense smoke into the high-speed side of the mixing layer. Simultaneous measurements of the velocity, vorticity and concentration fields were performed.

A 12-sensor hot-wire probe was used to measure the velocity field and its gradients, while the concentration field was recorded by taking digital pictures of the laser-illuminated smoke. The statistics of the velocity and vorticity fields agree well with previous research. By synchronizing the velocity and concentration measurements, concentration fluxes were determined. Octant analysis was performed on the flux data to explore the scalar transport processes. Conditional planar average of flow properties was also performed to determine their spatial distribution with respect to the large-scale vortices.

A large-eddy simulation, designed to match the experimental conditions, was performed to provide three-dimensional pictures of the mixing layer. A new approach to effectively specify the inflow boundary condition was proposed. Passive particles were released and tracked to simulate the scalar concentration field. Numerical interpolation schemes were examined for performing the particle tracking tasks. The simulation statistically supported the experimental result while providing insight about the flow topology, from which scalar transport models by the rib vortices and roller vortices were proposed and examined.

PASSIVE SCALAR DISPERSION IN A TURBULENT MIXING LAYER

by

Ning Li

Dissertation submitted to the Faculty of the Graduate School of the
University of Maryland, College Park in partial fulfillment
of the requirements for the degree of
Doctor of Philosophy
2004

Advisory Committee:

Professor James M. Wallace, Chair/Advisor
Assistant Professor Elias Balaras, Co-Advisor
Professor Richard V. Calabrese
Professor James H. Duncan
Professor Ugo Piomelli

ACKNOWLEDGEMENTS

I would like to express my profound appreciation to my advisor, Prof. James Wallace, for giving me the opportunity to conduct the research project presented in this dissertation, for supporting me financially through my 5 years of life in Maryland, for his expert guidance and mentorship. He also kindly corrected this manuscript many times, bringing my written English into a much readable form.

Dr. Elias Balaras (co-advisor) opened the door of fantastic world of CFD for me. I owe my gratitude to him for his wonderful LES code and for his direct involvement in my simulations, without which this work wouldn't have been possible.

I would also like to thank Prof. Richard Calabrese, Prof. James Duncan and Prof. Ugo Piomelli for reading this dissertation and offering constructive comments. Special tribute should be paid to Prof. Piomelli for his very informative CFD course, one of the best graduate courses I have ever attended.

Dr. Jean-Yves Vinçont contributed to the present experimental study by constructing instruments and setting up the optic system. I was constantly amazed by his endless creative ideas.

My colleagues and friends in Maryland have enriched my graduate life in many ways. Dr. Xinan Liu and Mr. Jianming Yang, among others, deserve a special mention here for their regular inputs to my project, from thought-provoking ideas to reusable code snippets.

I had many fruitful discussions with Dr. Sylvain Lardeau, my new colleague at Imperial College London, who happened to work on a similar project for his

PhD study and has extensive expertise in the area of numerical simulations. I would like to use this opportunity to thank him for giving me inspiration as well.

Finally, I owe my deepest thanks to my parents and my wife who have always stood by me and supported me through difficult times. I would like to dedicate this work to my 95-year old grandpa, who helped my parents to raise me up and who was my first mathematics teacher.

TABLE OF CONTENTS

LIST OF TABLES

LIST OF FIGURES

Chapter 1

Introduction

The plane turbulent mixing layer is one of the most important types of turbulent flows in nature and engineering. For example, in combustion fuel and air are often mixed using a mixing layer configuration. This configuration is also widely used to perform chemical reactions. In nature, the Great Red Spot on Jupiter is known to be such flow as well.

The study of the turbulent mixing layer has been a frequent subject of turbulence research. As early as the 1970's, the prominent feature of this flow – the large-scale spanwise vortices, was discovered and described in several experimental studies [18],[19],[24],[79]. In the following decades, this flow has continued to be investigated both experimentally and numerically. However, due to the limitations of experimental techniques and computational power, much of this research only focused on the velocity field of this flow.

In the 1990's, with the availability of sufficiently resolved direct numerical simulations (DNS) and large eddy simulations (LES) and with the development of new experimental techniques, such as the technique that uses multi-sensor hot-wire probes to make simultaneous measurement of the velocity and vorticity

fields in turbulent flows, researchers began to obtain knowledge of the vorticity field of the turbulent mixing layer.

Another important property of the turbulent mixing layer is its ability to transport scalars. Although there have been many measurements and numerical simulations of the scalar concentration field itself, knowledge of higher order statistics, such as concentration fluxes, are very rare. The scalar fluxes are of primary importance for predictive models of scalar transport in this flow.

Objective

The purpose of the research project presented herein is to obtain a thorough knowledge of the velocity, vorticity and concentration fields of a turbulent mixing layer in order to gain insight into the scalar transport processes and their relationship to vortical structures of this flow. In particular, quantitative measurements of the turbulent fluxes of a passive scalar have been made and analyzed to determine how they are affected by these structures.

Both experimental and numerical approaches have been used. The experiments focused on simultaneous measurement of velocity, vorticity, scalar concentration and fluxes (using the multi-sensor hot-wire anemometry, flow visualization and image processing), while the numerical simulations (using LES and particle tracking) complemented the experimental studies by adding 3D pictures of those fields and enabling clear determination of the turbulence structures.

1.1 Literature Review

Experimental Studies

The large coherent mixing layer structures, which are spanwise vortices and are also called rollers, were first observed by Brown and Roshko [18] in the early 1970's in their experiment using the shadowgraph technique. They found that the vortices grow linearly as they move downstream, and that some rollers pair into larger vortices. The effect of density differences between the two streams on the flow properties, such as the spreading angle, was also investigated.

Winant and Browand [79] studied the vortex pairing process. They found that the vortices often rolled around each other and formed larger vortices. This process controlled the growth of the mixing layer. Based on their observations, a model for mixing-layer growth was also presented.

At fairly low Reynolds numbers, the coherent structures in the mixing layer can be easily visualized with properly designed experimental methods, as shown in Fig. 1.1 (from Loucks [45]). As the Reynolds number increases, the vortices are not as spatially coherent, making their direct visualization of flow structures more difficult. The question arises as to whether the large spanwise vortices exist in a high Reynolds number mixing layers.

Dimotakis and Brown [24] gave a positive answer to this question by studying the mixing layer flow at high Reynolds numbers[1] up to 3×10^6. They once again observed the existence of large coherent structures. This study proved that

[1]The authors used the high-speed free-stream velocity as the velocity scale and the distance from the splitter plate as the length scale. So this Reynolds number is comparable to Re_θ of about 1000.

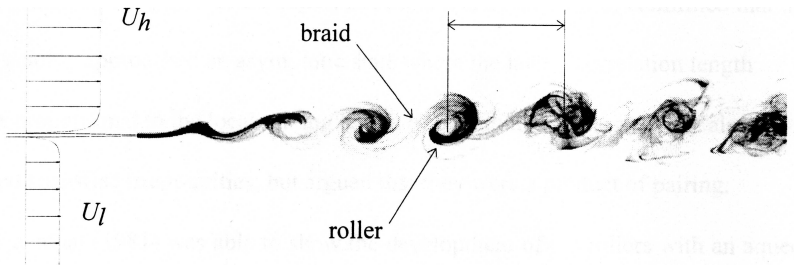

Figure 1.1: Visualization of a mixing layer.

the mixing layer dynamics are always coupled to the large structures. They also identified two distinct stages of the mixing: the entrainment across the boundaries of the shear layer, and the fine-scale mixing within those boundaries.

Chandrsuda, Mehta, Weir and Bradshaw [19] found that the formation of the coherent structures is highly influenced by the free-stream and inflow conditions, if the external flow is highly turbulent. They argued that the two-dimensional rollers were not a universal feature of the flow and three-dimensionality would be introduced at an early stage of transition.

Browand and Troutt [17] carried out an experiment with multiple hot-wire probes and confirmed that the rollers approached an asymptotic state by calculation of the spanwise correlations between different hot-wire signals. They also studied the spanwise irregularities and argued that they were produced by the pairing interactions between adjacent vortices.

Breidenthal [15] used a chemical reacting flow to study the mixing layer. By measuring the concentration of reaction product, the regions with high reaction production rates were identified and related to the large coherent structures and small-scale 3D motions of the flow. The Reynolds number and Schmidt number

effects on the flow were also studied. It was found that the mixing product was independent of the Reynolds number downstream of the transition.

Hernan and Jimenez [28] used digitized flow images to study the mixing layer. By analyzing a sequence of images, statistics of the life history of the eddies captured in the images was obtained. They found that the entrainment mostly occurs during the normal life of eddies, not during the pairing periods.

Ho and Huang [29] observed the evolution of the coherent structures under forced conditions. They showed that forcing at inflow at nearly a subharmonic frequency could change the growth rate of the rollers. Such forcing could make several vortices merging simultaneously and therefore dramatically increase the mixing.

Jimenez [31] found that the plane mixing layer develops a spanwise structure, due to the secondary instability of the flow. This secondary instability deforms the large spanwise rollers.

Using the LDV technique, Lang [38] measured the streamwise and cross-stream components of the velocity, as well as the spanwise vorticity and the Reynolds shear stress in a turbulent mixing layer.

The development of three-dimensional motions in a mixing layer was investigated by Bernal and Roshko [14]. They observed the secondary structures, i.e. streamwise vortices, by visualizing planes normal to the streamwise direction of the flow, using the laser-induced fluorescence technique. A topological model was proposed to illustrate the structures of the secondary vortices. The generation of such structures was related to the spanwise vortex instability.

Lasheras, Cho and Maxworthy [39] further studied these streamwise vortices and found that they were products of upstream perturbations. The vortices

were always seen to form in the braid regions, and their sizes are comparable to the prominent spanwise structures. Thus, they contribute substantially to the entrainment process.

In the 1990's, significantly improved experimental techniques made more accurate measurements of turbulent flow fields possible. Vukoslavčević, Wallace and Balint [75] developed a 9-sensor hot-wire probe with good spatial resolution for turbulent flows at moderate Reynolds numbers. It is capable of simultaneous measurement of both the velocity and the vorticity fields of turbulent flows. This probe was successfully applied [9] in a turbulent boundary layer flow, and the statistical properties obtained from the measurement compared very well with other laboratory measurements and numerical simulations.

This technique later evolved into a more sophisticated 12-sensor probe [76], which Loucks [45] used to perform measurement of the full velocity and vorticity fields of a turbulent mixing layer. This was an extensive study at several streamwise locations and thus at different Reynolds numbers. Statistical analysis of various physical variables such as velocity, Reynolds stress, turbulent kinetic energy, vorticity, enstrophy and dissipation rate was presented. Probability analysis was performed on the velocity and vorticity fields. Also presented was the conditional analysis of a set of physical variables to rebuild the spatial information of the flow. The current study shares the same instrumentation as this experiment, with the added ability to conduct scalar concentration measurements.

Bell and Mehta [11] studied the development of mixing layers with both tripped and untripped initial conditions. The growth rate of the layer for the untripped case was found to be higher than the tripped case. However, each case still appeared to be self-similar after some development length. In a later

study [12], they used the same experimental techniques to observe the streamwise vortices in the mixing layer. This was a comprehensive work that provided a quantitative description of many aspects of the streamwise vortices, including their origin, evolution and persistence. Bell, Plensniak and Mehta [13] further studied the effect of streamwise vortices on global properties of the mixing layer, such as momentum thickness and peak values of velocity variances.

Chemical reaction has been used to study the mixing layer, but experimental studies of the scalar field itself are relatively rare. Based on their experimental observations, Broadwell and Breidenthal [16] proposed a model for treating molecular mixing and chemical reaction in the mixing layer flow, as a replacement of the gradient diffusion models. Koochesfahani and Dimotakis [36] described an investigation of entrainment mixing in reacting and nonreacting (with passive scalar) flows at large Schmidt numbers. The mixed fluid composition was studied. The Schmidt number was shown to play an important role in such flows.

In recent years, improved experimental techniques have made possible more complex experiments. As an example, Koochesfahani, Cohn and MacKinnon [34] developed a "single-laser, two-tracer" approach for the simultaneous measurement of velocity and concentration fields in fluid flows. This was successfully applied to a turbulent mixing layer, and correlations between velocity and concentration fluctuations were obtained.

Pickett and Ghandhi [54] made quantitative passive scalar measurements in an incompressible planar mixing layer using planar laser-induced fluorescence of acetone seeded into one side of the layer. This experiment discovered a preferred mixture composition favoring the high-speed fluid. They [55] also studied the effect of inlet conditions on the mixing of a passive scalar.

Numerical Simulations

Corcos and Sherman [22] attempted to use a hierarchy of motions to model the evolution of rollers in a 2D plane to represent the fundamental stochastic properties of the mixing layer. Based on this model, a related work by Corcos and Lin [23] provided a detailed description of the 3D motions and streamwise vorticity and their effects on the 2D flows. They showed that the characteristics of the 3D motions were dictated by the distribution of spanwise vorticity which resulted from roll-up and pairing.

Ashurst and Meiburg [4] simulated a temporally developing shear layer using a discrete vortex method with a specially designed method to match the inflow condition of experimental studies. This achieved close agreement with experimental results. Their simulation showed the formation of concentrated streamwise vortices in the braid region of the mixing layer. They also found that the processes dominating the early stage of the mixing-layer development can be understood in terms of inviscid vortex dynamics.

Ghoniem and Heidarinejad [27] simulated a 2D spatially developing reacting shear layer and investigated the effect of the flow field on the reaction rate. Results revealed a strong similarity between the distribution of product concentration and vorticity. It was found that the product formation is strongly governed by the entrainment field.

In earlier decades, due to the limitation of computational power, numerical studies of turbulent mixing layers were mostly performed using analytical methods on relatively simple models, most of them 2D. With the advent of more powerful computers, direct numerical simulations with sufficient spacial resolu-

tion and large eddy simulations became more popular tools for turbulence studies. There have been several such simulations performed for mixing layers.

Moser and Rogers [48],[49] performed several Direct Numerical Simulations (DNS) of temporally developing[2] mixing layers. They used a variety of initial conditions as well as different amplitude perturbations to the mean flow to study the development of three-dimensionality and the transition to turbulence. Through these studies, many phenomena observed by previous experimental studies were confirmed. It was found that streamwise vortices were part of the initial cascade to small-scale turbulence. The pairing process inhibited the growth of three-dimensional disturbances. When the flow reached the self-similar stage, the streamwise vortices were absent.

Again using DNS, Rogers and Moser [61],[62] studied the three-dimensional evolution of temporal mixing layers in great detail. Using boundary layer DNS data [68] as inflow, they performed three DNS of the mixing layer: one base case with no disturbance, one with weak forcing and one with strong forcing. Results indicated that the base case and the weak disturbance case both reached self-similarity, which was characterized by a lack of large-scale pairing, a lack of streamwise vortices in the braid region and 'marching' PDFs of scalar mixing. In contrast, the strong disturbance case exhibited sustained large-scale pairing, well defined streamwise rib vortices and 'non-marching' scalar PDFs. This set of studies provided considerable information about the vortical structures of the

[2]Temporal simulations are widely used to study the mixing layer flow to avoid the difficulties associated with the imposition of inflow conditions (periodic boundary condition can be applied in the streamwise direction in the temporal simulations) and the computational cost due to the significant length of computational domain required to develop self-similar states.

flow, as well as the physical mechanism behind it.

Balaras, Piomelli and Wallace [7] performed large eddy simulations of temporally evolving turbulent mixing layers. The effect of different initial conditions (one case using turbulent boundary layer data and one case using mean flow plus random perturbations with prescribed moments) and the size of the computational box on the turbulent statistics and structures was examined. In all cases, self-similar states were reached. However, the growth rates and turbulence intensities of the mixing layer, as well as the turbulent structures were affected by the different initial conditions.

1.2 Thesis Synopsis

The introduction of turbulent mixing layer flow, the reviews and summaries of relevant studies and the research objectives have been presented so far. The outline of the rest of this dissertation is as follows:

- Chapter 2 is an overview of the experimental studies. The design idea, the experimental facilities and procedures are first documented. Then the calibration and data reduction methods for the hot-wire measurements are covered in detail. In the end the mixing layer characteristics are briefly described.

- In Chapter 3 the general idea, numerical method and procedure of large-eddy simulation are first covered. Then two crucial topics of the current study are discussed: the specification of realistic inflow boundary conditions for the LES, and the particle tracking method to study the scalar transport.

The numerical implementation details are documented. Finally the mixing layer integral properties are discussed.

- Chapter 4 presents all the experimental and LES results. The velocity, vorticity, scalar concentration and concentration flux fields are first observed from a statistical point of view. Then, in an effort to reconstruct the underlying flow structure from the experimental data, conditional analysis was performed. Finally visualization and analysis of the instantaneous LES flow structures were conducted. Discussions about the scalar transport mechanism is scattered throughout this chapter and summarized at its end.

- The dissertation is concluded by chapter 5.

Chapter 2

Experimental Design, Facility, Instrumentation and Procedures

The goal of the experimental part of this research is to make high quality measurements of the velocity and scalar concentration fields in a turbulent mixing layer. The velocity field in the self-similar region of the mixing layer and the concentration field of a smoke scalar were measured simultaneously at the same spatial locations, so that the physics underlying turbulent scalar transport could be explored.

This chapter introduces the design of the experiment, documents the experimental facilities and procedures, and discusses the data acquisition and data reduction methods. The experimental results will be shown and discussed in Chapter 3.

2.1 Experimental Configuration and Wind Tunnel Facility

The experiment was conducted in the low-speed wind tunnel of the Turbulence Research Laboratory at University of Maryland, College Park. It is shown in Fig. 2.1. The open-return type of wind tunnel was built in two adjacent rooms with a blower between the rooms driving the air flow. The tunnel has a test cross-section of $1.26m \times 0.63m$. The free-stream velocity can be selected and controlled within the range of $0.5m/s - 5.5m/s$. The three walls of the wind tunnel are smooth wood surfaces, with one vertical side of the test section made of plexiglass for visualization purposes. There is a rail system along the streamwise direction at the top corners of the tunnel. It was designed so that the probe support and traversing mechanism could travel along it conveniently. There are also stepper motor systems that allow the hot-wire probe to be moved automatically in the cross-stream vertical and spanwise directions. They are controlled by a computer system so that very little human intervention is needed.

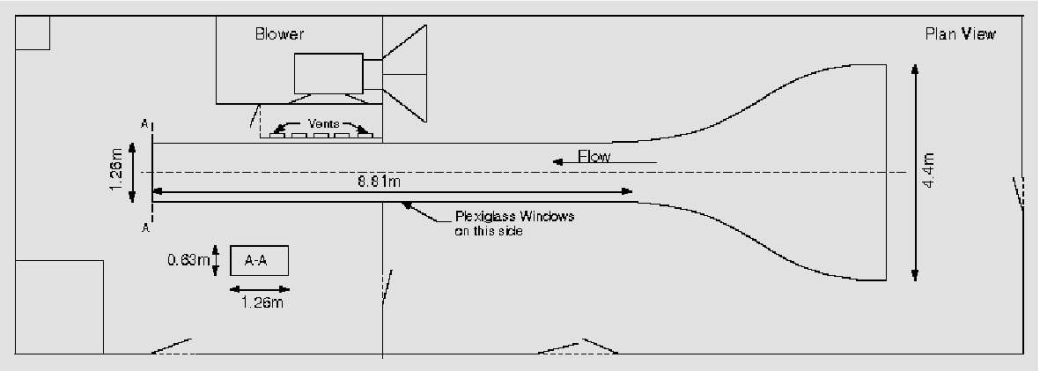

Figure 2.1: Low-speed wind tunnel.

The configuration of the experiment in the test section is shown in Fig. 2.2. Two major components of the experimental system are the devices for forming a plane mixing layer and devices for generating smoke concentrations.

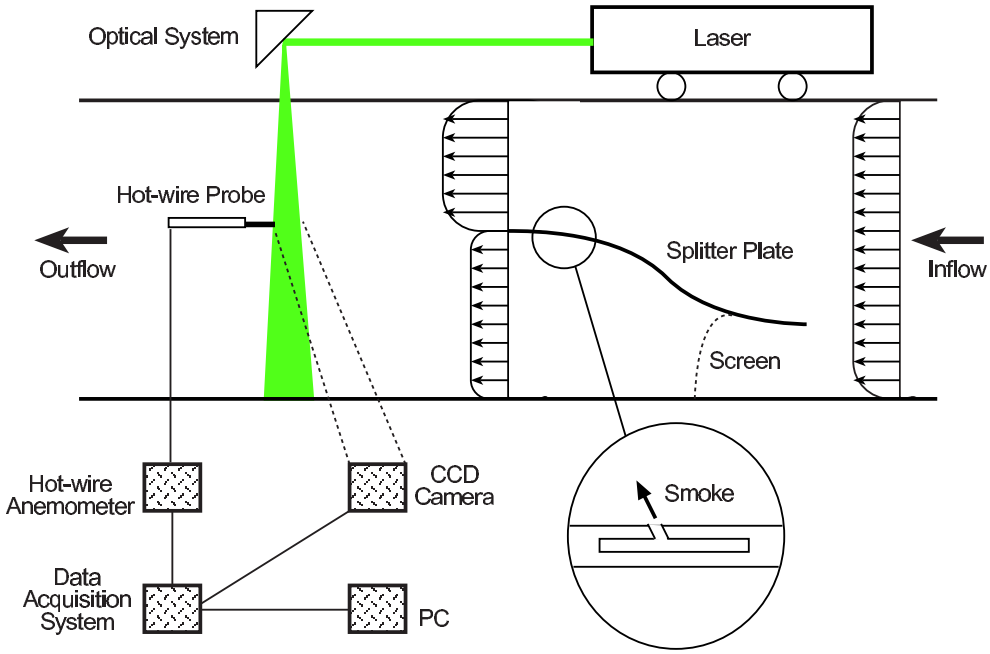

Figure 2.2: Mixing layer experiment configurations.

A curved splitter plate was built into the wind tunnel. This idea was developed by Lang [38]. It was adopted and further developed in the Turbulence Research Laboratory. The splitter plate divides the wind tunnel, accelerating the flow on one side and decelerating the flow on the other side. The trailing edge of the splitter plate provides a smooth meeting of two turbulent boundary layers and creates a mixing layer with a velocity ratio of about 2:1. There is a screen on the low-speed side to balance the pressure of the flow in the cross-stream direction,

eliminating the possible vertical mean velocity and separation at the trailing edge of the splitter plate.

The splitter plate was designed and constructed with a small slot on the upper surface from which smoke could be released into the high-speed-side splitter plate boundary layer. The smoke arrives at the gap through ports on the side wall of the tunnel, where the splitter plate was fixed to the tunnel. With the smoke illuminated by a laser beam, photos containing varying light intensity, and thus varying concentration information could be taken.

2.2 Smoke Concentration Generation

The smoke was generated by burning Chinese incense. Such incense is widely used in eastern countries for religious purposes and for refreshing air at indoor places where ventilation is poor. It is non-toxic and safe to use in a lab environment. Also, it was determined [20] that the sizes of the incense smoke particles are suitable for this experiment, ranging from 0.12 to 2.87μm. On the one hand, these particles are small enough so that they faithfully follow the turbulent motions[1]. They can be considered as passive, or just markers in the fluid, without significant influence on the fluid flow. On the other hand, they are still big enough to reflect enough light for the visualization and photography.

The device for generating smoke is shown in Fig. 2.3. Smoke was generated by burning coils of incense in a container. The smoke was driven by compressed

[1]According to [73], an estimate of the mean particle response time to a step change in velocity is only about $5 \times 10^7 sec$. The inertial forces on the particles can be safely ignored.

air[2], filtered to remove tars (which otherwise could possibly stick to the hot-wire sensors and affect their sensitivity) and cooled down to the ambient temperature through a heat exchanger, before it entered the wind tunnel.

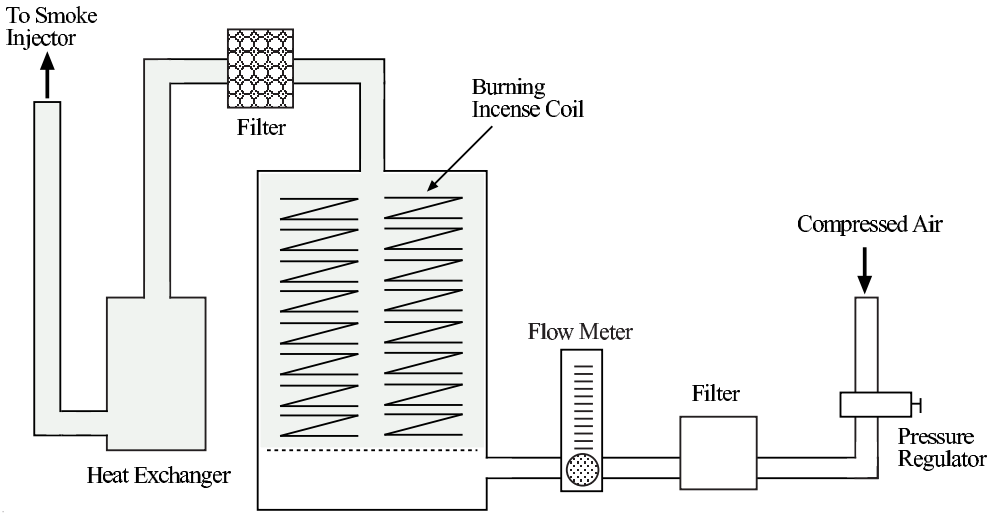

Figure 2.3: Smoke generation devices.

To minimize most of the recirculation of smoke through the laboratory room and back into the tunnel, a suction system was mounted at the end of the tunnel to draw in the smoke and pass it through a very fine filter to remove most of the particles.

[2]This did not excessively perturb the high-speed side boundary layer as the velocity measurement at the trailing edge of the splitter plate showed normal boundary layer behavior, as can be seen in Fig. 2.15.

2.3 Laser and Optical System

To illuminate the smoke, an Oxford Lasers CU15-A model Copper Vapor Laser system was used. The laser light output is a mixture of green and yellow, with wave lengths of $510nm$ and $578nm$, respectively. The maximum power is 15W. The system consists of a laser generation part and a power supply component.

Originally, the laser was place at a downstream location of the wind tunnel. In this arrangement, the light had to travel through the smoke for a long distance before it reached the testing area, greatly reducing the light intensity at the test section. To reduce the loss of light intensity, the laser was moved to a position on top of the wind tunnel just above the test section so that the laser beam only entered the smoke at the test section, as illustrated in Fig 2.2.

The test section was located about 2 meters downstream of the splitter plate trailing edge, where a hole was made in the ceiling of the wind tunnel and the laser beam was directed into the tunnel by an optical system. This streamwise location is well into the self-similar region of the mixing layer, as determined in an earlier experiment [45]. To approximate a concentration plane, a two-dimensional light sheet as thin as possible was needed in this experiment. The laser beam originally had a round shape at the exit of the laser. The optical system consisted of a set of lenses, mirrors and filters, which created the planar light. The light sheet was just a few millimeters thick in the spanwise direction. It illuminated a trapezoidal area covering the neighborhood of the locations for the velocity measurements. Fig 2.4 shows a schematic of the optical system.

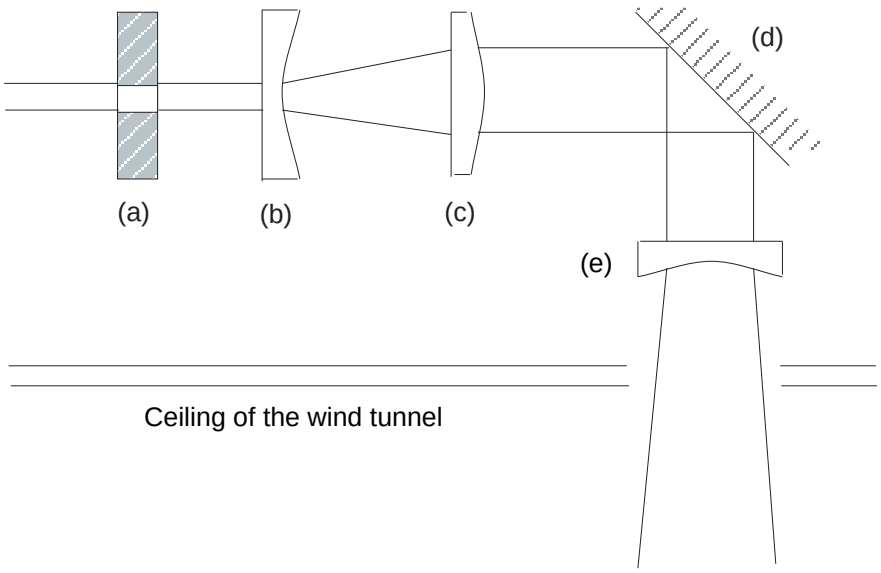

Figure 2.4: Optical system to generate a 2D light sheet to illuminate the smoke. (a) Filter to change the round beam into a light sheet. (b) and (c) Convex and concave lenses to widen the light sheet. (d) Mirror to redirect the light into the wind tunnel. (e) Concave lens to change the shape of the light sheet.

2.4 Digital Camera and Image Acquisition System

With this configuration, photos containing concentration information were taken by a KODAK megaplus ES 1.0 model digital camera. This CCD camera has an effective pixel array of $1,008$ (horizontal) $\times 1,018$ (vertical) with a progressive scan readout system. It is capable of taking pictures at a speed of up to 30 frames/second. The digital output is an eight bit gray scale with 256 levels. The gray scale values acquired from the pictures, above a base threshold, have been shown [73] to be a good representation of the light intensity scattered by the smoke, which in turn is related to the smoke concentration. The camera can be operated in a single frame, continuous, or double frame triggering mode. The continuous mode was appropriate for our purpose of capturing real-time images for a period of time. The double frame triggering mode, on the other hand, is perfect for PIV experiments where two consecutive images need to be correlated to determine particle movements.

With a ROAD RUNNER data acquisition card from BitFlow Inc., the digital images could be captured and stored in the memory of a PC for later processing. ROAD RUNNER is a reliable, high-performance digital camera interface card for digital imaging applications. It has a standard $32-bit/33MHz$ PCI interface to connect to a PC, and it has a $32-bit/RS422$ interface to connect to various types of digital cameras. It functions well with all versions of BitFlow SDK software so many hardware level configurations are programmable and controllable. The data storage PC for the present experiment was a Pentium II system with a 400MHz CPU, a 512M memory, and it runs Windows NT. It allowed us to store

up to 400 images at a time in the system memory. With the help of the associated image processing software (Video Savant), the digital images could be converted into various image formats and saved on hard disks as image files. The Windows Bitmap format was used for this experiment because it retains all the image information while encoding the image data.

The camera has a nearly constant sampling frequency (about $30Hz$). The laser system has an adjustable pulse repetition frequency range from as low as $2KHz$ to as high as $20KHz$. It was set to run at a frequency that is a multiple of the camera frequency ($3KHz$). Thus, at each image acquisition, a laser pulse was almost guaranteed to illuminate the smoke field. The short duration (1/3000 seconds) of the laser pulse minimized the blurring effect caused by the moving smoke, and clear, crispy images were obtained. Occasionally, a dark image was captured because the timing was not perfectly synchronized. However, this was very rare, no more that 5 instances for every $1,200$ pictures in the experiment, and could be easily handled with post-processing.

Another nice feature of this camera is that it can send a signal indicating its operational status. This signal contains a pulse corresponding to each picture the camera takes. The data acquisition system could record this signal along with the hot-wire signals. (see Fig. 4.8 in Chapter 4). By reading this signal and identifying the pulses, a computer program can easily synchronize the velocity, vorticity and scalar concentration information obtained in the experiment, and thus calculate the concentration fluxes, $\overline{uc}$ and $\overline{vc}$, and other correlations.

One more feature that affected our post-processing is also worth mentioning here. When operating at its highest speed, the camera transfers data out simultaneously via two data channels. One channel transfers the odd lines of the

images and the other channel transfers the even lines, i.e. the image output is interlaced. Normally, this would not be a problem because the associated image-processing software (Video Savant V3.0) knows how to rearrange the pixels and reassemble the image. However, in this experiment, the background gray levels of the two channels were slightly different. If we were to take a picture of a piece of white paper with the camera and export one column of pixels, we would have seen a zigzag change of gray values instead of the expected constant value. This problem was not discovered until the post-processing stage. It could be caused by the different noise levels the two channels experienced or for other reasons. Fortunately, this could be treated as a fixed system error and easily removed in post-processing.

2.5 12-sensor Hot-wire Probe, Anemometer and Data Acquisition Devices

A unique 12-sensor hot-wire probe developed earlier in the Turbulence Research Laboratory of University of Maryland was used to measure the velocity and vorticity fields [76]. The probe, shown in Fig. 2.5, consists of three 4-sensor arrays. Each array consists of four individual sensors oriented at approximately 45 degrees to the mean flow.

This probe is capable of measuring all three velocity components as well as six out of nine velocity gradients. The velocity measurement is possible from the directional sensitivity of the sensors. Actually, each 4-sensor array individually is enough to measure the velocity components. The redundancy provides extra

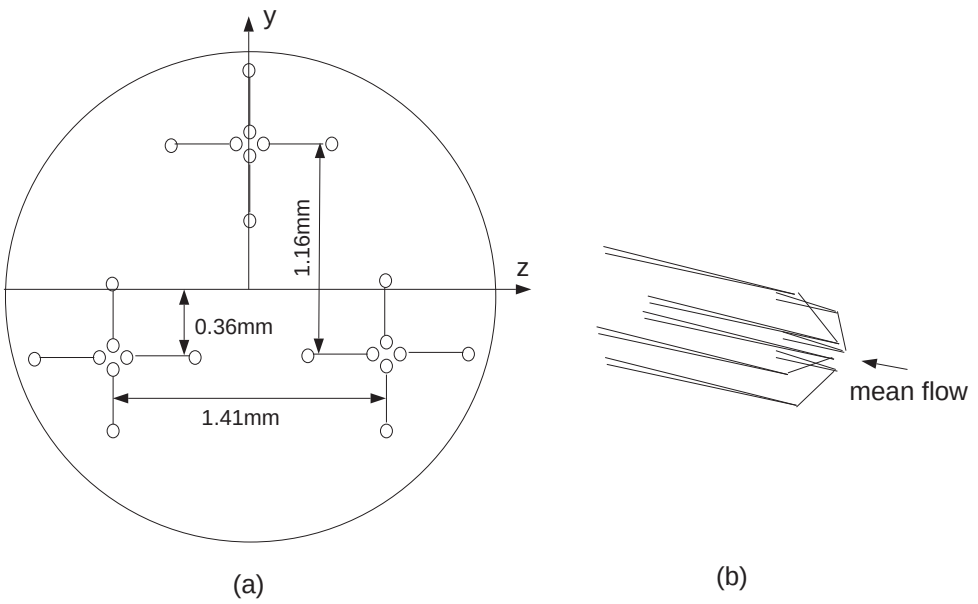

Figure 2.5: Schematic of 12-sensor hot-wire probe. (a) Front view, (b) Perspective view of one four-sensor array.

information for optimizing the velocity measurements and improving their accuracy. The additional sensors also enable the determination of the six velocity gradients in the cross-stream plane. The gradients are determined by expanding velocity vectors sensed at each wire in a Taylor's series about the geometric center of the probe front plane and solving a set of over-determined non-linear algebra equations. This technique is discussed in detail later in section 2.9. The remaining three (streamwise) velocity gradients can be estimated using Taylor's hypothesis, which is considered to be a fairly good approximation in experiments with enough temporal resolution and in which the turbulence intensity is not too high. The validity of this hypothesis is briefly discussed in section 4.2, as well as in [56] and [45]. Higher order velocity component statistics and important turbulence properties that depend on velocity gradients, such as vorticity, strain rate and dissipation rate, can be easily calculated from the information obtained from this probe.

The hot-wire probe was operated by an A. A. Lab AN-1003 model anemometry system. This is a constant temperature anemometer with 12 analog input channels. Each channel incorporates a standard Wheatstone-bridge type circuit. An overheat ratio of 1.2 was set for these measurements based on previous experience [45]. The raw voltage signals from the 12 channels were acquired using an OPTIM Megadac 5017A data acquisition system. This system has a 250 kHz 16-bit A/D converter, 32 simultaneous input channels, 64 megabytes of memory and an external 1 gigabyte optical disk storage. A thermocouple was used continuously to monitor the temperature changes in the wind tunnel. This information is necessary because temperature variation during the experiment must be taken into account calibrating of the hot-wire sensors and performing data

reduction. As mentioned before, the digital camera's operational status can be also monitored by recording a signal coming from the camera's back panel. These additional channels of data were also recorded by the OPTIM data acquisition system. The data sampling rate was set to $3KHz$. The acquisition system was interfaced with and controlled by an IBM PC, which also served as the data storage device. This PC is separate from the PC for image capturing and processing.

A set of software came with the data acquisition system which helped us control the system and process the data acquired. One significant issue raised by this system is that it saves raw data in a very special binary format. This format is not any of the standard binary formats on most PC/UNIX platforms. A conversion program is provided by OPTIM to convert such binary data into SUN binary. The storage logic (i.e. in which sequences multiple channels of data were written) of binary data in SUN format is well documented, so post-processing easily can be done based on it. The conversion program was compiled for a SUN computer, and no source code is available, so it has to run on a SUN computer (a SUN Sparc Station 10 system in the current research).

This sort of binary format incompatibility posed a great challenge throughout the data processing stage. Post-processing programs were written in different programming languages (such as FORTRAN, C, IDL and Java) on different computer systems where appropriate. Even the same source code might compile to different executables on different computers. For ultimate convenience, all the experimental data files were converted to human readable ASCII formats whenever possible, so that no confusion remained.

2.6 Calibration Devices

For the preliminary single-sensor hot-wire measurements, the calibration device is relatively simple. The only device needed is a jet that generates uniform velocity flows at the exit of its nozzle. The jet used has a motor driven by a power supply to generate the flow. The jet speed as a function of power supply voltage was calibrated first, using the system sketched in Fig. 2.6.

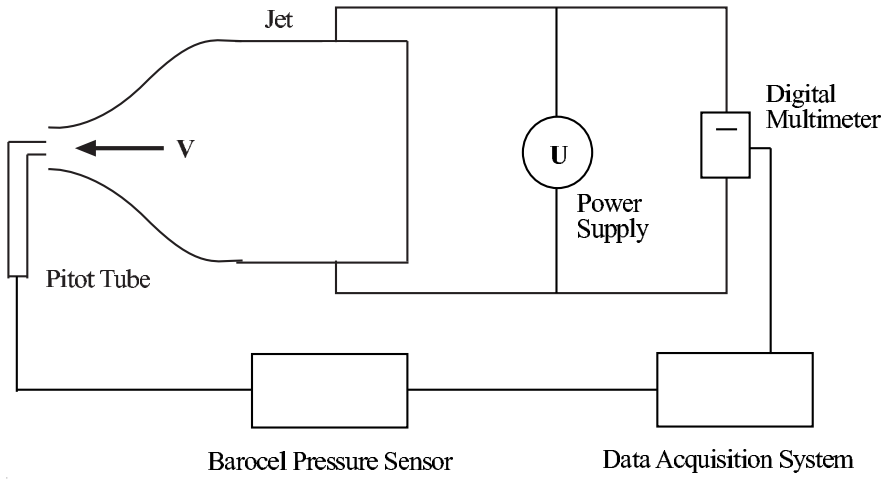

Figure 2.6: Jet calibration system.

A Pitot tube was used to calibrate the jet. An accurate Barocel pressure sensor was used to measure the difference between total pressure and static pressure of the Pitot tube. A digital multimeter was used to monitor the voltage. For better accuracy during the actual experiment, both the pressure difference and the voltage were sampled by the data acquisition system. A linear curve fit easily described the relationship between the jet nozzle exit velocity and the power supply voltage. After this step, the calibration jet was used to calibrate the

single-sensor hot-wire.

The calibration of the 12-sensor hot-wire is much more complex and is described in section 2.8.

2.7 Experimental Procedures

Several exploratory experiments with a single-sensor hot-wire probe were performed first. Streamwise mean velocity profiles of the mixing layer were measured. This preliminary work was to ensure that the wind tunnel and smoke generation devices were in good working condition, and the computer and data acquisition system were functioning properly. The post-processing procedure was established and tested with these relatively simpler data sets. The preliminary experiments also provided basic understanding of the mixing layer. The growth of the momentum thickness, the Reynolds number of the flow and other properties were estimated. These results were valuable in setting up the numerical simulations, as discussed in later chapters.

The definitive experiment followed these steps:

- All devices were set up and tested. The laser system was turned on and warmed up for about an hour.
- The 12-sensor hot-wire probe was exposed to multiple flow conditions generated by the specially designed calibration jet for calibration (see section 2.8 for more details).
- The wind tunnel was turned on and incense was ignited in the burner shown in Fig. 2.3 to generate smoke.

- The hot-wire probe was traversed through 15 cross-stream locations to perform velocity and velocity gradient measurements in the mixing layer flow. At the same time, digital images were taken by the camera, with the narrow laser light sheet just adjacent to the probe tip (see Fig. 2.2), to record concentration information.

- To accumulate long enough data records, the above measurements (three minutes long each) were repeated three times at each position. The PC only allowed 400 images to be stored in its memory. So a total number of 1200 images were accumulated for each cross-stream position.

- The wind tunnel was shut down. The 12-sensor hot-wire probe was recalibrated two more times, using the same set of calibration flow conditions.

The final run of the experiment took almost 15 hours and three people were involved. One was in charge of operating the data acquisition system to record hot-wire data on one PC. One was responsible for operating the digital camera for concentration measurements on a second PC. The third person had to adjust the hot-wire probe, monitor the data acquisition and coordinate the complete procedure.

The calibration process is discussed in Section 2.8. The measurements at the 15 locations involved the following operations:

- The hot-wire probe was driven by a stepper motor to move to the predefined cross-stream locations. Then the probe was moved manually and slightly forward in the streamwise direction to the edge of the laser light sheet (the probe support is on a rail attached to the wind tunnel to make this

possible). This step was needed because the edge of the light sheet was not perfectly vertical, due to the design of the optical system. Care was taken so that the tip of the hot-wire probe was only one pixel away from the light. This was monitored on a computer screen. If the probe was too close to the laser, the heat generated by the laser could change the sensor's response to the fluid flow. On the other hand, if the probe was too far away from the light, the velocity measurements and concentration measurements would be spatially separated, which was undesirable because velocity and concentration correlations were the main reason for these experiments.

- The hot-wire data was sampled at each location for a period of three minutes. The sampling frequency was 1000 Hz. The length of the sample proved to be more than enough to accurately calculate statistics of the velocity and vorticity fields.

- During the 3 minutes sampling period, 1200 digital images of the concentration field were taken by the CCD camera. This operation lasted about 40 seconds. The number of images available is limited by the computer hardware and image capturing hardware. So the synchronized velocity and concentration data was only available over less than a quarter of the 3 minutes period.

In the following sections, the hot-wire calibration process and data reduction process will be discussed in more detail.

2.8 Hot-wire Calibration Techniques

The hot-wire is a tiny, electrically heated metal element that is immersed in the fluid. It has been widely used to measure fluid properties for many years, especially velocity components of turbulent air flows.

The most common mode of hot-wire operation is the constant temperature mode. The sensor's electrical resistance will change as a function of the wire's temperature. By making the sensor one leg of a Wheatstone electrical bridge, and with a properly designed electrical circuit, the sensor can be maintained at a constant temperature, even while the air flowing over it will try to cool it at variable rates depending on the instantaneous velocity. The bridge voltage is constantly adjusted by the feedback characteristics of the circuit to keep the temperature constant. By recording the change of this bridge voltage, the change of flow velocity can be determined.

2.8.1 Single-sensor hot-wire calibration

Generally, the hot-wire's response to the velocity can be approximated by King's Law:

$$E^2 = A + BU^n, \tag{2.1}$$

where E is the voltage across the wire, U is the instantaneous velocity component normal to the sensor, and A, B and n are constants, which need to be determined through a calibration process.

The calibration of a single-sensor hot-wire is very straight-forward. The sensor is exposed to a variable predetermined steady, uniform and irrotational flow normal to it, and the voltage across the sensor is recorded. In practice, the non-

linear relationship between E and U is rather smooth, and a polynomial fit can be a good alternative to equation 2.1. Fig. 2.7 is a typical hot-wire calibration curve.

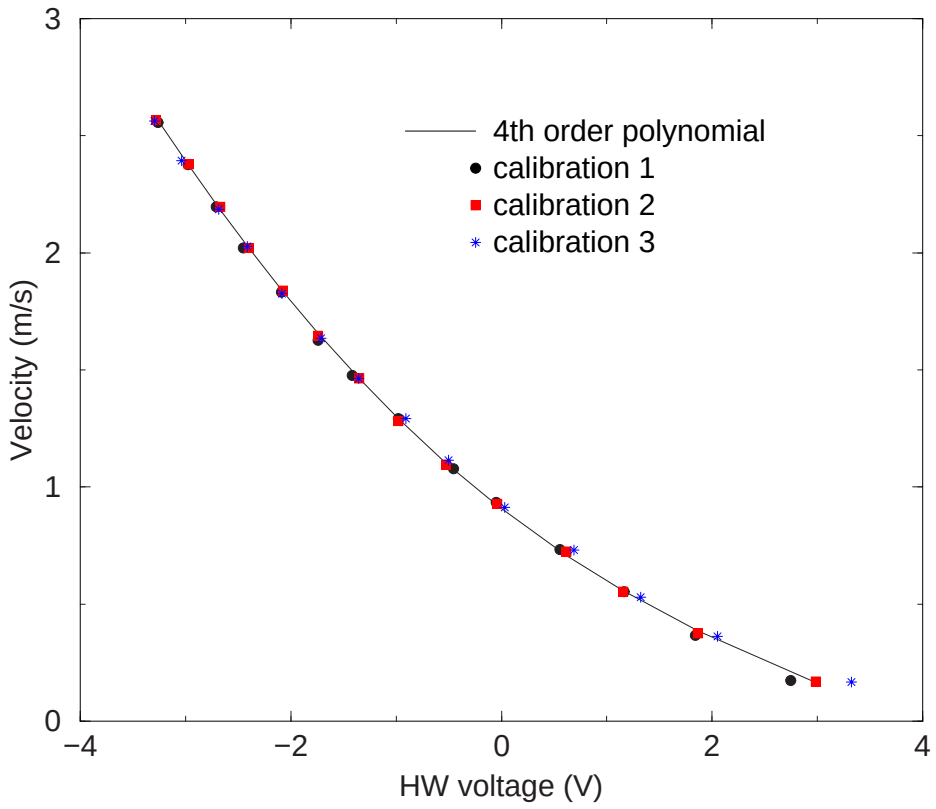

Figure 2.7: A typical hot-wire calibration curve.

The calibration device used in this experiment is the air-flow jet previously described, which responds linearly to the power supply voltage. It is able to generate a uniform velocity profile at its nozzle outlet in the speed range of $0 - 5m/s$. By placing the hot-wire probe just at the exit of the jet and carefully aligning its orientation (so that flow direction is normal to the sensor), calibration

can be performed.

2.8.2 12-sensor hot-wire calibration

The calibration of the 12-sensor probe is much more complex because the sensors have different orientations to the flow. Recalling that in (2.1) U is the velocity component normal to the wire, for the 12-sensor probe configuration the wires are not only oriented with angles not normal to the mean flow, but they also are very small. It would be very difficult to measure those angles directly and accurately in an experiment to determine those normal directions. Because of these difficulties, a more complex, but quite effective calibration method was used. Note that the procedure discussed below is applicable to any set of sensors which are not normal to the direction of the flow, not just those of the 12-sensor probe used in present experiment.

The starting point of our calibration procedure is Jorgenson's cooling law [32], which expresses what is known as the effective cooling velocity as a non-linear function of three orthogonal velocity components, i.e.

$$U_{eff}^2 = U_N^2 + C_T U_T^2 + C_B U_B^2, \tag{2.2}$$

where U_N, U_T and U_B denote the normal, tangential and bi-normal components of the cooling velocity with respect to the sensor, and C_T and C_B are the tangential and bi-normal cooling coefficients, respectively. These three directions are shown in Fig. 2.8 (a).

A more convenient coordinate system to use is one aligned with the wind tunnel and the probe axes, as shown in Fig. 2.8 (b). The two coordinate systems can be related through a geometric transformation, so that the velocity components

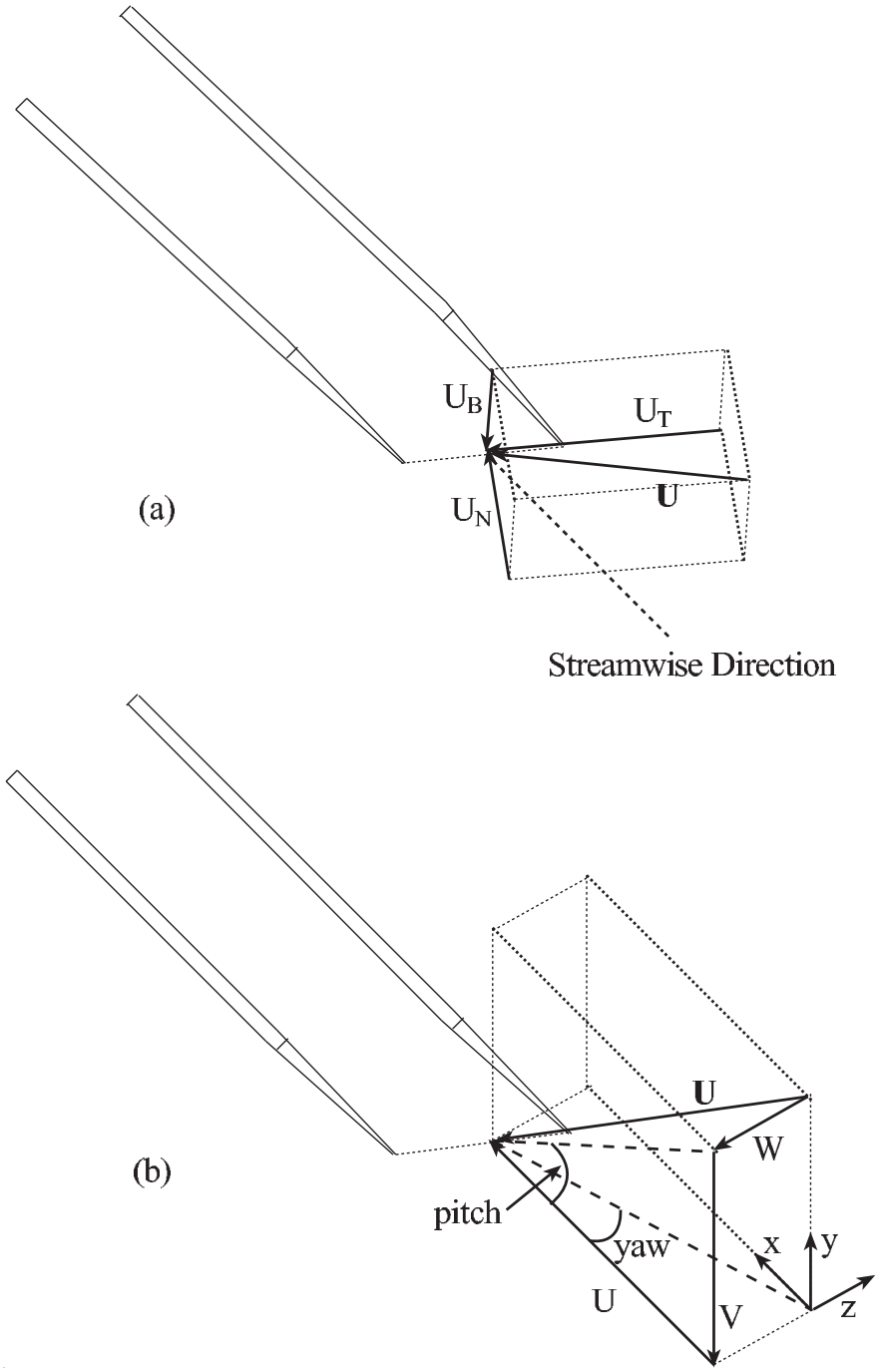

Figure 2.8: Two coordinate systems: (a) with respect to the sensor. (b) with respect to the wind tunnel and probe axes.

U_N, U_T and U_B can be rewritten as:

$$U_N = n_1 U + n_2 V + n_3 W \tag{2.3}$$

$$U_T = t_1 U + t_2 V + t_3 W \tag{2.4}$$

$$U_B = b_1 U + b_2 V + b_3 W, \tag{2.5}$$

where U, V and W are the three velocity components in the wind tunnel's coordinate system in the streamwise, cross-stream and spanwise directions, and n_i, t_i and $b_i (i = 1, 2, 3)$ are the geometric transformation coefficients. Again, due to the small size of the probe, it is very hard to measure the length and orientation of each sensor precisely enough to determine the transformation coefficients directly. It is generally much easier to combine these coefficients with the cooling velocity coefficients C_T and C_B in (2.2) and determine these combined coefficients indirectly by calibration.

As mentioned above, the relationship between the effective cooling velocity and the hot-wire voltage can be well approximated with a fourth order polynomial.

$$U_{eff}^2 = A_1 + A_2 E + A_3 E^2 + A_4 E^3 + A_5 E^4, \tag{2.6}$$

where A_1 through A_5 are coefficients of each sensor to be determined from the calibration. Substituting (2.3) - (2.5) into the Jorgensen's cooling law (2.2) and combining the constants yields:

$$U_{eff}^2 = U^2 + A_6 V^2 + A_7 W^2 + A_8 UV + A_9 UW + A_{10} VW, \tag{2.7}$$

with A_6 through A_{10} to be determined from the calibration process.

During a calibration, U, V and W in (2.7) are known from knowledge of the calibration jet's velocity and orientation (refer to equation (2.11) - (2.13)), and E

in (2.6) is the measured anemometer circuit's bridge output voltage. By applying the least square method to minimize the difference between equation (2.7) and (2.6), all ten coefficients $A_1 ... A_{10}$ can be determined. This is done by solving a 10 by 10 linear algebraic equation system in the form of $A\vec{x} = \vec{b}$, where the matrix[3] is:

$$A = \begin{bmatrix}
N_c & \overline{E} & \overline{E^2} & \overline{E^3} & \overline{E^4} & -\overline{V^2} & -\overline{W^2} & -\overline{UV} & -\overline{UW} & -\overline{VW} \\
\overline{E} & \overline{E^2} & \overline{E^3} & \overline{E^4} & \overline{E^5} & -\overline{EV^2} & -\overline{EW^2} & -\overline{EUV} & -\overline{EUW} & -\overline{EVW} \\
\overline{E^2} & \overline{E^3} & \overline{E^4} & \overline{E^5} & \overline{E^6} & -\overline{E^2V^2} & -\overline{E^2W^2} & -\overline{E^2UV} & -\overline{E^2UW} & -\overline{E^2VW} \\
\overline{E^3} & \overline{E^4} & \overline{E^5} & \overline{E^6} & \overline{E^7} & -\overline{E^3V^2} & -\overline{E^3W^2} & -\overline{E^3UV} & -\overline{E^3UW} & -\overline{E^3VW} \\
\overline{E^4} & \overline{E^5} & \overline{E^6} & \overline{E^7} & \overline{E^8} & -\overline{E^4V^2} & -\overline{E^4W^2} & -\overline{E^4UV} & -\overline{E^4UW} & -\overline{E^4VW} \\
-\overline{V^2} & -\overline{EV^2} & -\overline{E^2V^2} & -\overline{E^3V^2} & -\overline{E^4V^2} & \overline{V^4} & \overline{V^2W^2} & \overline{UV^3} & \overline{UV^2W} & \overline{V^3W} \\
-\overline{W^2} & -\overline{EW^2} & -\overline{E^2W^2} & -\overline{E^3W^2} & -\overline{E^4W^2} & \overline{V^2W^2} & \overline{W^4} & \overline{UVW^2} & \overline{UW^3} & \overline{VW^3} \\
-\overline{UV} & -\overline{EUV} & -\overline{E^2UV} & -\overline{E^3UV} & -\overline{E^4UV} & \overline{UV^3} & \overline{UVW^2} & \overline{U^2V^2} & \overline{U^2VW} & \overline{UV^2W} \\
-\overline{UW} & -\overline{EUW} & -\overline{E^2UW} & -\overline{E^3UW} & -\overline{E^4UW} & \overline{UV^2W} & \overline{UW^3} & \overline{U^2VW} & \overline{U^2W^2} & \overline{UVW^2} \\
-\overline{VW} & -\overline{EVW} & -\overline{E^2VW} & -\overline{E^3VW} & -\overline{E^4VW} & \overline{V^3W} & \overline{VW^3} & \overline{UV^2W} & \overline{UVW^2} & \overline{V^2W^2}
\end{bmatrix}. \tag{2.8}$$

$\vec{x}$ is a vector containing the 10 unknown coefficients A_1 through A_{10}, and the right-hand-side vector is:

$$\vec{b} = \left[\overline{U^2}\ \overline{EU^2}\ \overline{E^2U^2}\ \overline{E^3U^2}\ \overline{E^4U^2}\ -\overline{U^2V^2}\ -\overline{U^2W^2}\ -\overline{U^3V}\ -\overline{U^3W}\ -\overline{U^2VW}\right]^T. \tag{2.9}$$

N_c in the above matrix refers to the number of calibration points, and the bars over the other terms indicate summations over the whole calibration data set,

[3]The matrix and right-hand-side vector in reference [45] and [51] are not correct. They both missed some minus signs.

i.e.:

$$\overline{E} = \sum_{i=1}^{N_c} E_i,\ \overline{E^2} = \sum_{i=1}^{N_c} E_i^2,\ etc. \tag{2.10}$$

Mathematically, 10 calibration values are the minimum needed to determine the system. To archive higher accuracy in practice, 65 different calibration orientations of the calibration jet for each of three calibration jet speeds, Q, were used. The locations are identified by their pitch and yaw angles, as illustrated in Fig. 2.9. The calibration jet is sketched in Fig. 2.10.

The jet was fixed on a support that could be moved both in pitch (vertical) and yaw (horizontal) motion, thus providing directional information to each sensor. For a given jet velocity Q and pitch/yaw angle combination, we have

$$U = Qcos(\gamma)cos(\phi) \tag{2.11}$$

$$V = Qsin(\gamma)cos(\phi) \tag{2.12}$$

$$W = Qsin(\phi), \tag{2.13}$$

where γ is the pitch angle and ϕ is the yaw angle with respect to the tunnel's streamwise direction. These velocity components were supplied to equation (2.7) for the calibration calculation. These predetermined pitch and yaw orientations of the jet with respect to the probe were obtained with a computer controlled motor driven positioning system. So the whole calibration process is automatic, needing no human intervention. The path in Fig. 2.9 (dashed lines) was selected to minimize the time needed to move the jet during the calibration.

Fig. 2.11 and 2.12 show a set of calibration curves for the 12-sensor probe determined in our experiment. The circle symbols were calculated using (2.6), while the star symbols were calculated from (2.7). The variable r refers to Pearson's

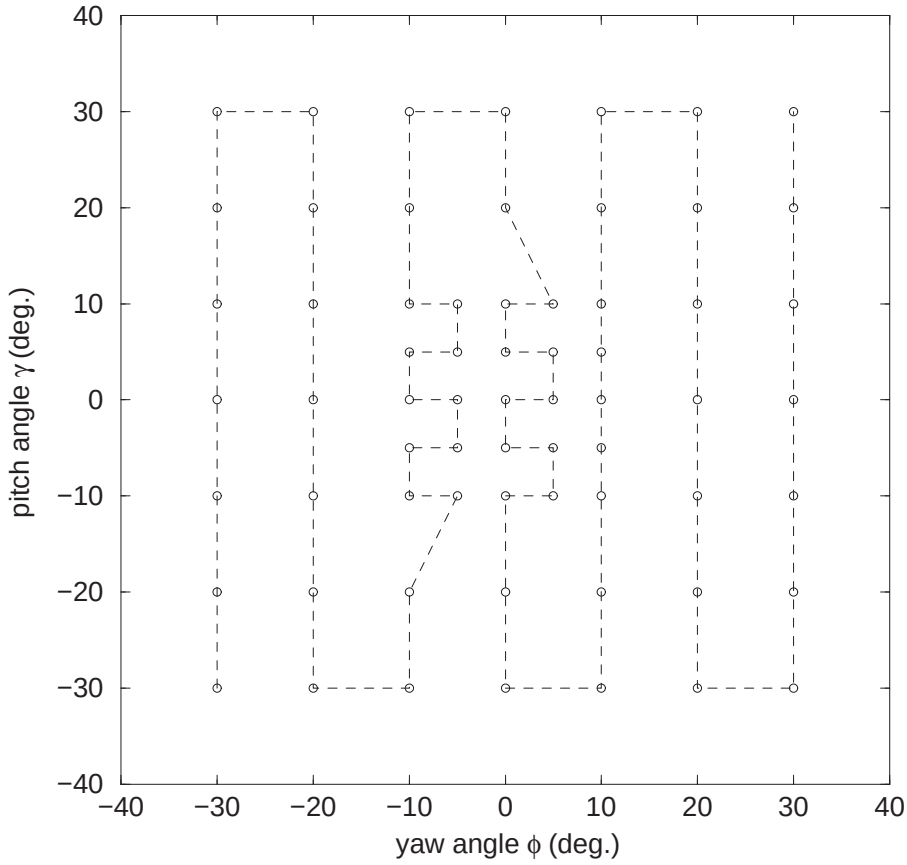

Figure 2.9: Pitch and yaw angles of calibration jet. The dashed lines show the optimized path to minimize the time needed to move the jet during the calibration.

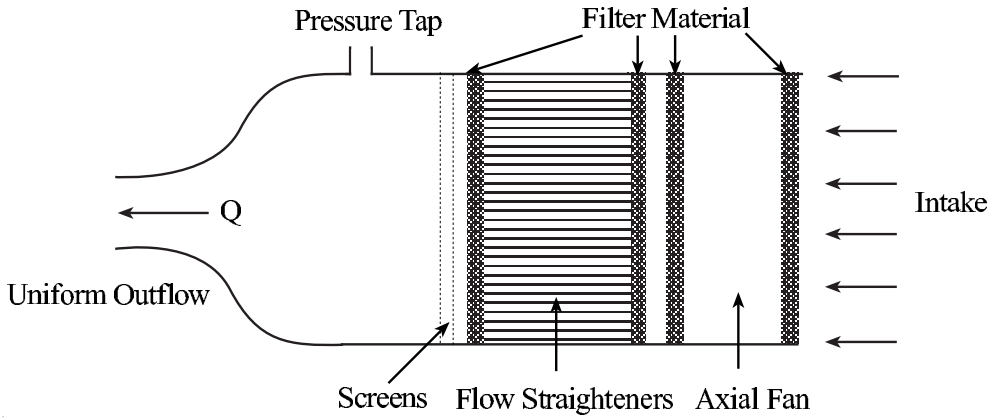

Figure 2.10: Calibration jet.

correlation coefficient, defined by

$$r = \frac{\sum U_{eff_U}^2 U_{eff_E}^2}{\sqrt{\sum (U_{eff_U}^2)^2 \sum (U_{eff_E}^2)^2}}, \tag{2.14}$$

where U_{eff_U} is the effective cooling velocity defined by (2.7), and U_{eff_E} is the effective cooling velocity defined by (2.6). The very high correlation between the cooling law and the polynomial fits to the voltage values provides good confidence in the calibration.

2.8.3 Temperature correction of hot-wire calibration

The hot-wire sensor is a temperature sensitive device. During the experiment, which generally lasts for many hours, changes in ambient temperature can affect the heat transfer rate from the wires, which introduces changes in the hot-wire voltages not related to the velocity variation that is the point of the measurements. Even worse, the magnitudes of such errors can be amplified when applying (2.6), because of the non-linear characteristics of polynomials.

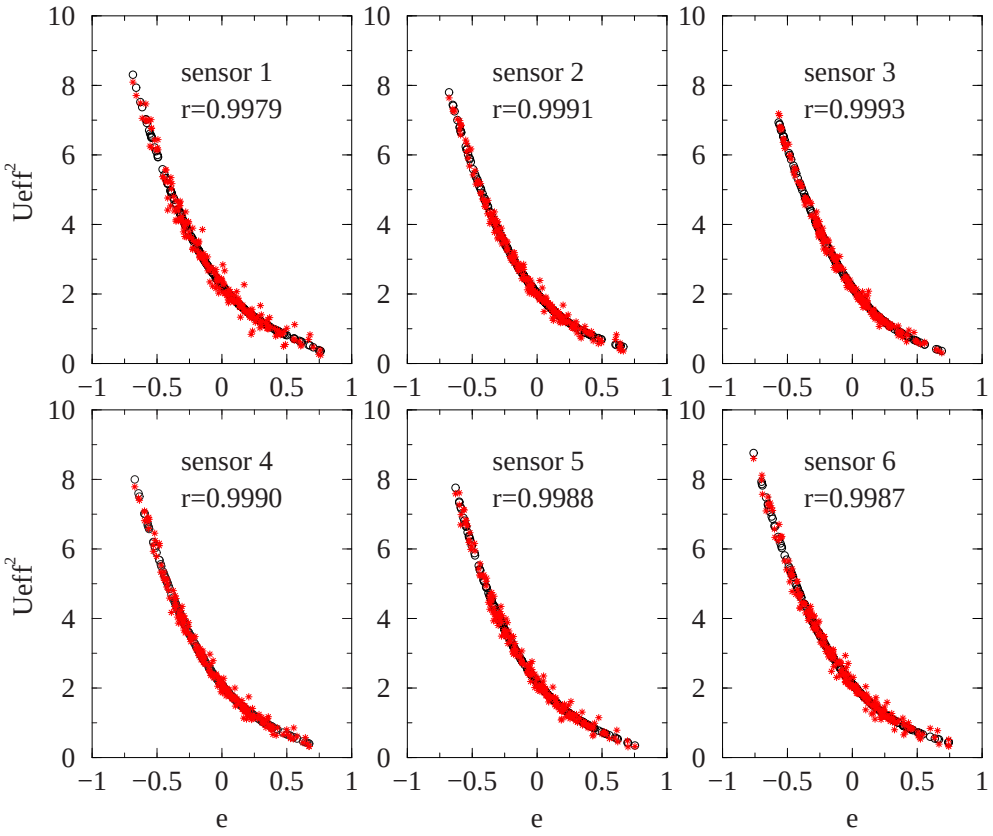

Figure 2.11: Calibration curves of 12-sensor probe: sensors 1 through 6. Pearson's correlation coefficient r is given for each sensor.

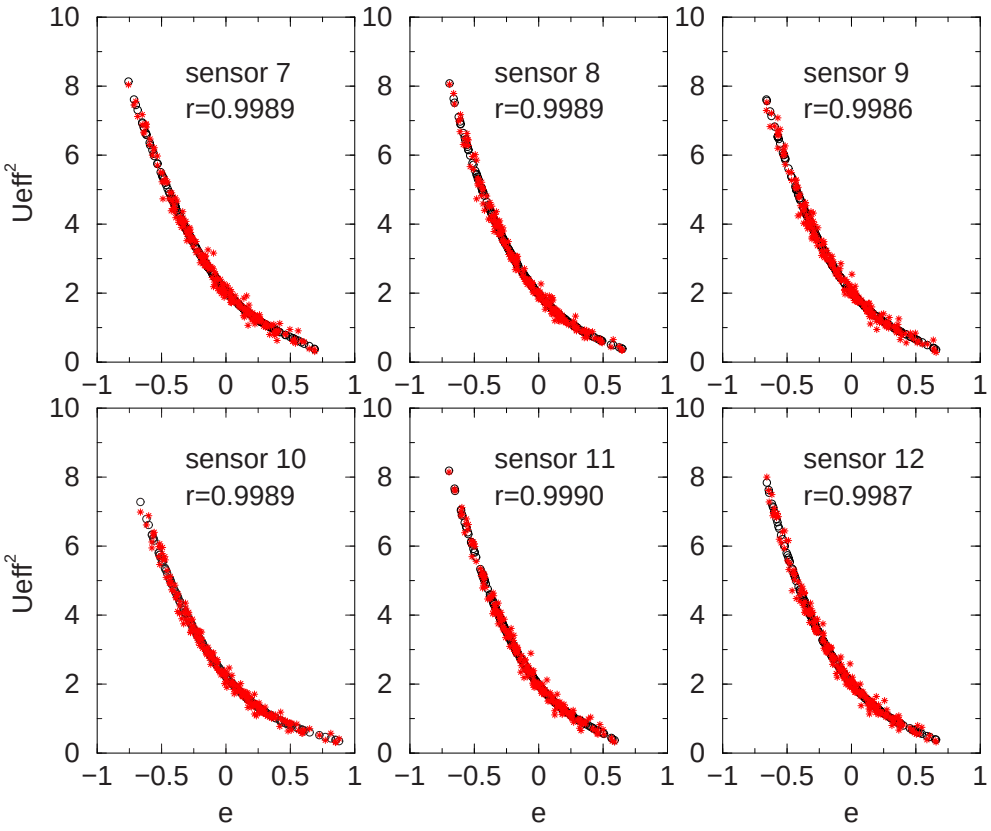

Figure 2.12: Calibration curves of 12-sensor probe: sensors 7 through 12.

The variation in ambient temperature could not be easily avoided. All electronic devices in the lab, especially the laser, generated heat during the experiment. However, it was possible to take the thermal effects into account by recording the fluid temperature along with other signals and then performing temperature corrections at the post-processing stage.

A type-K thermocouple was used to measure the temperature in the wind tunnel during the whole duration of the experiment. The analog temperature signal was digitized by the data acquisition system along with the hot-wire voltages. A linear correction of the hot-wire voltages was performed, given by the formula:

$$E' = E + (T - T_{ref})\sigma_T, \tag{2.15}$$

where E is the measured voltage, E' is the corrected voltage, T is the measured temperature, T_{ref} is a constant reference temperature and σ_T is a correction constant determined from the calibration data. This correction has to be done for each individual hot-wire sensor, and the correction constants can be different.

This linear correction is quite accurate and effective for small temperature changes of no more than a few degrees. This correction method was optimized by iterating the correction constant σ_T to achieve a maximum value of Pearson's correlation, as defined in (2.14). These maximum values are higher than the correlation values calculated from data without temperature correction, as shown in table 2.1.

Table 2.1: Temperature correction to obtain better calibration results.

Sensor	σ_T	r before temperature correction	r after correction
1	-6.0	0.9979	0.9984
2	-2.9	0.9991	0.9993
3	-2.5	0.9993	0.9994
4	-4.9	0.9990	0.9993
5	-5.5	0.9988	0.9992
6	-3.5	0.9987	0.9990
7	-2.6	0.9989	0.9990
8	-4.5	0.9989	0.9992
9	-5.1	0.9986	0.9990
10	-3.7	0.9989	0.9991
11	-1.9	0.9990	0.9992
12	-5.5	0.9987	0.9991

2.9 Hot-wire Data Reduction Techniques

The data reduction is the process by which the velocity and velocity gradient components are obtained from the hot-wire voltage signals. Unlike the single-sensor hot-wire case, where velocity can be directly related to the hot-wire voltage using the calibration curve, the 12-sensor data reduction is much more complex.

A basic assumption for all data reduction methods for probes that are used to obtain velocity gradients is that the instantaneous gradient is constant over the probe sensing area. This assumption is reasonable as long as the size of the probe is comparable to the minimum length scale of the turbulence. In [45], it was shown that the spatial resolution of the 12-sensor probe is about $4 - 5$ Kolmogorov scales, η, in the mixing layer flow at a similar Reynolds number to that for the current experiment. This provides confidence to use the following data reduction methods.

There are two data reduction methods that have been developed in parallel for the 12-sensor hot-wire probes of the Turbulence Research Laboratory. Both methods were performed on the current data set. They are briefly discussed here. Interested readers are referred to [51] and [76] for detailed documentation of these two methods.

2.9.1 Data reduction method I

The first method is a least-square type of method. The starting point is still (2.6) and (2.7). After the calibration coefficients, A_i, have been determined and the probe is exposed to a turbulent flow, the velocity components cooling each sensor become the unknowns. These unknowns can be transformed into the

velocity components at the centroid of the probe's projected frontal plane passing through the sensor centers and the velocity gradients in this plane by expanding the velocity vector at this centroid location using a first order Taylor's series, giving

$$\vec{U}_j = \vec{U}_0 + \Delta y_j \frac{\partial \vec{U}}{\partial y} + \Delta z_j \frac{\partial \vec{U}}{\partial z}. \tag{2.16}$$

Here the subscript j indicates the jth sensor, $\vec{U}_0$ refers to the velocity vector at the centroid of the probe frontal plane, and Δy_j and Δz_j are coordinates of the midpoint of each sensor with respect to the centroid.

Substituting the Taylor's series (2.16) into (2.7) and then subtracting it from (2.6) yields:

$$\begin{aligned}
\epsilon_j &= A_1 + A_2 E_j + A_3 E_j^2 + A_4 E_j^3 + A_5 E_j^4 \\
&- (U_0^2 + 2\Delta y U_0 \frac{\partial U}{\partial y} + 2\Delta z U_0 \frac{\partial U}{\partial z}) \\
&- A_6 (V_0^2 + 2\Delta y V_0 \frac{\partial V}{\partial y} + 2\Delta z V_0 \frac{\partial V}{\partial z}) \\
&- A_7 (W_0^2 + 2\Delta y W_0 \frac{\partial W}{\partial y} + 2\Delta z W_0 \frac{\partial W}{\partial z}) \\
&- A_8 [U_0 V_0 + \Delta y (U_0 \frac{\partial V}{\partial y} + V_0 \frac{\partial U}{\partial y}) + \Delta z (U_0 \frac{\partial V}{\partial z} + V_0 \frac{\partial U}{\partial z})] \\
&- A_9 [U_0 W_0 + \Delta y (U_0 \frac{\partial W}{\partial y} + W_0 \frac{\partial U}{\partial y}) + \Delta z (U_0 \frac{\partial W}{\partial z} + W_0 \frac{\partial U}{\partial z})] \\
&- A_{10} [V_0 W_0 + \Delta y (V_0 \frac{\partial W}{\partial y} + W_0 \frac{\partial V}{\partial y}) + \Delta z (V_0 \frac{\partial W}{\partial z} + W_0 \frac{\partial V}{\partial z})].
\end{aligned} \tag{2.17}$$

In the above equation, U_0, V_0 and W_0 are the three velocity components at the centroid of the probe front plane, and ϵ_j is the error term of the jth sensor. The subscript j on Δy and Δz identifying each sensor is omitted for simplicity. Small magnitude second order terms have all been dropped in (2.17).

The sum of the errors of all 12 sensors is:

$$E = \sum_{j=1}^{12} \epsilon_j. \tag{2.18}$$

By minimizing the total error E, the unknowns (U_0, V_0, W_0, $\partial U/\partial y$, $\partial U/\partial z$, $\partial V/\partial y$, $\partial V/\partial y$, $\partial W/\partial y$ and $\partial W/\partial z$) can be determined. Unlike the calibration system that produces linear equations of the unknowns, the solution system here is non-linear. An iterative method was developed to solve this least-square system.

Occasionally this method does not work very well in the flow regions where large turbulent fluctuations occur. This can be the near-wall region of a turbulent boundary layer, where fluctuations sometimes have the same magnitude as the mean velocities, or it can be near the center line of the mixing layer, where the flow is highly turbulent. In such situations, it is possible that some instantaneous velocity vectors are almost parallel to some of the sensors. As a result, the mathematical properties of the solution system is poor, and the solution method does not converge.

In a previous boundary layer experiment [53], it was reported that only 5% of data points suffered from the above problems near the wall at $y^+ = 26$. The mixing layer experiments were affected much less by this because of the existence of large mean streamwise velocities everywhere in the flow. In general, this data reduction method is highly efficient and relatively easy to implement.

2.9.2 Data reduction method II

The second method was developed by Vukoslavčević et al. [76] and uses a different approach to determine the velocity and gradient field.

The starting point is still Jorgensen's cooling law with velocity components U, V and W at each sensor expanded using a Taylor's series. However, in this method the Taylor's expansion is with respect to the array centers, instead of the geometric center of the probe frontal plane:

$$\vec{U}_j = \vec{U}_{0,i} + \Delta y_j \frac{\partial \vec{U}}{\partial y} + \Delta z_j \frac{\partial \vec{U}}{\partial z}. \tag{2.19}$$

Here $\vec{U}_{0,i}$ refers to the velocity vector at the center of array i, to which sensor j belongs. After substituting this expansion into the Jorgensen's cooling law (2.2), a set of non-linear equations very similar to (2.17) are obtained:

$$\begin{aligned}
0 &= A_1 + A_2 e_j + A_3 e_j^2 + A_4 e_j^3 + A_5 e_j^4 \\
&- (U_{0,i}^2 + 2\Delta y U_{0,i} \frac{\partial U_i}{\partial y} + 2\Delta z U_{0,i} \frac{\partial U_i}{\partial z}) \\
&- A_6 (V_{0,i}^2 + 2\Delta y V_{0,i} \frac{\partial V_i}{\partial y} + 2\Delta z V_{0,i} \frac{\partial V_i}{\partial z}) \\
&- A_7 (W_{0,i}^2 + 2\Delta y W_{0,i} \frac{\partial W_i}{\partial y} + 2\Delta z W_{0,i} \frac{\partial W_i}{\partial z}) \\
&- A_8 [U_{0,i} V_i + \Delta y (U_{0,i} \frac{\partial V_i}{\partial y} + V_{0,i} \frac{\partial U_i}{\partial y}) + \Delta z (U_{0,i} \frac{\partial V_i}{\partial z} + V_{0,i} \frac{\partial U_i}{\partial z})] \\
&- A_9 [U_{0,i} W_{0,i} + \Delta y (U_{0,i} \frac{\partial W_i}{\partial y} + W_{0,i} \frac{\partial U_i}{\partial y}) + \Delta z (U_{0,i} \frac{\partial W_i}{\partial z} + W_{0,i} \frac{\partial U_i}{\partial z})] \\
&- A_{10} [V_{0,i} W_{0,i} + \Delta y (V_{0,i} \frac{\partial W_i}{\partial y} + W_{0,i} \frac{\partial V_i}{\partial y}) + \Delta z (V_{0,i} \frac{\partial W_i}{\partial z} + W_{0,i} \frac{\partial V_i}{\partial z})].
\end{aligned} \tag{2.20}$$

However, here the velocity components $U_{0,i}$, $V_{0,i}$ and $W_{0,i}$ are defined at the *ith* array center. Δy_j and Δz_j refer to the distance from the sensor centers to the array centers, which is considerably smaller than the distance from the sensor centers to the probe centroid. Thus it is reasonable to assume that all the gradient terms in above equation are much smaller than those gradient terms in equation (2.17).

Based on this assumption, the following iterative method can be used to solve for the velocity and velocity gradient components.

- Equation (2.20) is first solved for each array with all gradient terms neglected. This reduces the system to three 4-equation uncoupled systems. Each of them has only $U_{0,i}$, $V_{0,i}$ and $W_{0,i}$ as their three unknowns. They are over-determined systems. The 'best' three equations are chosen to solve the system. The criteria for choosing the 'best' will be discussed below.

- The previous step gives first estimates of the velocity components at the three array centers. Then estimates of all the gradient terms at the probe center can be found from the array center velocity components. For example, if the arrays are arranged as in Fig. 2.13, then the gradient $\partial U/\partial y$ can be estimated to first order as:

$$\frac{\partial U}{\partial y} = \frac{U_I - 0.5(U_{II} + U_{III})}{\Delta y}, \tag{2.21}$$

  where the subscripts I, II and III refer to the different arrays. Other gradients in the plane can be evaluated similarly.

- The gradients estimated in the previous step then can serve as gradient values at the array centers in (2.20). The 'best' three equations then can be solved again with those gradient terms known for improved velocity component estimates.

- The previous two steps are repeated until both the velocity and the velocity gradients converge to within some specified small value.

This method has been found to converge very quickly, requiring just a few

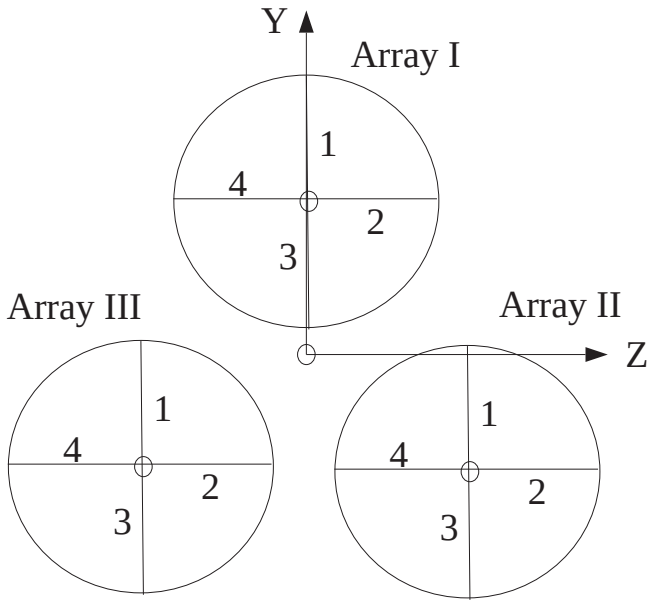

Figure 2.13: Arrangement of three arrays in a 12-sensor hot-wire probe.

iterations. It also suffers less from the non-convergence problems[4] described above for method 1. The two data reduction approaches yielded almost same results for this mixing layer experiment. The experimental results presented in Chapter 3 were obtained using method 2.

As mentioned above for method 2, the 'best' three equations need to be chosen from four equations to solve the velocity components at each array. In Fig. 2.13, sensors 2 and 4 in each array are always selected. This is because the dominant gradient terms in both the boundary layer flow and the mixing layer flow are in the y direction. Only one from sensors 1 and 3 is chosen by a 'smart' program

[4]In the present experiment, at the mixing layer centerline location, only 182 of 540,000 (0.034%) velocity values are not converged. The centerline location should be affected the most by the non-convergence issue because flow there is most likely to experience large fluctuations in spanwise and cross-stream directions.

based on their orientations with respect to the instantaneous velocity vectors. The one that ensures the uniqueness of physical solutions is always chosen. Detailed discussion of this issue can be found in [76].

The redundant information provided by the 4th sensor in each array also ensures the success of the measurement when unexpected events happen. At the very end of the current experiment, one of the twelve sensors was broken. Thanks to this redundancy, the data reduction method was still able to give reasonable velocity field values so that the data at the last few locations was salvaged.

2.10 Mixing Layer Characteristics

In Fig. 2.14 the streamwise mean velocity profiles measured at several locations downstream of the trailing edge of the splitter plate are shown. These profiles were measured with a single-sensor hot-wire probe in a preliminary experiment. This and other preliminary experiments were performed for the purpose of validating the mixing layer facility and providing some basic understanding of the flow.

As can be seen in the figure, right after the trailing edge of the splitter plate, the two turbulent boundary layer profiles from either side of the splitter plate merge together. In Fig. 2.15, both the low-speed-side and high-speed-side velocity profiles are plotted in semi-log coordinates where it is seen that they more or less display log law characteristics. The low-speed-side boundary layer profile deviates more from the log law because of the existence of a pressure gradient caused by the arrangement of the splitter plate.

Further downstream, the mixing layer begins to grow and evolves into the

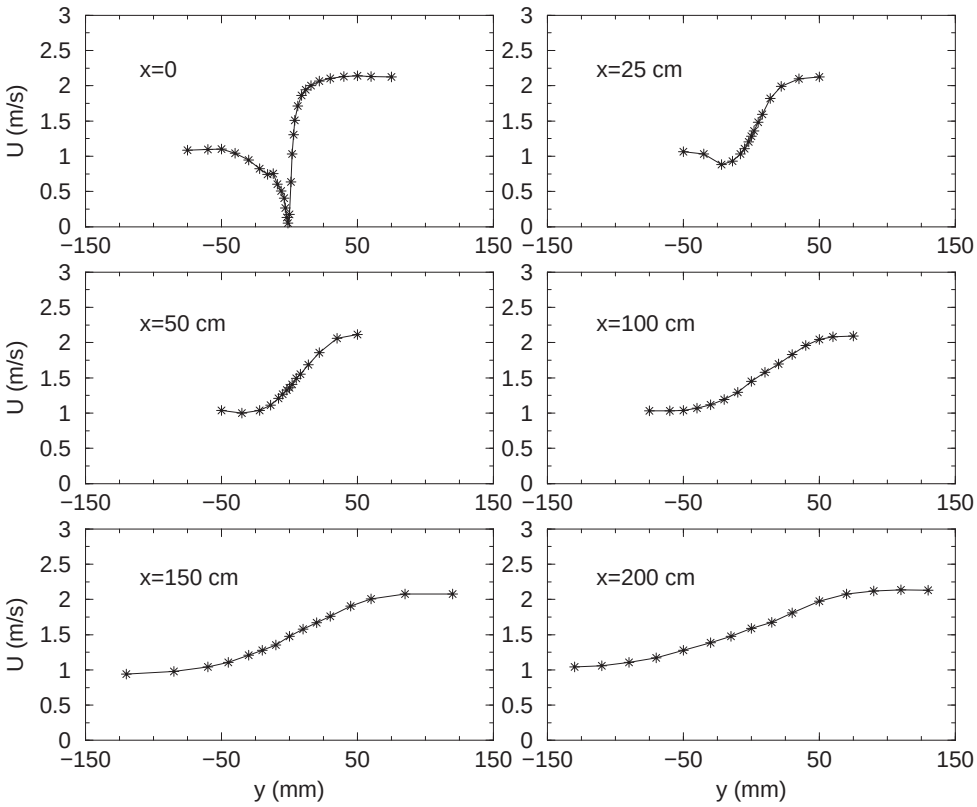

Figure 2.14: Mean velocity profiles at different downstream locations from the splitter plate trailing edge.

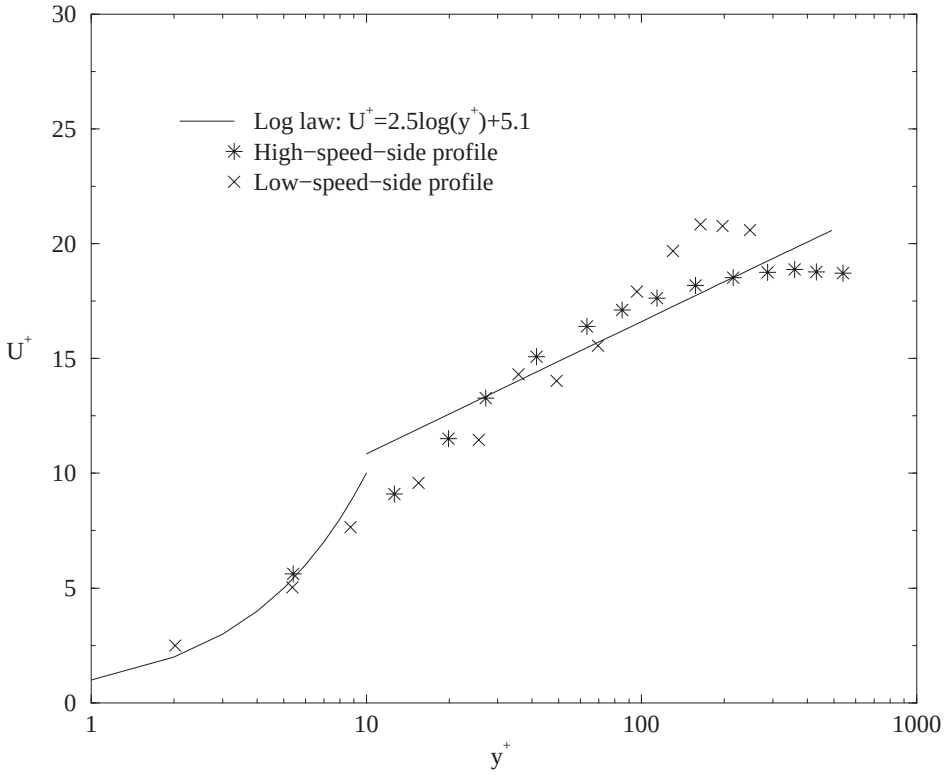

Figure 2.15: High-speed and low-speed boundary layer velocity profiles at the splitter plate trailing edge.

self-similar shape at about 50 centimeters away from the splitter plate. From these profiles, one can easily evaluate the growth of the momentum thickness of the mixing layer,

$$\theta = \int_{-\infty}^{\infty} \left[\frac{1}{4} - \left(\frac{\overline{U_1} - U_c}{\Delta U} \right)^2 \right] dy. \tag{2.22}$$

Here $U_c \equiv 0.5(U_h + U_l)$ is defined as splitter plate plane velocity, $\Delta U \equiv U_h - U_l$ is the velocity difference between high-speed-side and low-speed-side free-stream ($U_h = 1.97m/s$ and $U_l = 1.00m/s$ in the final experiment), and $\overline{U_1}$ is the local mean velocity at location y in the mixing layer. As will be discussed, the momentum thickness is of great importance to the mixing layer flow as a characteristic length scale. From the experimental data, it can be evaluated using a discrete form of (2.22):

$$\theta = \sum_{k} \left[\frac{1}{4} - \left(\frac{\overline{U}_{1,k} - U_c}{\Delta U} \right)^2 \right] \Delta y, \tag{2.23}$$

where Δy is the step interval in the cross-stream direction that the hot-wire probe is traversed in k steps. Fig. 2.16 shows the linear growth of momentum thickness in the mixing layer flow. The growth rate $d\theta/dx = 0.013$.

Based on the length scale θ and the velocity scale ΔU, the Reynolds number can be defined as:

$$Re_\theta = \frac{\Delta U \theta}{\nu}. \tag{2.24}$$

In the present experimental studies, the detailed 12-sensor measurements were performed at $2m$ downstream from the trailing edge of the splitter plate in the self-similar region, where the momentum thickness is about $25.6mm$ and the Reynolds number is about $Re_\theta = 1590$.

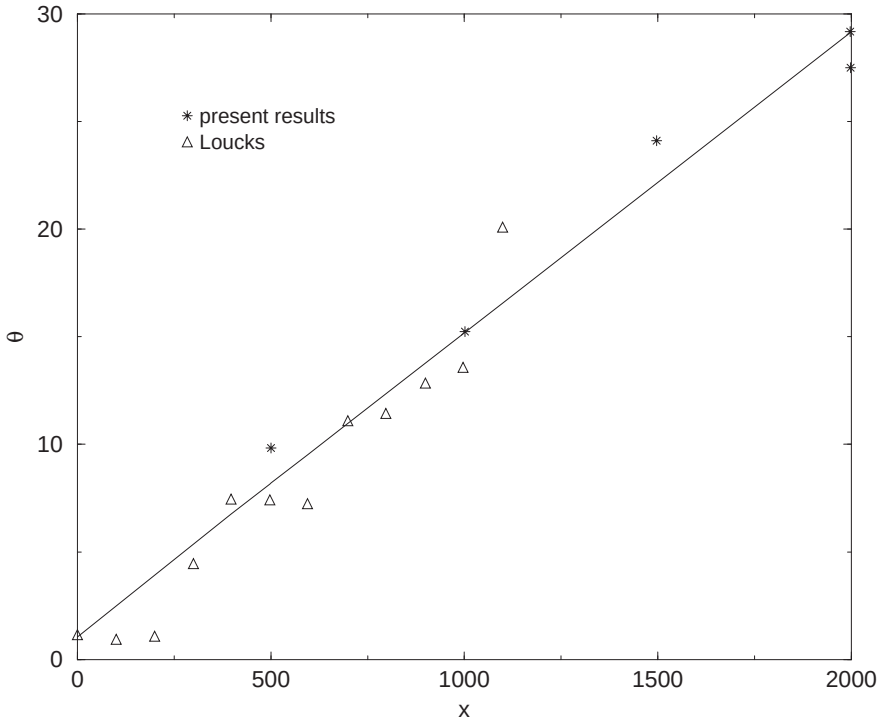

Figure 2.16: The growth of momentum thickness in the mixing layer. Units are in *mm* and the solid line is a least-square linear fit.

Chapter 3

Large-Eddy Simulations

While experimental studies like the one outlined in the previous chapter can provide reliable statistical information on several quantities of interest, numerical simulations can generally provide a wealth of complementary information about turbulent flows. In the current mixing layer study, for example, hot-wire time series measurements of the velocity and vorticity fields were limited to a few spatial locations, and conditional analysis of the data was performed to extend the knowledge to a two-dimensional plane. On the other hand, highly accurate numerical simulations can provide information on the local flow topology and dynamics that is not directly measurable.

In the framework of the present work, to complement the experimental studies, large-eddy simulation of spatially developing turbulent mixing layers were performed in parallel. The simulations were designed to match the experimental conditions as closely as possible. The scalar transport in the flow was simulated by tracking massless particles.

In section 3.1, an overview of the adopted LES methodology is presented. Following this, two special topics are covered. First, the treatment of the inflow

boundary conditions, which is critical for the accuracy of spatially developing flows, will be covered in section 3.2. Then in section 3.3, the particle tracking schemes used to study the scalar transport will be discussed in detail.

3.1 Overview of the Method

3.1.1 Mathematical formulation

The LES methodology is intermediate between the direct numerical simulation (DNS) approach, where all scales of motion are resolved, and the Reynolds Averaged Navier Stokes (RANS) approach, where all turbulent scales are modelled. In particular, in LES a spatially filtered form of Navier-Stokes equations is solved and all scales larger than the filter size – which is usually proportional to the local grid spacing – are resolved directly as in a DNS. Only scales smaller than the filter size are modelled. An inherent advantage of this modelling strategy is its predictive capability: the large, energy carrying eddies that depend on the specific geometry and boundary conditions are directly resolved; the small scales that are approximately homogeneous and isotropic and therefore do not depend on the specific flow problem are modelled using simple and inexpensive eddy viscosity type models.

In the present finite-difference implementation a top-hat filter is implicitly applied by the difference operator to separate the large resolved scales from the ones to be modelled. The resulting equations of motion have the following form:

$$\frac{\partial \overline{u}_i}{\partial x_i} = 0 \tag{3.1}$$

$$\frac{\partial \overline{u}_i}{\partial t} + \frac{\partial}{\partial x_j}(\overline{u}_i \overline{u}_j) = -\frac{\partial \overline{p}}{\partial x_i} + \frac{1}{Re}\frac{\partial^2 \overline{u}_i}{\partial x_i \partial x_j} - \frac{\partial \tau_{ij}}{\partial x_j}, \tag{3.2}$$

where the overbar denotes a filtered variable and

$$\tau_{ij} = \overline{u_i u_j} - \overline{u}_i \overline{u}_j, \tag{3.3}$$

are the subgrid scale (SGS) stresses that need to be parameterized. $u_i (i = 1, 2, 3)$ are the components of the velocity vector in the three coordinate directions, p is the pressure and Re is the Reynolds number.

The purpose of SGS models is to account for the effects of small-scale eddies in the flow, mostly by removing energy from the resolved scales to mimic the way that energy is dissipated at the end of the energy cascade. In the present study a preliminary set of computations was conducted using the Smagorinsky model [65], which relates the subgrid-scale stress to the resolved strain rate:

$$\tau_{ij} - \frac{1}{3}\delta_{ij}\tau_{kk} = -2\nu_T \overline{S}_{ij} = -2C\Delta^2 |\overline{S}_{ij}| \overline{S}_{ij}. \tag{3.4}$$

In (3.4) ν_T is the turbulent eddy viscosity and Δ is the filter size, defined as $(\Delta x \Delta y \Delta z)^{1/3}$, where $\Delta x, \Delta y, \Delta z$ is the local grid spacing in the three coordinate directions. $\overline{S}_{ij}$ is the resolved strain rate, defined as:

$$\overline{S}_{ij} = \frac{1}{2}\left(\frac{\partial \overline{u}_i}{\partial x_j} + \frac{\partial \overline{u}_j}{\partial x_i}\right). \tag{3.5}$$

The value of the constant C needs to be chosen based on the type of problem. In all computations where the Smagorinsky model is used, a value of $C = 0.11$ was adopted.

One weakness of this model is that a single model constant used throughout the flow is often unable to properly represent all the complex turbulent features. A more important concern in the present study is the fact that the model does

not vanish in areas of the flow field where the flow is laminar. This can introduce complication near the edge of the mixing layer where irrotational fluctuations are present. To alleviate this concern a dynamic eddy viscosity type model was subsequently used [26].

Such models dynamically determine the model constant to reflect the local conditions of the flow. The basic idea is to apply a coarser spatial filter (called the test-filter, compared to the finer filter which is called the grid-filter) on the N-S equations and assume that the resulting subtest-scale stresses associated with the test filter T_{ij} also can be modelled using an eddy viscosity type of model as in equation (3.4):

$$T_{ij} - \frac{1}{3}\delta_{ij}T_{kk} = -2C\widehat{\Delta}^2|\widehat{\overline{S}}_{ij}|\widehat{\overline{S}}_{ij}, \tag{3.6}$$

where the hat indicates test filtering, $\widehat{\Delta}$ is the coarser filter width and $\widehat{\overline{S}}_{ij}$ is the test-filtered strain rate. The stresses at the two different grid levels can be related with the following identity: [26]

$$\mathcal{L}_{ij} = T_{ij} - \widehat{\tau_{ij}} = \widehat{\overline{u}_i\overline{u}_j} - \widehat{\overline{u}}_i\widehat{\overline{u}}_j. \tag{3.7}$$

Equation (3.4), (3.6) and (3.7) can be used to determine the model coefficient C dynamically. Here the least-square method proposed by Lilly [44] is adopted:

$$C(x_i, t) = \frac{1}{2}\frac{\mathcal{L}_{ij}M_{ij}}{M_{ij}M_{ij}}, \tag{3.8}$$

where M_{ij} is defined as:

$$M_{ij} = \widehat{\Delta}^2|\widehat{\overline{S}}_{ij}|\widehat{\overline{S}}_{ij} - \overline{\Delta}|\widehat{\overline{S}_{ij}|\overline{S}_{ij}}. \tag{3.9}$$

The model coefficient given by (3.8) is a function of both space and time, and it is known to cause numerical instabilities when it becomes negative. For this

reason, an ensemble average is needed to remove the sharp fluctuations of the coefficient. In the present work, the Lagrangian averaging procedure proposed by Meneveau et al. [47] is adopted. It accumulates the required averages over flow pathlines rather than over homogeneous directions. This is sensible because the local flow condition at a given point $\vec{x}$ can be highly dependent on the history of flow along the trajectory leading to $\vec{x}$.

Using this idea, the ensemble averages of the numerator and denominator of (3.8) can be written as:

$$< \mathcal{L}_{ij} M_{ij} >= \int_{-\infty}^{t} \mathcal{L}_{ij}(t') M_{ij}(t') W(t - t') dt', \tag{3.10}$$

$$< M_{ij} M_{ij} >= \int_{-\infty}^{t} M_{ij}(t') M_{ij}(t') W(t - t') dt', \tag{3.11}$$

where $W(t)$ is a weighting function, normally giving more weight to recent times in history. Details of the present implementation can be found in [63].

3.1.2 Numerical method

Equation (3.1) and (3.2) are solved using a standard finite-difference fractional step method on a staggered grid. Details of the method can be found in [6]. In the following the basic elements of the approach are given.

For the purpose of discussion, the momentum equation (3.2) is rewritten in the form:

$$\frac{\partial \overline{u}_i}{\partial t} = H(\overline{u}_i, \overline{u}_j) - \frac{\partial \overline{p}}{\partial x_i}, \tag{3.12}$$

where H is just a spatial operator including all the convection and diffusion terms. Time advancement of (3.12) is done using an explicit Adams-Bashforth scheme

resulting in the following predicted velocity:

$$\frac{\overline{u}_i^* - \overline{u}_i^n}{\Delta t} = \frac{3}{2} H(\overline{u}_i, \overline{u}_j)^n - \frac{1}{2} H(\overline{u}_i, \overline{u}_j)^{n-1} + \frac{\partial \overline{p}^n}{\partial x_i}. \tag{3.13}$$

The velocity $\overline{u}^*$ obtained from the above equation is an estimation of the velocity field and it does not satisfy the continuity equation. Projection in a divergence-free space is done by solving the following Poisson equation:

$$\frac{\partial^2 \delta \overline{p}}{\partial x_i^2} = \frac{1}{\Delta t} \frac{\partial \overline{u}_i^*}{\partial x_i}. \tag{3.14}$$

The divergence-free velocity field is finally obtained from:

$$\frac{\overline{u}_i^{n+1} - \overline{u}_i^*}{\Delta t} = -\frac{\partial \delta \overline{p}}{\partial x_i}. \tag{3.15}$$

All spatial derivatives in H are obtained with second-order central difference on a staggered grid.

3.1.3 Boundary conditions

The specification of boundary conditions is of great importance. Some types of boundary conditions are easier to realize numerically than others. For example, periodic conditions and non-slip boundary condition are quite straightforward to implement. However, in a spatially developing flow, such as the turbulent mixing layer configuration of this investigation, the specification of inflow boundary conditions can be a great challenge. Section 3.2 will be dedicated to discuss the inflow boundary conditions for the mixing layer simulation. In the following other types of boundary conditions are briefly reviewed.

A schematic of the three-dimensional computational domain and the boundary types is given in Fig. 3.1. In the homogeneous spanwise direction, periodic

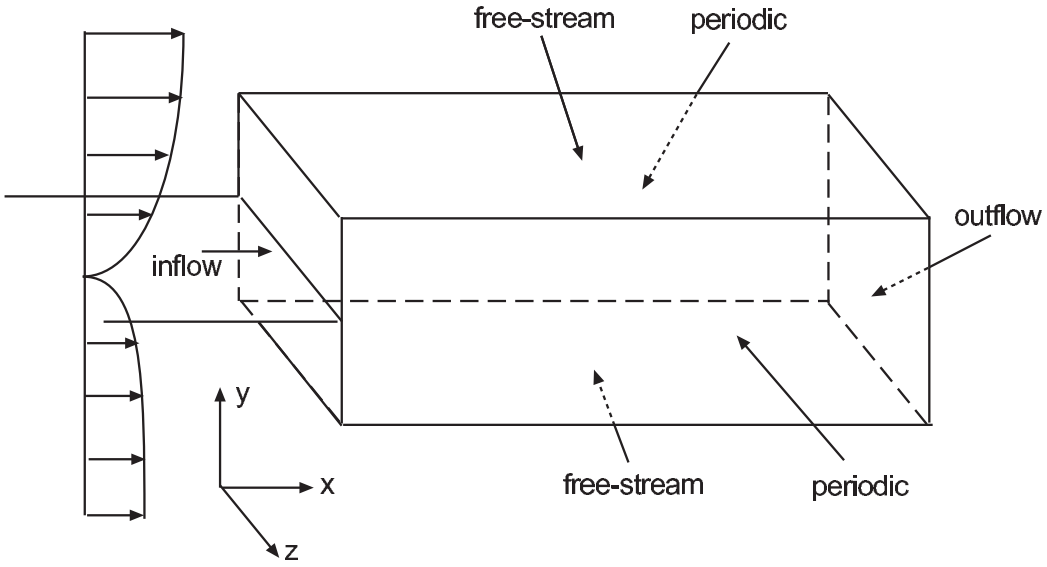

Figure 3.1: Schematic of the LES computational domain and the boundary types.

boundary conditions are used, where information from the other side of the box can be taken to determine the boundary values of velocity components. At the outflow boundary, one must specify boundary conditions that allow turbulent structures to leave the domain without introducing disturbances to the calculation. For this reason a convective condition is used [52] .

Care also must be taken to specify the boundary conditions at the two free stream boundaries of the mixing layer. The condition used in the current study is based on the assumption that the free stream is irrotational. The w component is determined from $dw/dz = 0$ while u and v are determined from solving:

$$\omega_x = \frac{\partial w}{\partial y} - \frac{\partial v}{\partial z} = 0, \tag{3.16}$$

$$\omega_y = \frac{\partial u}{\partial z} - \frac{\partial w}{\partial x} = 0. \tag{3.17}$$

This free stream boundary condition allows the fluid to enter or leave the

boundaries, which may cause imbalance of mass. The convective outflow boundary condition can also produce surplus or deficit of mass. Thus a global mass balancing procedure is necessary to ensure the conservation of mass. Here the mass imbalance is evaluated at the prediction step and a correction to the velocity component normal to the outflow boundary is added to conserve the mass. Such correction is applied on all outflow boundary cells and is usually very small.

3.2 Inflow Boundary Conditions

3.2.1 Introduction

Although most flows encountered in real applications develop in space, for many years DNS and LES of turbulence have been mostly confined to fully developed or time-developing flows, in which the specification of the boundary conditions is significantly simplified: periodic conditions can be used, removing the need to specify inflow and outflow conditions. For flows that develop spatially, such as the mixing layer or the flat-plate boundary layer, however, the use of periodic boundary conditions is not appropriate. To simulate such spatially developing flows, several approaches have been used and are briefly discussed in the following paragraphs.

For some flow problems one can still apply periodic boundary conditions, and observe the flow development in time. If Taylor's hypothesis holds, one can then relate time to space through a Galilean transformation with an appropriate convection velocity. Temporally developing mixing layers [62] and boundary layers [70] have been simulated in this manner. A limitation of this approach lies in the

fact that entrainment from the free-stream is not allowed, and in some flows (the boundary layer, for instance) the correct Reynolds shear stress profile cannot be recovered.

For self-similar flows, one can solve the governing equations in the self-similar coordinate frame. Spalart performed DNS of sink flow [67] and flat-plate boundary layers [68] using this approach. Spalart also used periodic conditions to study a boundary layer in the presence of favorable, then adverse pressure gradient (which is not self-similar) by introducing the 'fringe method' [69]. This technique consists in adding forcing terms to the Navier Stokes equations in small regions near the inflow and outflow of the domain to remove mass and decrease the boundary layer thickness at the outflow, prior to re-introducing it at the inflow. Although this method can be effective for the simulation of equilibrium boundary layers, and in some non-equilibrium cases [43], its general applicability is limited, since the streamwise extent of the computational box should be increased substantially to allow the flow to return to equilibrium as it approaches the outflow boundary.

The method proposed by Lund et al. [46] also requires self-similarity. It involves rescaling the velocity field at some downstream location, in a flat-plate boundary layer, and re-introducing it at the inflow. An advantage of this method is that it allows the calculation of nonequilibrium flows as long as a flat-plate of sufficient length is appended before the region of interest. A large region of the flow (and substantial computational resources) are, however, used only to generate a realistic inflow condition.

To study transitional flows, perturbations can be superposed on a laminar mean flow. This approach has been used successfully in boundary layers [57],

[30] and mixing layers [21]. If, however, one is interested in turbulent flows, the development of turbulence from perturbed boundary conditions may require excessively long streamwise domains, since turbulence must be allowed to develop from the imposed perturbation.

Alternatively, one may impose a mean velocity profile and superpose on it random noise perturbations, adjusting their phases to yield the desired moments up to some (typically second) order. This approach was adopted by Lee et al. [41] in a DNS of isotropic compressible turbulence; they found that the flow recovers fairly quickly (in about two integral length scales) from the random fluctuations. The method, however, appears to be less well suited to wall-bounded flows. Le et al. [40] and Akselvoll et al. [1] found that several boundary-layer thicknesses (10δ and 25δ, respectively) were needed for reasonable statistics to be established before the region of interest in backward facing step computations. In addition to the waste of computational resources due to large recovery lengths, control of the skin friction and integral thickness just upstream of the domain of interest is difficult: the development section is un-physical and the upstream conditions do not always lead to the desired statistics downstream.

The use of the results of auxiliary calculations may be the most realistic type of inflow condition available, since the development section can be drastically reduced or in some cases eliminated altogether. The auxiliary calculation must be run synchronously with or prior to the actual computation, and a time series of data stored on disk are used as inflow. Using this approach, several computations of spatially developing flows have been conducted successfully [2], [33], [46]. In high-Reynolds number flows, however, the number of points in the inflow plane increases dramatically and the cost of the auxiliary computation may become

significant from the storage and the CPU time point of view. This is the case for the two stream turbulent mixing layer, in which two separate auxiliary computations (low- and high-speed boundary layers) are needed. The proposed approach in the present study is based on the 'auxiliary calculation' approach.

3.2.2 Present approach and preliminary assessment

The inflow plane of a spatially developing mixing layer requires two boundary layers, one for the high-speed side and one for the low-speed side. In this situation, two auxiliary calculations are necessary. Also, the temporal resolution of the auxiliary simulations has to be the same as the main simulation. Thus their CPU and storage costs will be comparable to those of the main simulation. It would be beneficial if one could perform the auxiliary boundary-layer simulations for a shorter time period T_s, store two planes of data for each time step over the period T_s, and recycle the stored data as many times as needed at the inflow boundary of the main simulation.

It is obvious that such a procedure introduces a periodicity at the inflow plane of the mixing layer that might influence flow statistics. However, it can be argued that this periodicity may be eliminated by the non-linear interactions in the turbulence not far away from the inflow plane and that the downstream statistics will not be affected.

To test this idea a series of preliminary computations were conducted. All the quantities in this section will be normalized by δ_L^*, the displacement thickness of the low-speed boundary layer, and $U_{\infty L}$, the low-speed free-stream velocity. The configuration of the mixing-layer simulations is described in Fig. 3.2. The

computational domain has a size of $L_x = 1100$ (streamwise) by $L_y = 80$ (spanwise) by $L_z = 190$ (cross-stream). On the inflow plane, the high-speed side is a boundary-layer velocity profile with free-stream velocity $U_H = 2$, while the low-speed side has an up-side-down boundary-layer profile with free-stream velocity $U_L = 1$. This configuration was designed to mimic the experiment by Loucks [45], which measured a similar mixing layer with a multiple-sensor hot-wire probe.

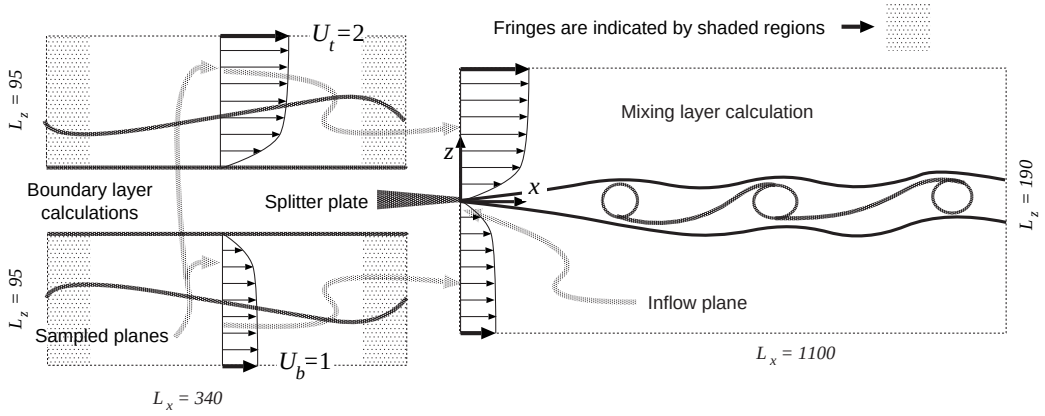

Figure 3.2: Computational domains for the mixing-layer simulation and two auxiliary boundary-layer simulations.

Two flat plate boundary-layer simulations were performed on domains of size $340(L_x)$ by $80(L_y)$ by $95(L_z)$. They were discretized with $80 \times 32 \times 40$ grids. The simulations were performed for a dimensionless time period of 776 units and one plane of data from each simulation was stored at each time step to the hard disk as the inflow conditions for the main simulation.

Three different mixing layer simulations were conducted: In the first case, the whole sample was used; in the second case, one half of the sample was used, repeated twice; in the third case, one quarter of the sample was used, repeated

four times. A windowing technique was used to modify the signals at their two ends to make them periodic so that no abrupt changes were introduced when recycling the inflow data. These time sequences are shown in Fig. 3.3.

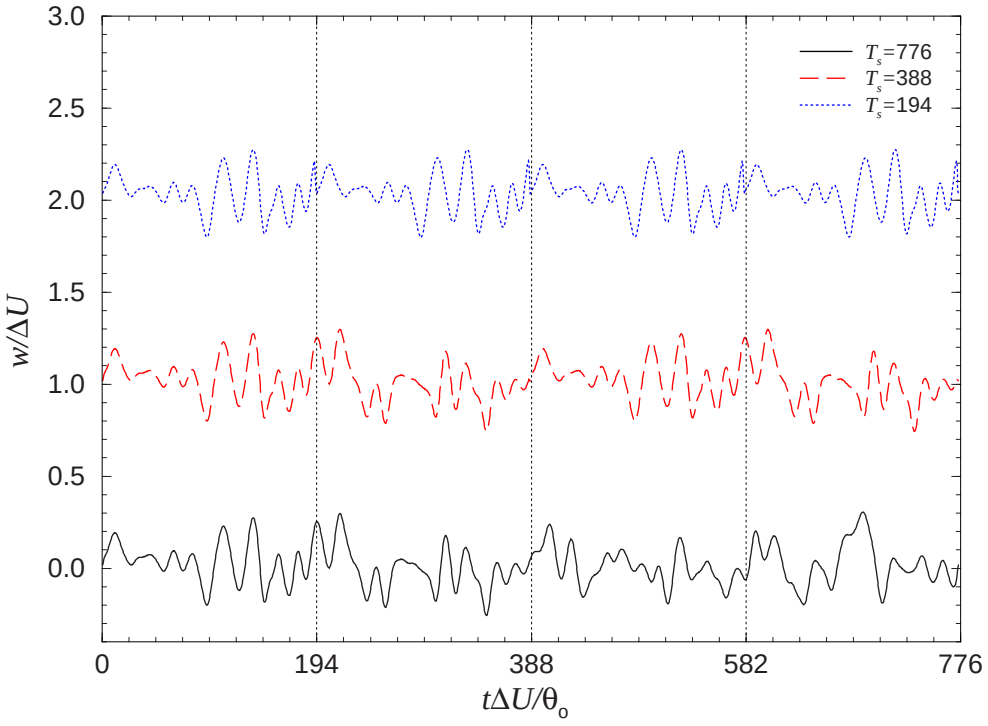

Figure 3.3: Time sequence of a velocity component at an arbitrary location on the inflow plane. Each signal is shifted one unit for clarity.

All three cases started from the same initial field and the simulations were allowed to develop in time for one flow-through time (during which a fluid particle travelling at the low-speed-side velocity could move out of the downstream boundary) before the statistics were accumulated for another flow-through time. Then statistics from the three cases were compared.

Shown in Fig. 3.4 (a) is the time-averaged momentum thickness of the mixing layer. The three cases agree quite well and the length of the inflow has little effect on this integral quantity. Fig. 3.4 (b) shows the averaged momentum thickness over four different periods in case 3. If the periodicity at inflow were maintained, the statistics by averaging over different periods would be identical and equal to the long-term average. However, Fig. 3.4 (b) clearly shows that the periodicity at the inflow was removed by the turbulence and all periods have different averages.

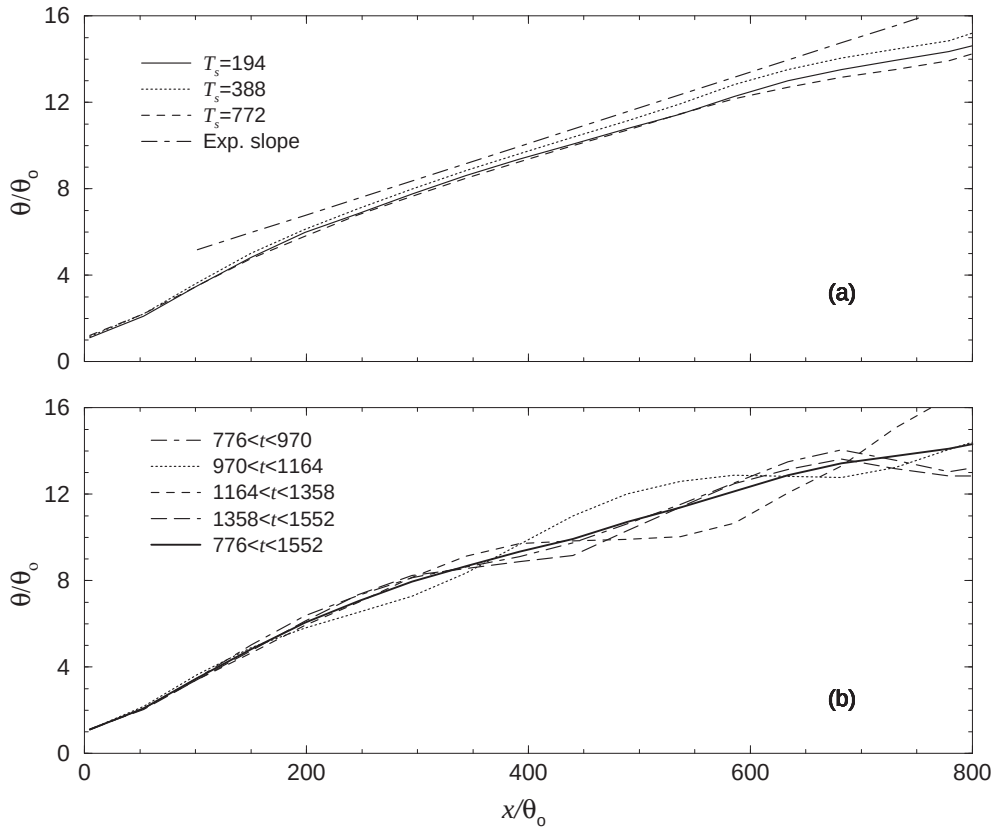

Figure 3.4: Growth of momentum thickness in the mixing layer. Experimental slope is from Loucks [45]. (a) Time average for different inflow condition cases. (b) Averages over different periods of case 3.

To quantify the loss of periodicity, auto-correlations of the streamwise velocity fluctuations were calculated at several streamwise locations for each case. The auto-correlation is defined as:

$$R_{uu}(x,z,t) = \frac{< u'(\mathbf{x},t')u'(\mathbf{x},t'+t) >}{< u'^2 >^{1/2}}, \tag{3.18}$$

where u' is the streamwise velocity fluctuation and the angle brackets represent averages over time and homogeneous spanwise direction. The results are shown in Fig. 3.5.

At the inflow plane ($x = 0$), when the data is reused, one can expect to see the auto-correlation value going back to 1 as two identical signals are correlated. This can be observed at time $t/T = 0.25, 0.5$ in case 3 and $t/T = 0.5$ in case 2. With distance downstream, the correlations also show secondary peaks at those times. However, the secondary peak values decrease rapidly with increasing downstream distance, which reflects the de-correlation. At $x = 290$, which is at about a quarter of the useful domain from the inflow, the peak values drop to below 0.2.

Finally in Fig. 3.6 some statistics for the mixing layer at two streamwise locations are shown. The first location ($x = 97$) is very close to the inflow plane and the second location ($x = 484$) is in the self-similar region. Both the first order moment (mean velocity) and the second order moment ($q^2 =< u_i' u_i' >$, the trace of the Reynolds stress tensor) from the simulation agree very well with the experiment [45], the initial conditions of which we attempted match.

To give a general idea of the efficiency of this method: in the current test case, the time spent on the auxiliary simulations was about 64% of the main simulation. However, if one is interested in higher order properties of the flow, the main

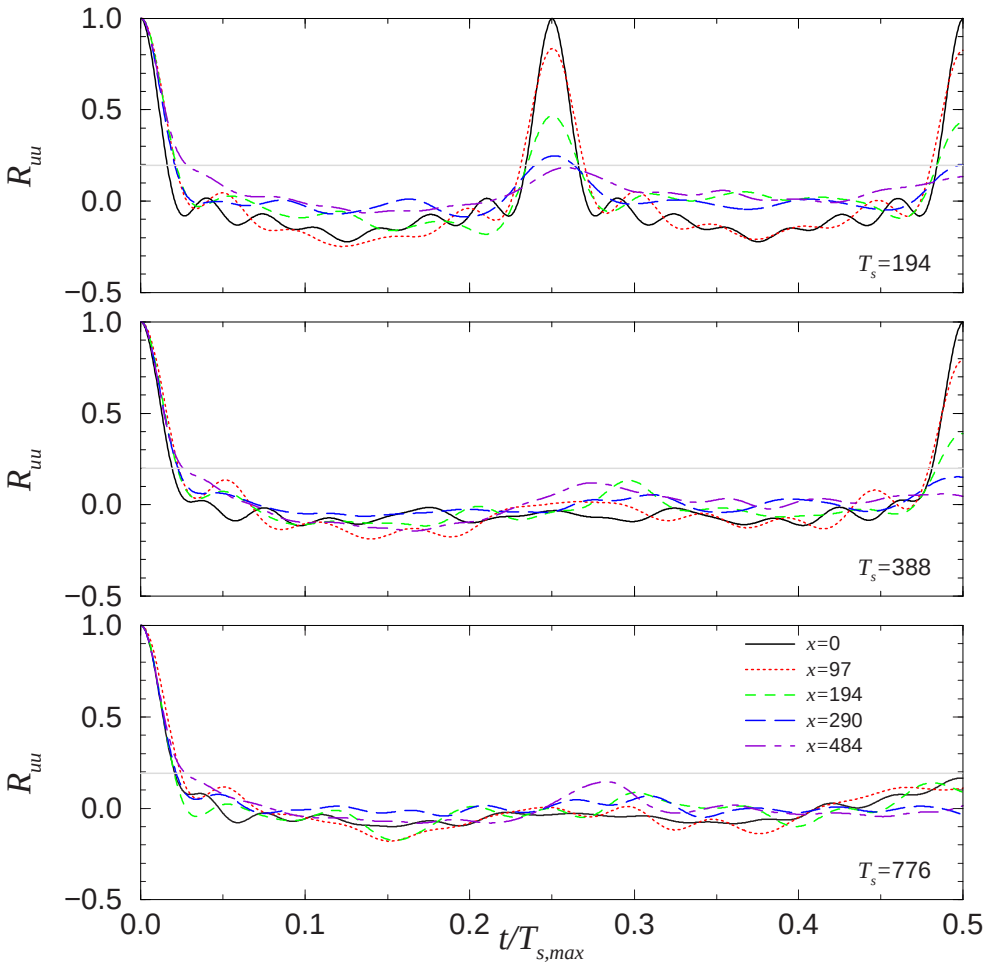

Figure 3.5: Autocorrelations of streamwise velocity fluctuations at several streamwise locations. Top: case 3; Middle: case 2; Bottom: case 1.

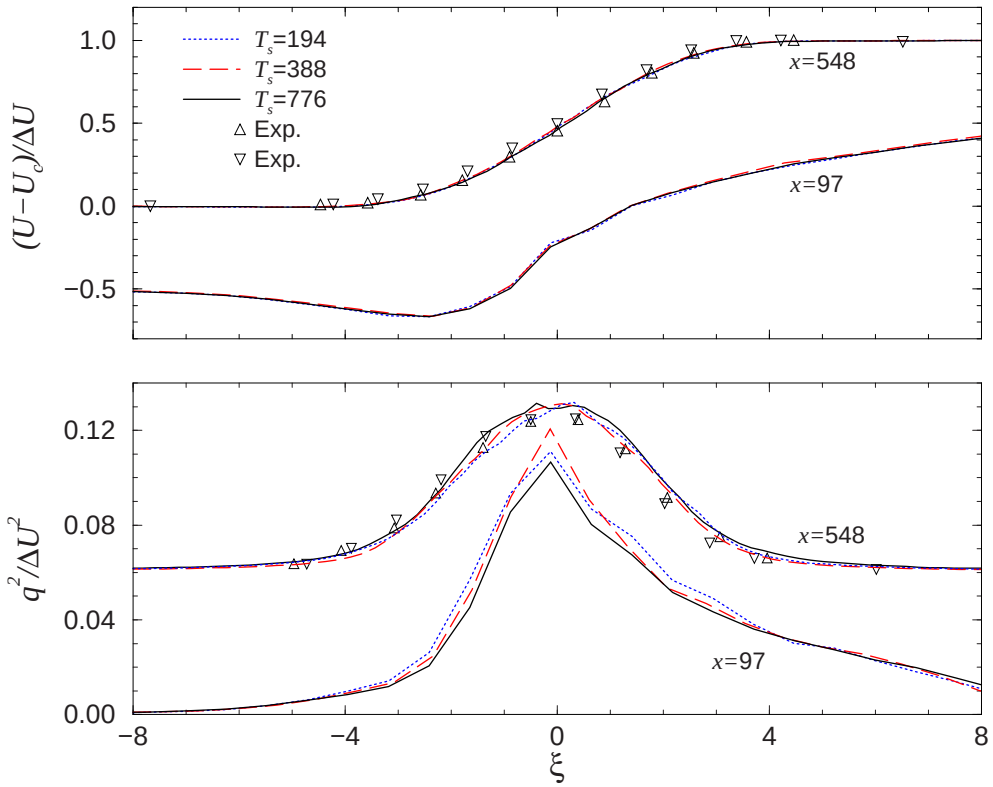

Figure 3.6: First- and second-order moments in the self-similar region of the mixing layer. Experimental data from Loucks [45]. (a) Mean velocity. (b) Trace of Reynolds stress tensor.

simulation needs to run for a much longer time to achieve converged statistics. In that situation, the saving by recycling the inflow data can be significant.

The above method was also tested by [37] in a spatially developing mixing layer in the framework of a finite-difference method. The author suggested that the mechanism to de-correlate the inflow periodicity might be partly from the numerical error of the 2nd order spatial discretization of the code. When a 6-order central difference scheme was used, this mechanism became much weaker.

3.3 Scalar Transport

3.3.1 Problem formulation

The dispersion of passive scalars in a flow field is normally the result of two different physical processes: advection and molecular diffusion. This is clearly described by the following scalar transport equation:

$$\frac{\partial C}{\partial t} + u_j \frac{\partial C}{\partial x_j} = k_c \frac{\partial^2 C}{\partial x_j \partial x_j}, \tag{3.19}$$

where C is the scalar concentration, u_j denotes the velocity and k_c is the molecular diffusivity of the scalar. In the framework of LES, (3.19) can be spatially filtered, resulting in:

$$\frac{\partial \overline{C}}{\partial t} + \overline{u}_j \frac{\partial \overline{C}}{\partial x_j} = k_c \frac{\partial^2 \overline{C}}{\partial x_j \partial x_j} - \frac{\partial Q_j}{\partial x_j}, \tag{3.20}$$

where the overbar denotes a filtered variable and

$$Q_j = \overline{u_j C} - \overline{u}_j \overline{C} \tag{3.21}$$

is the sub-grid scalar flux that has to be modelled.

However, in the present study, the LES approach based on solving (3.20) is prohibitively expensive because of the high Schmidt number of the scalar field. The Schmidt number, defined as

$$Sc = \frac{\nu}{k_c}, \tag{3.22}$$

is a dimensionless measurement of the ratio between the momentum diffusivity ν and the molecular diffusivity k_c. It was estimated [73] that the smoke concentration used in the present study has a Schmidt number of the order of 10^6.

According to the theoretical analysis of Batchelor [10], in an equilibrium state, the smallest scale of the gradient variance of a scalar in a turbulent flow is characterized by:

$$\eta_c = \left(\frac{\nu k_c^2}{\epsilon}\right)^{1/4} = \left(\frac{\nu^3}{\epsilon}\right)^{1/4} \frac{1}{Sc^{1/2}} = \frac{\eta}{Sc^{1/2}}, \tag{3.23}$$

where ϵ denotes the dissipation rate and η is the Kolmogorov length scale. This indicates that a substantially higher spatial resolution ($\sim 10^4$ times finer than the grid resolution used in the present LES study) has to be used to resolve the scalar concentration field.

An alternative approach to study the passive scalar concentration field is to use a particle tracking method, in which massless particles are introduced into the flow and their trajectories are followed. This approach assumes that the scalar is only carried by the particles, and the concentration associated with each particle is conserved along its trajectory. In this case, the scalar concentration at an Eulerian point $\vec{x}$ is represented by the volume-averaged particle number over the neighborhood of $\vec{x}$. Of course, the resolution with which the concentration is determined depends on the size of the volume over which the averaging is done.

Unlike the scalar transport equation (3.19), which has an Eulerian perspective,

it is more convenient to describe the motions of tracer particles from a Lagrangian point of view. The governing equation is:

$$\frac{d\vec{x_p}}{dt} = \vec{u_p} + \vec{b}(t), \tag{3.24}$$

where $\vec{x_p}$ is the position vector of the particle, $\vec{u_p}$ is the particle velocity and $\vec{b}(t)$ is a zero-mean random variable describing the brownian motions of the particles due to the molecular diffusion. The magnitude of $\vec{b}(t)$ is known [3] to be proportional to the molecular diffusivity k_c of the scalar so it is not important in the present study, where the molecular diffusion of the scalar is extremely weak. Thus only the following equation needs to be integrated:

$$\frac{d\vec{x_p}}{dt} = \vec{u_p}. \tag{3.25}$$

Although it is easy to understand that (3.19) and (3.24) describe the same transport physics from different perspectives, the task to mathematically relate them is non-trivial. Readers interested in this topic should consult [64] where the Eulerian view and the Lagrangian view of passive scalar mixing are covered analytically in great detail.

Since the particle locations almost never coincide with the underlying Eulerian grid of the simulations, central to the problem of particle tracking is finding interpolation schemes that are both numerically accurate and cost-effective. This issue will be discussed in the following section. The temporal integration scheme and the procedure adopted to introduce the particles at the inflow plane in a way that closely approximated the experimental conditions will then be described.

3.3.2 Interpolation procedure

In this section two different interpolation strategies to compute the velocity of a particle at an arbitrary grid point are examined: a high order direction-by-direction polynomial interpolation and multidimensional tri-linear and tri-cubic schemes. In the first strategy, multiple-dimensional problems are broken up into a succession of one-dimensional interpolations. To achieve high accuracy, high order polynomials can be used. Polynomial interpolation is a fairly popular method, and has been widely used in particle tracking algorithms (e.g., Wang et al [78]). The second strategy is to achieve high level of smoothness over the multiple-dimensional domain by using nodes from all dimensions together. One such application in particle tracking can be found in [66].

Fifth order polynomial interpolation (direction by direction)

In general, through any N points, there is a unique polynomial of degree $N-1$. Given a set of N points (x_i, y_i) the values of the function $P(x)$ is given by the following Lagrange formula:

$$\begin{aligned} P(x) &= \frac{(x-x_2)(x-x_3)...(x-x_N)}{(x_1-x_2)(x_1-x_3)...(x_1-x_N)}y_1 + \frac{(x-x_1)(x-x_3)...(x-x_N)}{(x_2-x_1)(x_2-x_3)...(x_2-x_N)}y_2 \\ &\quad +... + \frac{(x-x_1)(x-x_2)...(x-x_{N-1})}{(x_N-x_1)(x_N-x_2)...(x_N-x_{N-1})}y_N \end{aligned} \tag{3.26}$$

Directly using the above formula, however, is computationally inefficient. A better way to perform the same interpolation is to use a recursive algorithm to gradually approach the final result. One such algorithm is called Neville's algorithm. Let us assume that there are four tabulated points x_1 through x_4, with

their function values y_1 through y_4, as shown in Fig. 3.7. Neville's algorithm would first build first order approximations (P_{12}, P_{23} and P_{34}) through linear interpolations (or extrapolations) based on tabulated function values. Then the second order approximations (P_{123} and P_{234}) are calculated based on the first order values. The procedure is performed recursively using the following formula:

$$P_{i(i+1)\ldots(i+m)} = \frac{(x - x_{i+m})P_{i(i+1)\ldots(i+m-1)} + (x_i - x)P_{(i+1)(i+2)\ldots(i+m)}}{x_i - x_{i+m}}, \qquad (3.27)$$

until the tip of the pyramid is reached. It can be proved that the recursive method yields exactly the same interpolation result as using the Lagrange formula [71]. However, it is much more efficient. The only disadvantage of this method is that

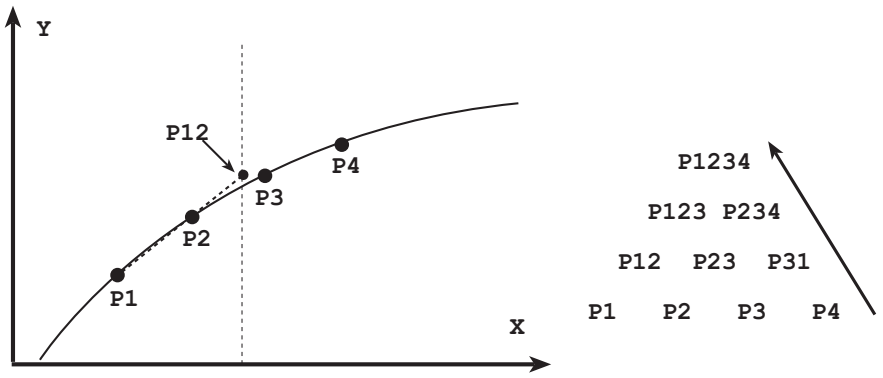

Figure 3.7: Neville's algorithm to perform polynomial interpolation.

the coefficients of the polynomial are not directly obtained and stored, which can increase computational cost.

In the current project, fifth order polynomial interpolations, which involve 6 points in each direction, or $6^3 = 216$ points in three-dimensional domain were used. The interpolation was performed in a direction-by-direction man-

ner, which breaks the three-dimensional interpolation procedure into a number of one-dimensional interpolations. The details are given in Appendix A.

Since the above scheme involves 3 nodes from each side of the particle, special treatment is required near the boundary of the computational box. In the present study one-sided formulae at the same order of accuracy are used.

Tri-linear interpolation and tri-cubic interpolation

In this section a multiple-dimensional interpolation procedure that uses neighboring points in all directions together is given. Two typical schemes are the tri-linear and the tri-cubic scheme. Tri-linear interpolation uses 8 neighboring points, while tri-cubic uses 64 neighboring points. As can be seen from the following discussion, while they are theoretically very similar and also very similar to implement, the differences of the computational costs are substantial.

In the case of tri-linear interpolation, the function value at an arbitrary point can be expressed as:

$$u(x, y, z) = (a + bx)(c + dy)(e + fz), \tag{3.28}$$

ie. it changes linearly in each direction. By expanding the equation above, 8 separate terms are obtained with 8 coefficients to be determined. Note that a grid cell surrounding a particle has exactly 8 corner points, where their function values and coordinates are known. An 8 by 8 linear equation system can be formed to solve for the unknown coefficients. Then, function values at arbitrary locations within that grid cell can be evaluated explicitly.

The tri-cubic interpolation is based on the same idea, except that it use multiplication of cubic functions and involves 4 points on each grid line. It can be

written as:

$$u(x,y,z) = (a_1 + a_2x + a_3x^2 + a_4x^3)(b_1 + b_2y + b_3y^2 + b_4y^3)(c_1 + c_2z + c_3z^2 + c_4z^3). \tag{3.29}$$

Expanding the above equation yields 64 unknown coefficients. To solve for the unknowns, 27 grid cells with 64 nodes have to be involved in the interpolation. As a result, a much larger linear system (64 by 64) has to be solved.

It is obvious that storing the interpolation coefficients in memory, rather than computing them at each time step, would increase substantially the efficiency of the algorithm. The trade-off, however, is that a large amount of storage is required. In the following, the methodology for the specific application will be discussed.

For simplicity let us consider a simplified two-dimensional bilinear interpolation in the form of:

$$\begin{aligned} u(x,y) &= (ax+b)(cx+d) \\ &= acxy + adx + bcy + bd \\ &= c_1xy + c_2x + c_3y + c_4. \end{aligned} \tag{3.30}$$

If a rectangular grid cell (which contains a particle) has four nodes at (x_0, y_0), (x_0, y_1), (x_1, y_0), (x_1, y_1), then in the framework of a bilinear interpolation one has to solve the following linear system:

$$\begin{bmatrix} x_0y_0 & x_0 & y_0 & 1 \\ x_1y_0 & x_1 & y_0 & 1 \\ x_0y_1 & x_0 & y_1 & 1 \\ x_1y_1 & x_1 & y_1 & 1 \end{bmatrix} \begin{bmatrix} c_1 \\ c_2 \\ c_3 \\ c_4 \end{bmatrix} = \begin{bmatrix} u(x_0,y_0) \\ u(x_1,y_0) \\ u(x_0,y_1) \\ u(x_1,y_1) \end{bmatrix}. \tag{3.31}$$

By looking at the equations, it is obvious that the elements in the left-hand-side matrix only contain geometric information about the grid, and the right-hand-side vector only contains function values on grid nodes. This means that once the grid system has been determined, the left-hand-side matrix for each grid cell can be created and the expensive LU decompositions can be performed only once. The right-hand-side vector, in contrast, has to be determined continuously, because the flow field is changing with time. In this case, however, only a rather fast back substitution step is needed to solve the linear systems.

With this procedure, all left-hand-side matrices can be formed, LU decomposed and stored in memory for future use to reduce the computational cost. The storage cost, however, can become a major obstacle. For instance, in the mixing layer, if all the matrices for a tri-cubic scheme were to be stored, the memory usage for a moderate number of grid cells (approximately $600,000$) would be of the order of 10 Gigabytes for a single precision calculation. This is far beyond the ability of most modern workstations.

One possible solution to reduce the storage cost is to take advantage of the grid uniformity in one or more directions. For example, in a simulation with uniform meshes in all directions, all grid cells have exactly the same shape and size. If a relative coordinate system is used (i.e. x, y, z are relative to a origin local to each cell), then the matrices are the same for all grid cells and only one matrix needs to be stored. If one dimension is non-uniform (i.e. y), then only one matrix needs to be stored for each $x - z$ plane.

In the present computations the grid is always uniform in the spanwise homogeneous direction. Referring to the previous example and taking advantage of the grid uniformity in the span, the storage for the tri-cubic scheme can be

reduced to approximately 310 Megabytes. This is a reasonable memory size for many modern PC systems.

There is no special boundary treatment for tri-linear interpolation as it only involves vertices from one grid cell for each particle. For the tri-cubic scheme, similar to the 5th order polynomial, one-sided formula was used.

3.3.3 Time advancement

Time advancement of equation (3.24) is done with an explicit Adams-Bashforth scheme as for the Navier-Stokes equation part. Generally, any explicit time scheme could work well as long as the time steps are small enough. It can be argued that, in particle tracking, numerical errors usually come from interpolation, rather than temporal integration [5].

The integration can be written in the following format:

$$\vec{x}_p^{n+1} = \vec{x}_p^n + \Delta t[(1+\alpha)\vec{u}_p^n - \alpha\vec{u}_p^{n-1}], \tag{3.32}$$

where α equals 0.5 for a normal time step. Note that to calculate the particle displacement at time $n+1$, particle velocities at both time n and time $n-1$ are required. So at the time when a particle is just introduced into the computation domain and no particle velocity history is available, the scheme must be degraded to a first order Eulerian scheme. This is done by setting $\alpha = 0$.

3.3.4 Preliminary assessment of the interpolation schemes

To test the accuracy and efficiency of the different methods, preliminary calculations were performed using a prescribed three-dimensional velocity field that satisfies the Navier-Stokes equations. The domain was discretized using a $64\times64\times64$

grid. The test case was designed so that the domain size, grid size and time step were comparable to those of the final simulation. Fig. 3.8 shows the computational domain and an example of a single particle trajectory.

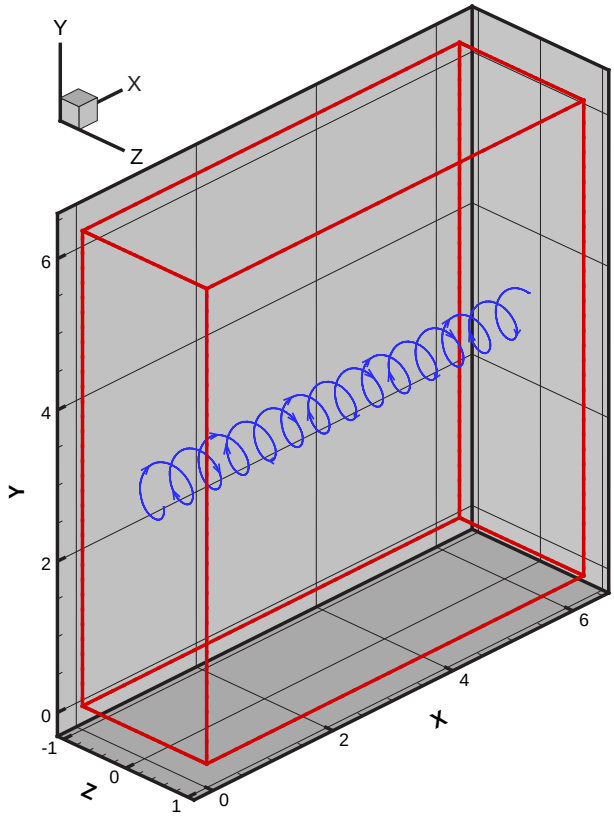

Figure 3.8: Computational domain to assess the interpolation schemes and one particle trajectory.

In the first test case, one particle was allowed to travel the whole length of the computational box and it was tracked by three different interpolation schemes using the same conditions (identical starting point, time step and grid resolution).

The end positions of the particle ($\vec{x}_{num}$) after 3000 time steps were compared to the analytical solution ($\vec{x}_{ana}$). The result is shown in the second column of table 3.1, and the numbers are reported as the ratio of the error $|\vec{x}_{num} - \vec{x}_{ana}|$ to the uniform grid size Δ. All schemes produced satisfactory results and the maximum error is only 6% of the grid size. The tri-cubic scheme appeared to be one order of magnitude more accurate than the other two schemes. Although the polynomial scheme uses more stencils (216 nodes) than the other two schemes, its direction-by-direction nature appears to reduce its accuracy.

In the second test case, the times needed to perform $300,000$ interpolations using the three schemes were recorded. They are normalized by the time used by the tri-linear scheme t_{min} and reported in the third column of table 3.1. It can be seen that the tri-cubic scheme is prohibitively expensive due to its need to solve a huge linear system. The tri-linear scheme is by far the fastest.

The idea of speeding up the interpolation process by storing the interpolation coefficients was also evaluated in a preliminary mixing layer simulation. The gain of computational time is highly dependent on the number of particles in use – the more particles sitting in the same grid cell, the more effective this idea is. With

Table 3.1: Accuracy and efficiency of the interpolation schemes.

Interpolation Scheme	$\lvert\vec{x}_{num} - \vec{x}_{ana}\rvert/\Delta$	t/t_{min}
5th order polynomial	6.17%	4.6
Tri-linear	4.47%	1.0
Tri-cubic	0.52%	96.4

1 million particles and a moderate grid (500,000 cells), 2/3 of the CPU time was saved using the tri-linear scheme.

Based on the analysis above, the tri-linear scheme, which has the overall best performance, was chosen in the final simulation.

3.4 Setup of the Computations

In this section details of the setup of the mixing layer computations are given. A key point in simulating the experiment described in the previous chapter is the boundary condition at the inflow plane in the simulations. The auxiliary boundary layer LES, used to generate the inflow data are discussed in detail in section 3.4.1. Other parameters that could affect the results, like the domain size and numerical resolution are examined in section 3.4.2.

3.4.1 Auxiliary boundary layer simulations

As mentioned in the previous sections, measurements of the mean velocity profiles exactly at the trailing edge of the splitter plate were conducted for the purpose of providing the required information to construct accurate inflow conditions for the LES. The presence of a zero pressure gradient boundary layer is clear on the high-speed side, while on the low-speed side a relative weak adverse pressure gradient is apparent. The ratio of the free-stream velocities of the two boundary layers is $u_{\infty H}/u_{\infty L} = 1.95$ (henceforth the subscript H refers to quantities on the high-speed side and the subscript L to quantities on the low-speed side), and the ratio of the displacement thickness is $\delta^*_H/\delta^*_L = 0.44$. The corresponding Reynolds numbers are $Re_H = u_{\infty H}\delta^*_H/\nu = 680$ and $Re_L = u_{\infty L}\delta^*_L/\nu = 800$. Also

henceforth and unless otherwise stated the displacement thickness δ_L^* and the free-stream velocity $u_{\infty L}$ will be used as the reference length and velocity scales.

To be able to construct inflow conditions using the method described in section 3.2 two separate boundary layer computations were conducted mimicking the conditions of the low-speed and high-speed side in the experiment. The simulations were performed on $200\delta^* \times 40\delta^* \times 35\delta^*$ computational domains, with $256 \times 96 \times 48$ grid nodes in the streamwise, spanwise and wall-normal directions, respectively. The streamwise and spanwise grids were uniform, while the wall-normal grid was stretched using a hyperbolic tangent function. The size of the computational box in the spanwise direction was the same as the planned mixing layer simulation, while in the wall-normal direction the size was half of that in the mixing layer simulation. The boundary layer simulations were conducted using the rescaling method by Lund et. al. [46].

By adjusting the inflow flow parameters, the boundary layers were controlled to have the desired thicknesses in the middle of the computational domain ($x/\delta^* = 100$), where the flow field is least affected by the boundary conditions. Instantaneous $y - z$ planes of velocity data were taken from there and stored on the disk. Based on the experience from the preliminary study in section 3.2, the time period of the stored data was about $240tu_\infty/\delta^*$. Within this time period, a fluid particle travelling at the mixing layer centerline velocity would move out of the computational domain from the outflow boundary.

To evaluate the accuracy of the auxiliary boundary layer LES, comparisons with the DNS result of Spalart [68] at a similar Reynolds number were made. Fig 3.9 shows the mean velocity profiles that match the DNS profile very well. In the LES the first point from the wall was located at $y^+ = 0.9$ for the low-speed side

and $y^+ = 1.6$ for the high-speed side.

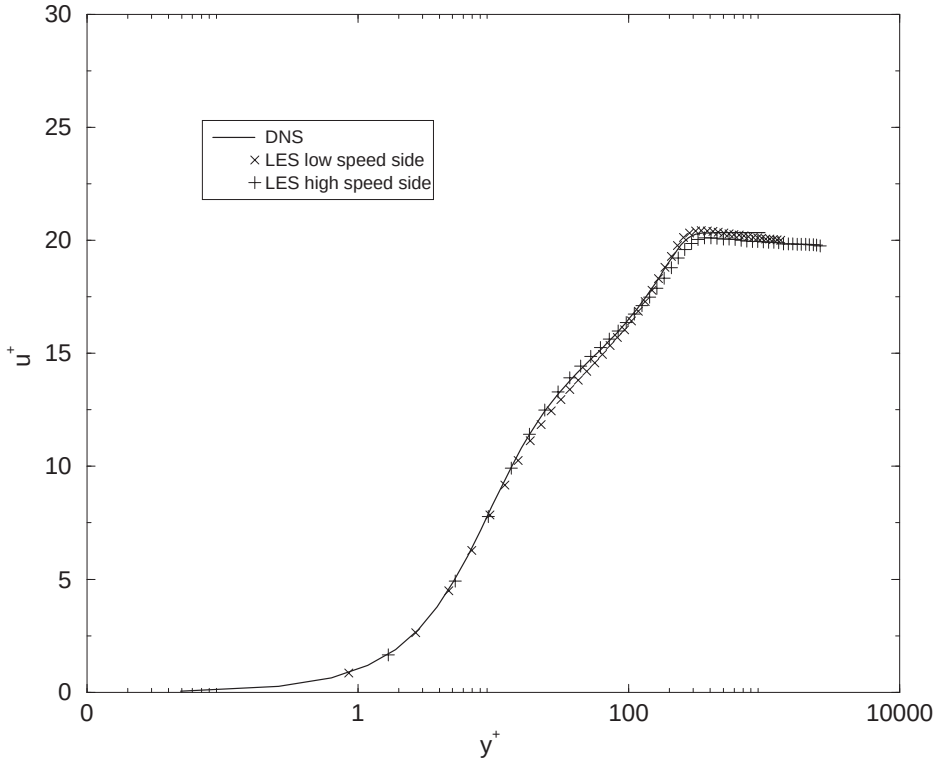

Figure 3.9: Comparison of mean velocity profiles of the boundary layer simulations.

Shown in Fig 3.10 are the root-mean-square profiles of the three velocity components in inner coordinates. As expected for marginally resolved LES, the u_{rms} values were slightly over-predicted in the near-wall region, while v_{rms} and w_{rms} were slightly under-predicted. Nevertheless, for the purpose of constructing inflow conditions for the mixing layer simulation, such accuracy is more than adequate.

The slice data from both high-speed and low-speed sides were then interpo-

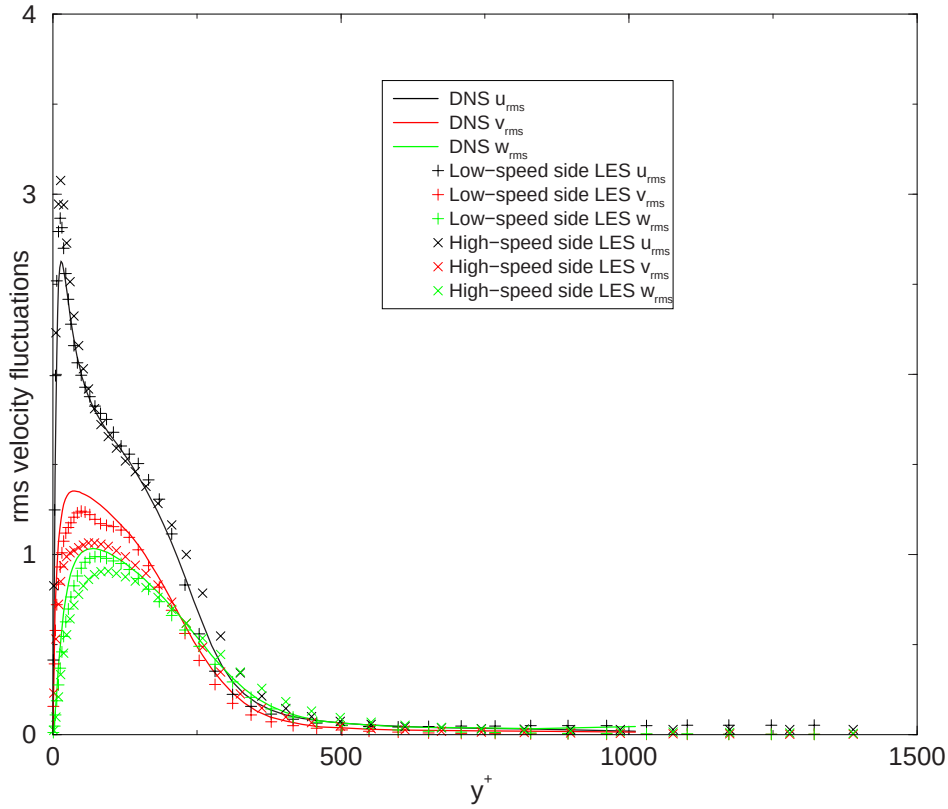

Figure 3.10: Comparison of velocity rms profiles of the boundary layer simulations.

lated on the mixing layer grid to be used as inflow boundary conditions following the procedure described in section 3.2. The resulting mean velocity profile at the inflow is compared to the measured one in Fig. 3.11, where it is seen that the agreement is excellent.

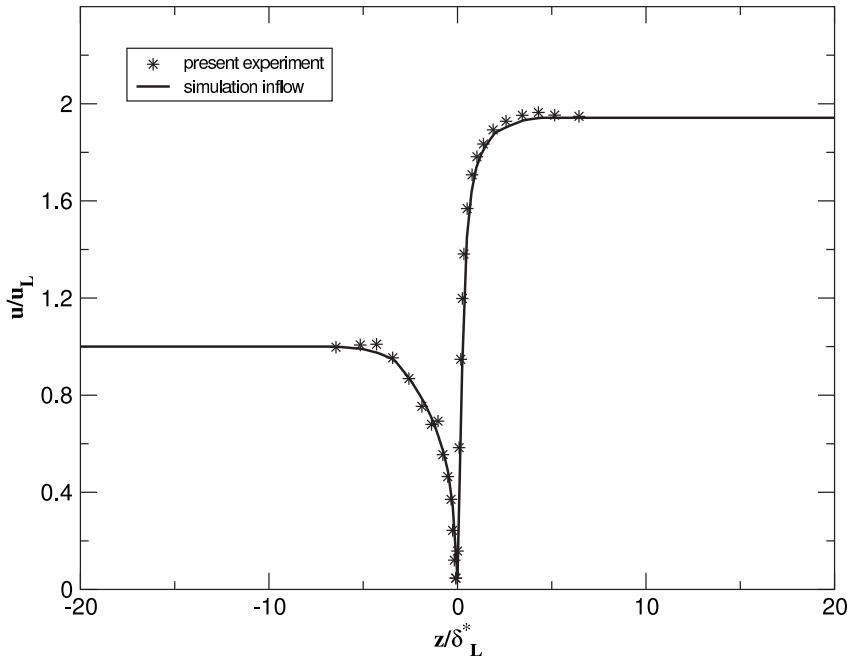

Figure 3.11: Inflow boundary condition for the mixing layer simulation.

The specification of inflow concentration conditions for the simulation is as important as its velocity counterpart. In the present experimental study, the smoke was injected from a slot into the high-speed side boundary layer. The slot is about $200mm$ upstream of the splitter plate trailing edge. There was no

direct measurements of the concentration profiles at the splitter plate trailing edge plane.

To provide realistic inflow concentration conditions for the simulation, Chiang's [20] experimental results were used for guidance. Chiang performed an experiment measuring the smoke concentration in a turbulent boundary layer downstream of a line source. The way the scalar was generated and transported in his experiment is quite similar to that of the current experiment. Fig 3.12 shows typical mean concentration and concentration variance profiles from his measurements.

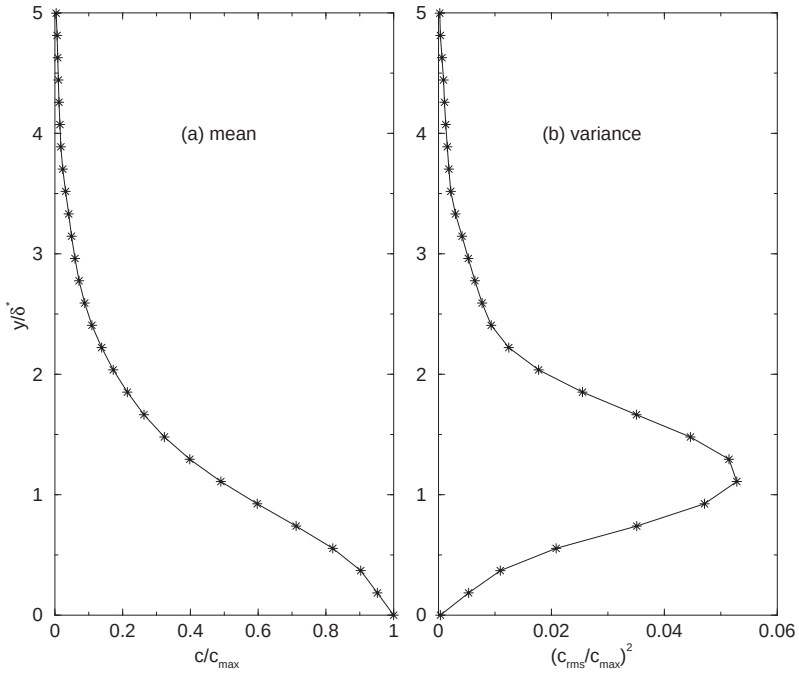

Figure 3.12: Concentration measurement [20] in a turbulent boundary layer. (a) Mean profile; (b) Variance profile.

To simulate the way that concentration changes with time at the mixing layer

inflow, at each cross-stream location a random number generator was used to generate time series that statistically gave the desired mean and variance values that match the experimental profiles. These numbers were then translated into number of particles needed for each cross-stream level. The desired number of particles were seeded randomly into the first and second column of grid cells at each time step of the simulation to provide the inflow concentration information. This method gave reasonable downstream statistics in this simulation.

3.4.2 Computational domain, grid refinement, sample size and particle number issues

A previous temporal LES by Balaras et. al. [7] has shown that the mixing layer statistics are very sensitive to the size of the computational box, especially in the spanwise direction. This simulation was used as a guide when choosing the domain size and the grid resolution in the spanwise and cross-stream directions for the current numerical simulation. The experimental results on the growth of the mixing layer provided helpful information to determine the box size in the streamwise direction.

The domain size of the final computation is $350\delta^* \times 40\delta^* \times 70\delta^*$ (the displacement thickness δ^* of the precursor low-speed boundary layer simulation is the length scale for discussions in this section). The temporal LES indicated that a grid resolution of 96×96 in $y - z$ planes is sufficient for this box size. In the streamwise direction, three different grids were tested to investigate the influence of grid resolution.

Fig. 3.13 illustrates the different streamwise grids. In one case a uniform grid

was used and in two other cases finer grids near the inflow plane were used. From the same starting field and with the same boundary conditions, simulations were performed on all three grids, and their statistics were compared.

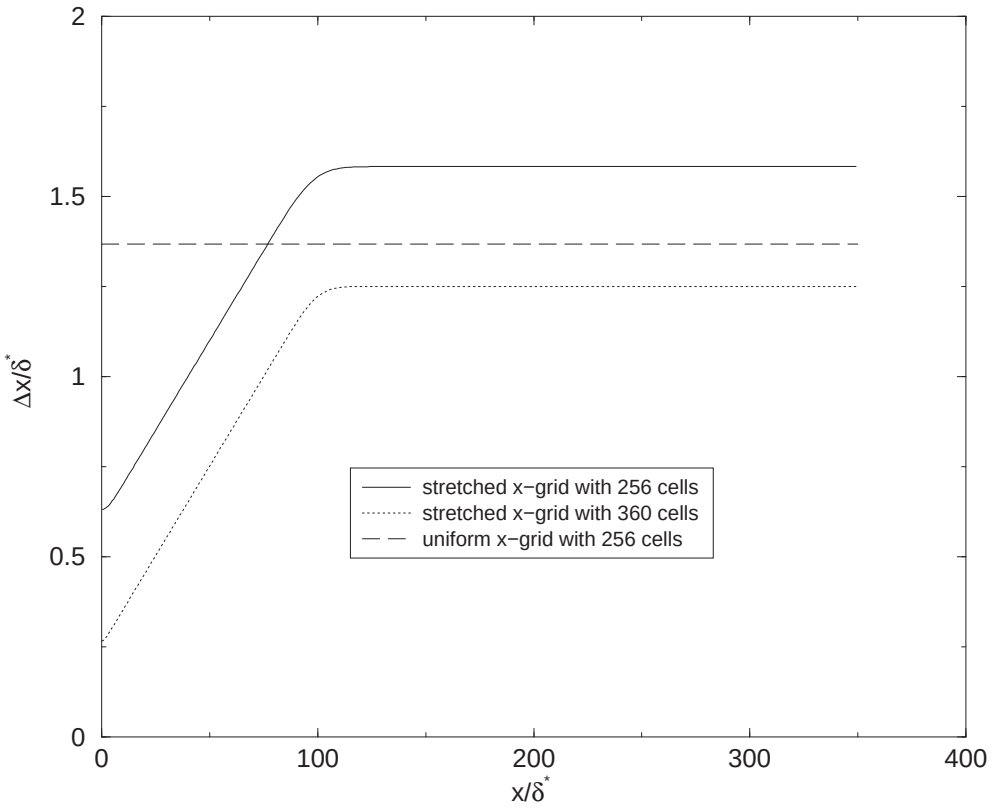

Figure 3.13: Three sets of grids used for the grid refinement test.

Fig. 3.14 shows the growth of the mixing layer. It is evident that the coarser uniform grid case does not have enough grid resolution near the inflow plane, thus leading to poor prediction of the growth of the mixing layer. The other two grids, however, give about the same growth rate. The small difference between them is due to sample size of the statistics.

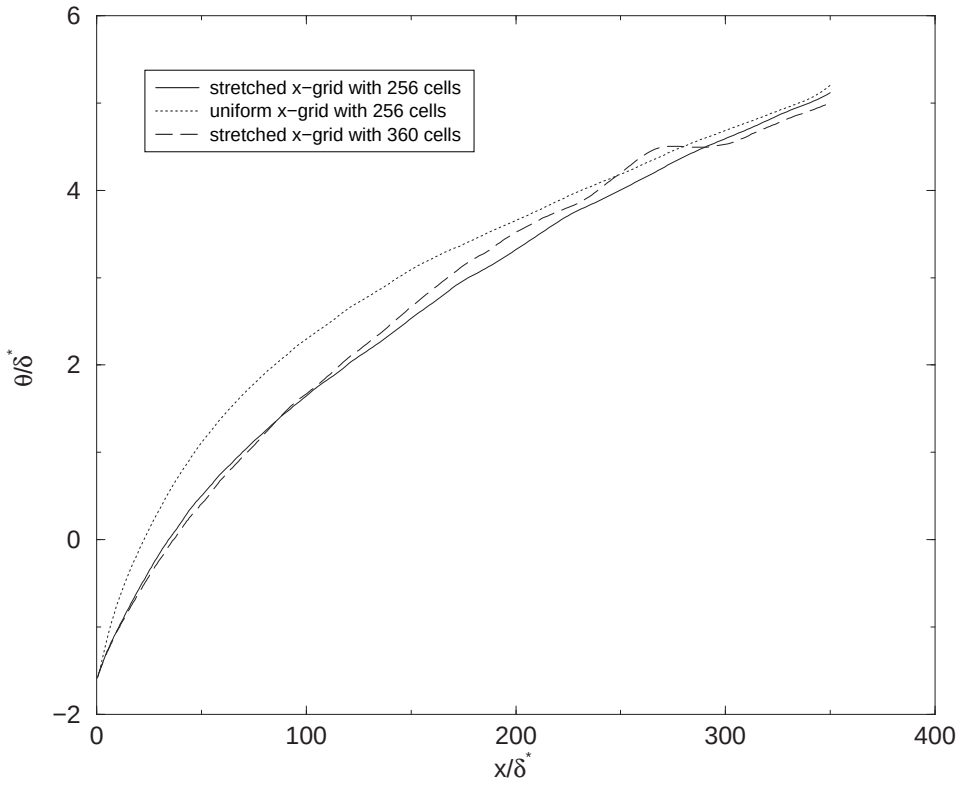

Figure 3.14: Grid refinement test: growth of momentum thickness.

Velocity statistics at a cross-stream section of the mixing layer in the self-similar region are shown in Fig. 3.15. While all three cases identically predicted the mean velocity, the prediction of velocity fluctuation variances for the coarser uniform grid case deviate from the other two, which are almost identical.

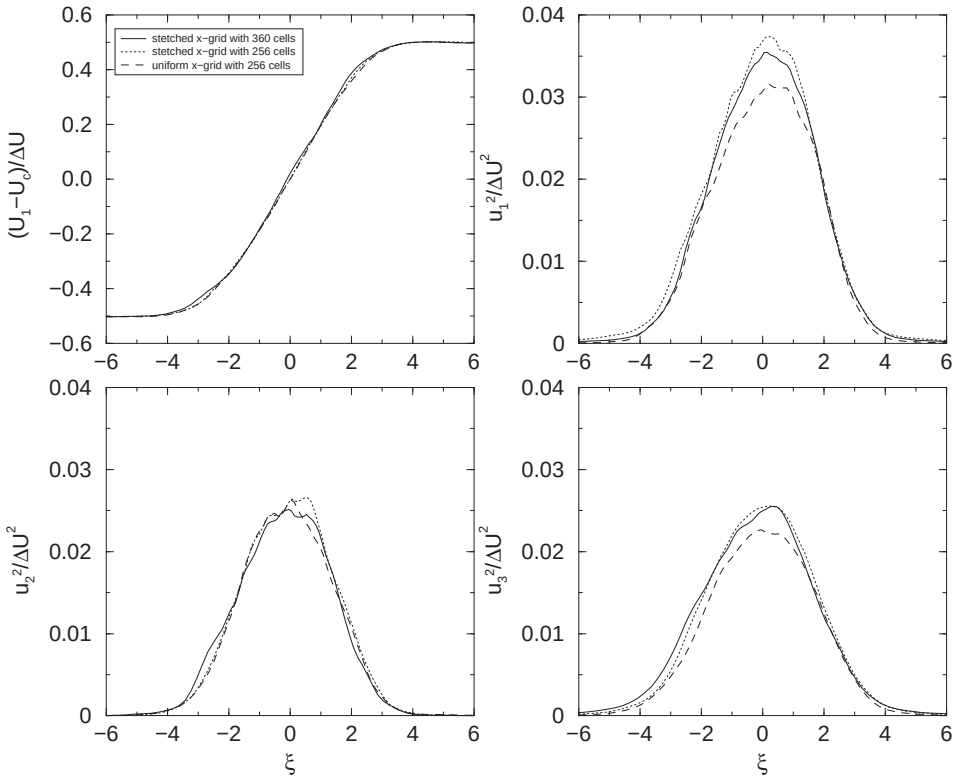

Figure 3.15: Grid refinement test: mean velocity and velocity variances.

As a result of the above analysis, the coarse uniform grid was first excluded from further calculations. Given the agreement between the results on the two non-uniform grids, it was assumed that the intermediate grid ($256 \times 96 \times 96$) provided adequate resolution and was used in the definitive simulation.

Initially a LES without particle tracking was performed to obtain a veloc-

ity field, which was independent of the initial conditions. Then particles were released from the inflow plane at each time step and allowed to disperse for 10,000 time steps (about 3.7 flow-through times). Statistics were accumulated over 15,000 time steps. Sampling over 2,000 - 15,000 time steps indicates that second-order concentration statistics, e.g. the rms of the concentration fluctuations, become very well converged after about 10,000 time steps, as shown in Fig. 3.16.

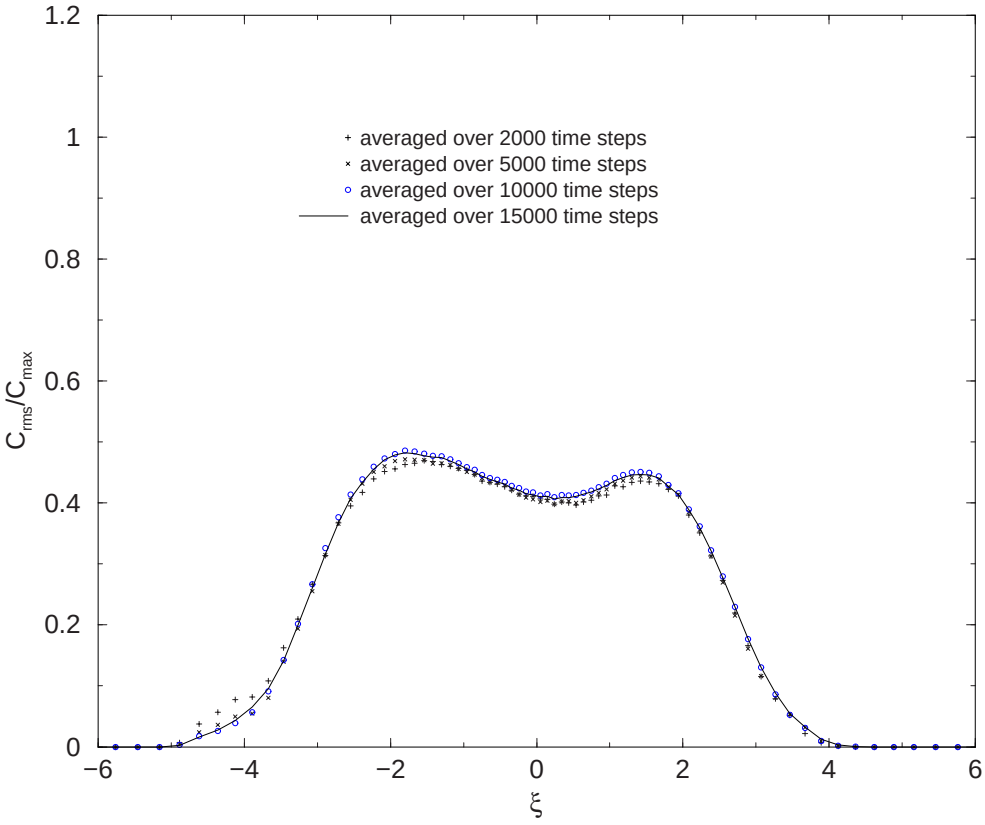

Figure 3.16: Sample size test: statistics over 10,000 time steps (3.7 flow-through time) is very well converged.

It is also very important to evaluate the effect of the total number of particles on the concentration statistics. Three test cases were conducted with the same grid resolution for the velocity field but with different numbers of particles: 4 million, 8 million and 12 million. Fig. 3.17 shows that the rms of the concentration fluctuations converges reasonably well using 8 million particles. With 4-million particles, however, the concentration fluctuation rms was significantly over-predicted. In this case there were only, on average, about 10 particles per grid cell.

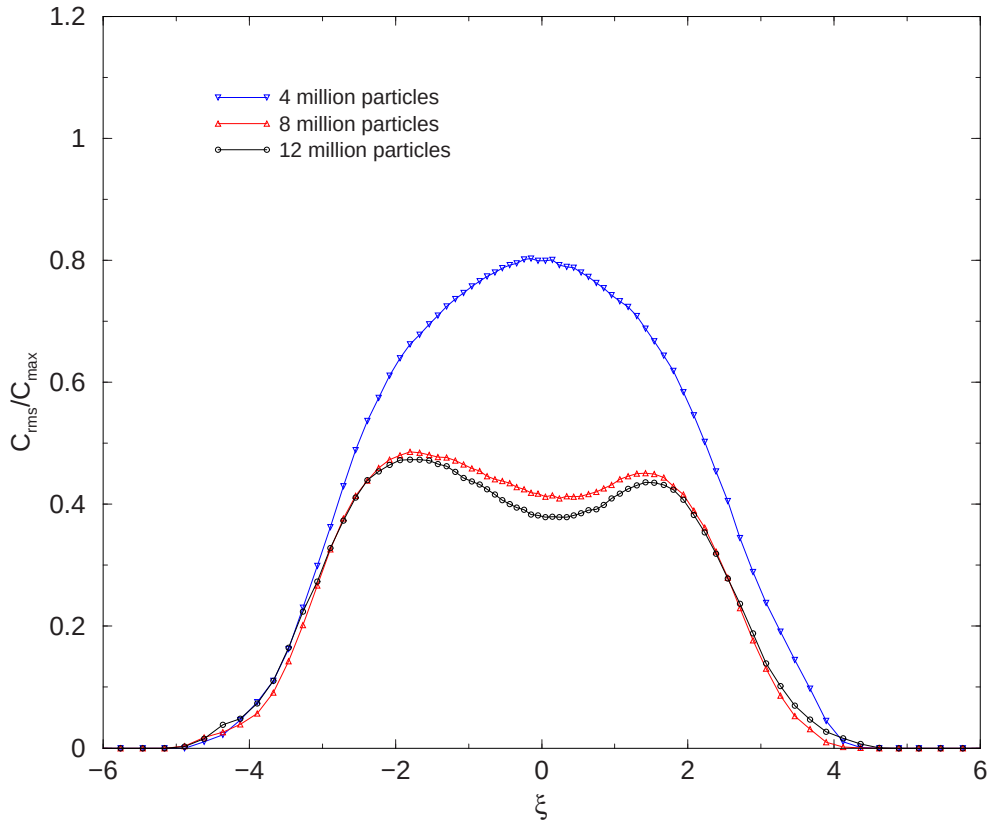

Figure 3.17: The dependence of the root-mean-square of the concentration fluctuations on the number of particles tracked in the simulation.

Finally, it should be mentioned here that the volume over which the particle number density is determined (not necessarily the same as the LES grid) has a very large impact on the concentration statistics. This issue will be addressed in section 4.3, where the scalar concentration results are presented.

3.5 Mixing Layer Integral Properties

In Fig. 3.18 the streamwise evolution of the momentum thickness, θ, of the mixing layer is shown. It is computed from the spanwise-average and time-average of 1000 instantaneous fields using (2.23). As a length scale, the momentum thickness

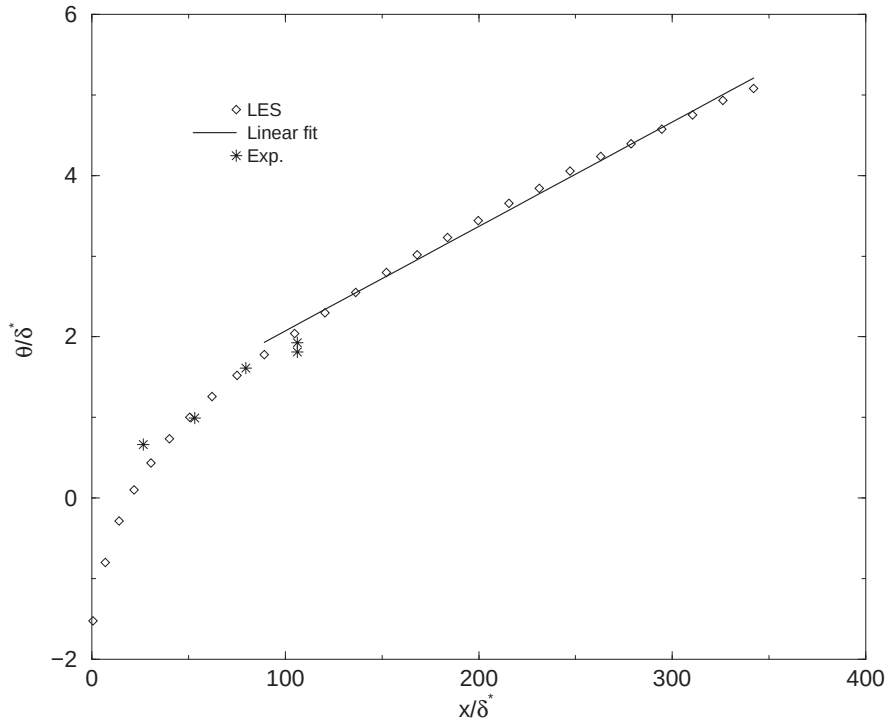

Figure 3.18: Evolution of momentum thickness of the mixing layer. The solid line is a linear fit based on data points beyond $x = 100$.

should always have positive values. However, in the wake of the splitter plate, because of the deficit of the streamwise velocity near the center line, (2.23) can yield negative values. This is true in the present study when the low-speed boundary layer is almost twice as thick as the high-speed boundary layer. The definition of the momentum thickness in (2.23) is for a mixing layer and does not have a clear physical meaning near the edge of the splitter plate where the two boundary layers merge.

After an initial adjustment, the growth of the mixing layer becomes linear at around $x = 100$, suggesting that a self-similar state is reached. The linear section (showing as a fitted line) has a slope of $d\theta/dx = 0.013$. This agrees very well with the present experimental slope. The Reynolds number range of the linear growth region is $1500 - 3900$ (using the local momentum thickness as the length scale and ΔU as velocity scale), with the experimental Reynolds number (1590) near the lower end. In chapter 4, the experimental and LES results will be compared with several references which are listed here in Table 3.2 [1].

Another clear way to identify the self-similar state of the mixing layer is to observe the rate of dissipation of turbulent kinetic energy. This quantity is approximately constant in the streamwise direction in the self-similar region when properly scaled [62]. It is defined as:

$$< \epsilon(x) >= \frac{1}{TL_z} \int_0^T \int_0^{L_z} \int_0^{L_y} \epsilon \, dy \, dz \, dt, \tag{3.33}$$

which is a function of x, averaged in time and spanwise, and integrated in the

[1] Bell and Metha's experiment used length scales other that the momentum thickness. So the numbers shown here are approximations.

Table 3.2: Mixing layer parameters comparison between the current study and some references.

	Re_θ	$d\theta/dx$
Present Experimental Study	1,590	0.013
Present Numerical Study (LES)	1,500-3,900	0.013
Loucks [45]	2,483 1,792 432	0.016
Bell & Metha [12]	2,800 1,900 1,570	0.010
Rogers & Moser (DNS) [62]	1,500-2,000	0.014

cross-stream direction. The integrand is defined as:

$$\epsilon = 2\nu\overline{S}_{ij}\overline{S}_{ij} - \tau_{ij}\overline{S}_{ij}, \tag{3.34}$$

where $\overline{S}_{ij}$ is the resolved strain rate and τ_{ij} is the subgrid-scale stress from the SGS model. The total dissipation rate consists of two parts – the resolved part and the subgrid-scale part.

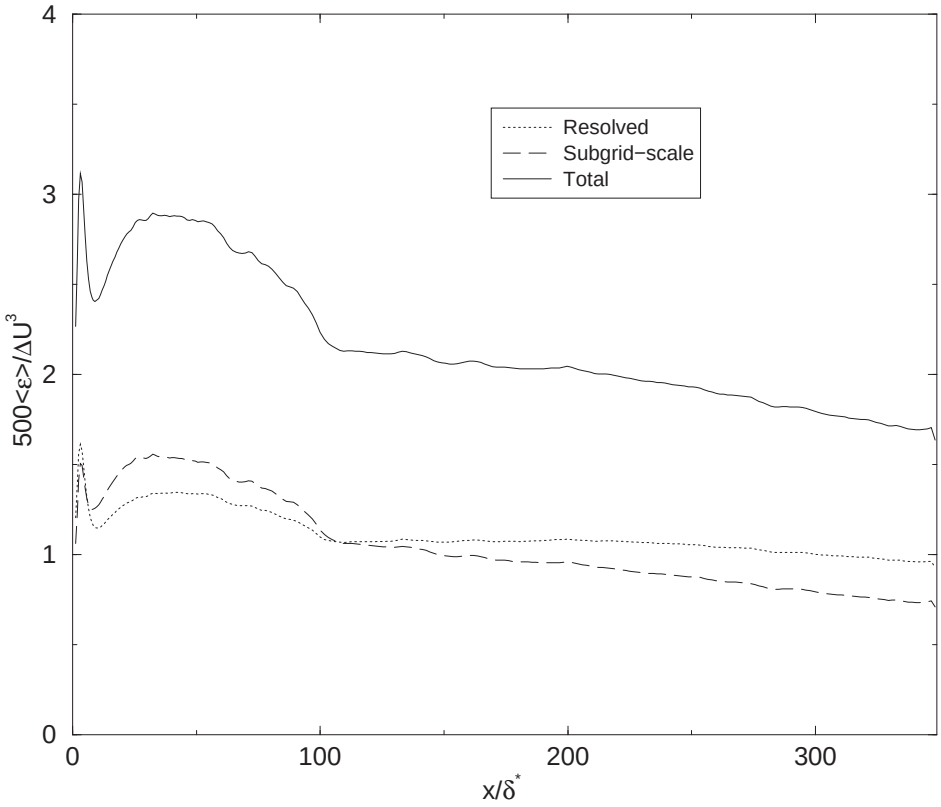

Figure 3.19: Evolution of dissipation rate of the mixing layer.

This quantity can be normalized by the velocity scale ΔU^3 and becomes nearly constant in the self-similar region as shown in Fig. 3.19. It is clear that the flow enters a self-similar state from around $x = 100$, which agrees with the value

obtained from the momentum thickness plot but is much easier to identify. The magnitudes of the resolved part and the subgrid-scale part are almost the same. The total dissipation rate in the self-similar region is about $\langle\epsilon\rangle / \Delta U^3 = 0.004$, which matches the rate from the temporal simulation of [7] very well.

Chapter 4

Results of Experiment and Large-Eddy Simulations

In the previous two chapters, the design, facility, instrumentation, procedure and data processing of the mixing layer experiment and large-eddy simulations were covered. This chapter will present the results from both the experiments and the simulations. Various mathematical and statistical tools were used to analyze the data. When appropriate, they will be discussed along with the results.

4.1 Velocity Statistics

To describe the velocity field statistical characteristics of the mixing layer, a set of standard statistical tools were used. They are:

$$\overline{a} = \frac{1}{N} \sum_{n=1}^{N} a_n, \tag{4.1}$$

the mean value,

$$\sigma^2 = \frac{1}{N-1} \sum_{n=1}^{N} (a_n - \overline{a})^2, \tag{4.2}$$

the variance, which is a measure of how the variable fluctuates about the mean value,

$$S = \frac{1}{N}\sum_{n=1}^{N}(\frac{a_n - \overline{a}}{\sigma})^3, \tag{4.3}$$

the skewness factor, which characterizes the asymmetry of the variable's distribution about the mean value, and

$$K = \frac{1}{N}\sum_{n=1}^{N}(\frac{a_n - \overline{a}}{\sigma})^4, \tag{4.4}$$

the flatness factor (or Kurtosis), which describes how extreme values affect the shape of the probability distribution of the variable. In these definitions σ is the standard deviation of the variable's fluctuations about its mean.

Fig. 4.1 shows the mean streamwise velocity profile and the root-mean-square (rms) values of the three velocity fluctuation components for locations $\xi = y/\theta$ across the mixing layer. The experimental results of the present study (shown as filled circles) and the LES results (shown as dotted, long-dashed and short-dashed curves for three self-similar streamwise locations) are compared with published results. The mean velocity profiles collapse extremely well for all cases. The rms distributions also collapse reasonably well except that the peak of v_{rms} is somewhat higher for the present experiment and LES compared to the other experiments and to the Rogers and Moser [62] DNS. The width of the v_{rms} profile for the experiment is greater than for the simulations but agrees well with the previous experiment of Loucks [45] in the same flow facility. The generally good data collapse indicates that all the data compared are from self-similar mixing layer states.

Fig. 4.2 shows the skewness and flatness factors of the three velocity fluctuations; The agreement with Loucks' experiment [45] at a similar Reynolds number

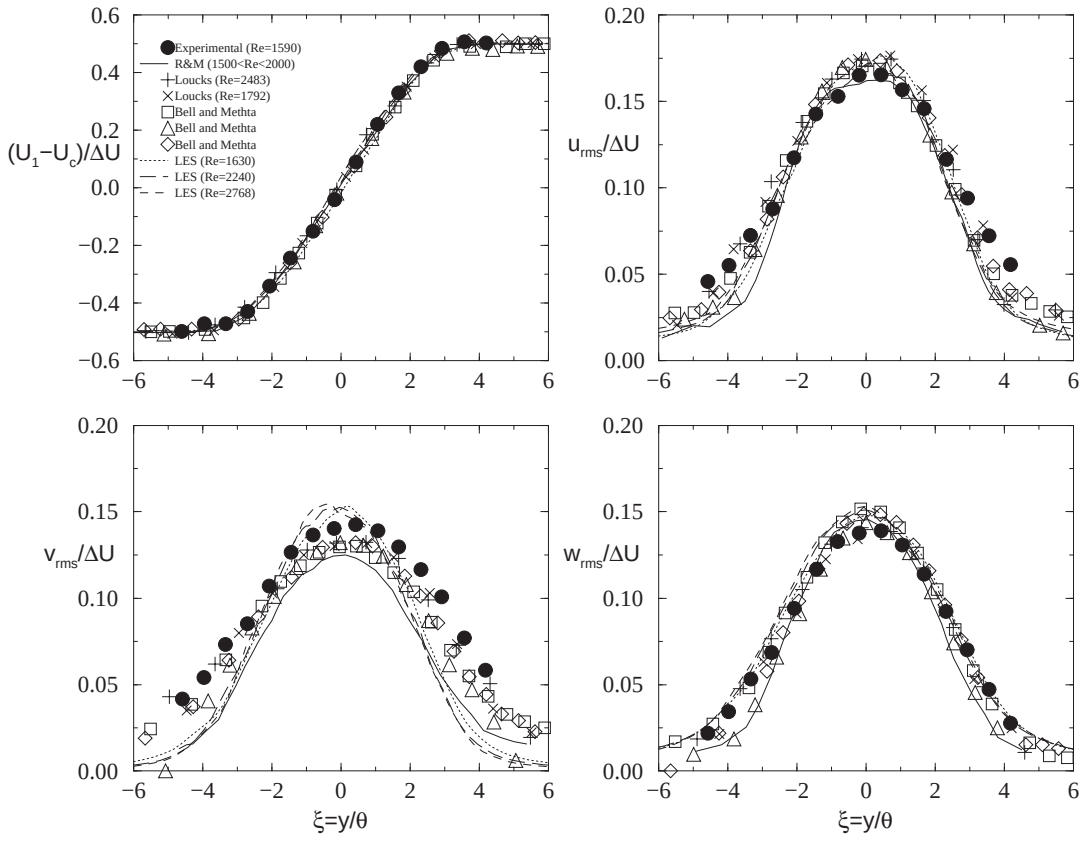

Figure 4.1: Velocity statistics: (a) mean streamwise velocity; (b) streamwise, (c) cross-stream, and (d) spanwise velocity fluctuation root-mean-square values. All data normalized with ΔU.

is quite good.

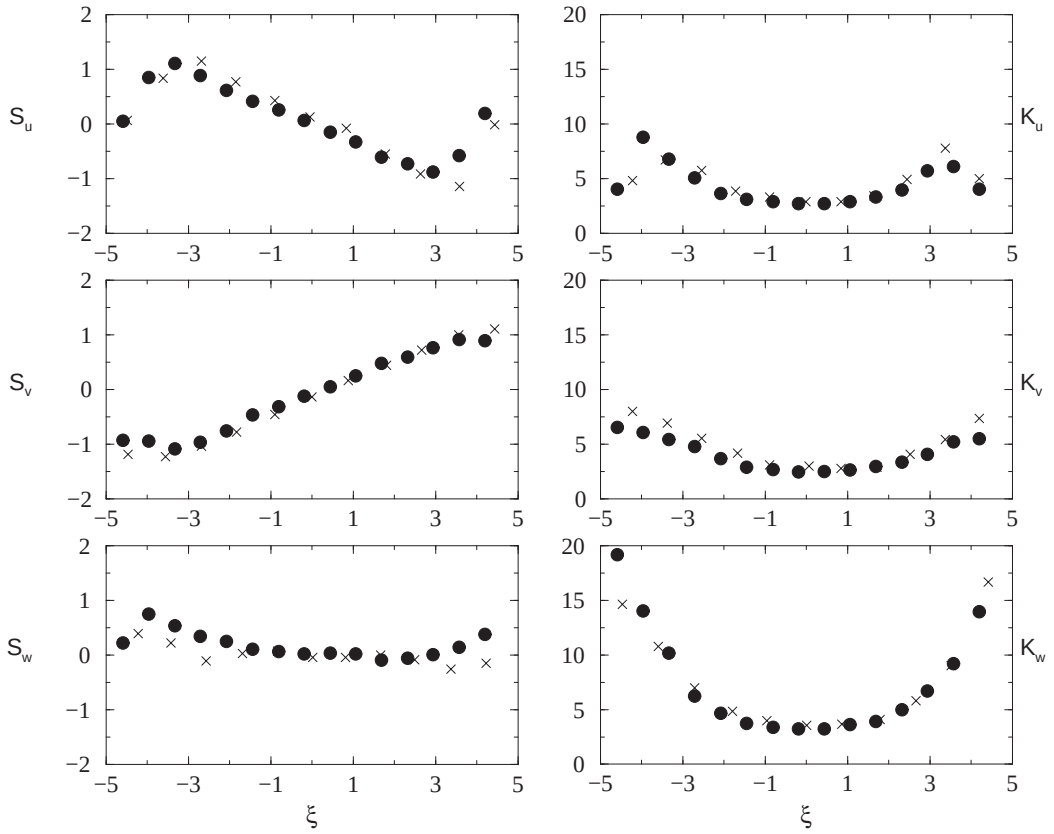

Figure 4.2: Skewness (left column) and flatness (right column) factors of the three velocity fluctuations. Present data: •, $Re_\theta = 1590$; Loucks [45]: ×, $Re_\theta = 1792$.

4.2 Vorticity Statistics

The 12-sensor hot-wire measurements provided three velocity components and six velocity gradients. The three streamwise gradients are not measured directly;

they must be determined using Taylor's hypothesis, i.e.

$$\frac{\partial U_i}{\partial x} = -\frac{1}{U}\frac{\partial U_i}{\partial t}. \tag{4.5}$$

These gradients can be combined into vorticity components as well as other variables such as strain rate, dissipation rate and enstrophy for further analysis. In practice, the time derivative term in (4.5) is often approximated using a central difference scheme:

$$\frac{\partial U_i}{\partial t} = \frac{U_i^{t+\Delta t} - U_i^{t-\Delta t}}{2\Delta t}. \tag{4.6}$$

Taylor's hypothesis is based on the assumption that, over a sufficiently short time, the flow is 'frozen' and the turbulent diffusion is weak. Thus flow structures are only convected by the mean flow. The validity of this assumption has been probed by several studies [45],[56],[75],[51]. One simple approach to validate the assumption from the 12-sensor probe data is to use the continuity equation to evaluate the streamwise velocity gradient $\partial U/\partial x$:

$$\frac{\partial U}{\partial x} = -\frac{\partial V}{\partial y} - \frac{\partial W}{\partial z}, \tag{4.7}$$

where the two right-hand-side gradient terms are directly measured.

Fig. 4.3 shows a comparison of the streamwise velocity gradient at $\xi = 0$ from both (4.5) and (4.7). The shapes of the curves, which carry phase information of the signal, match reasonably well. The correlation coefficient between these two signals is 0.68.

After obtaining the three streamwise velocity gradients. vorticity components can be calculated using the following definitions:

$$\omega_x = \frac{\partial W}{\partial y} - \frac{\partial V}{\partial z},\ \omega_y = \frac{\partial U}{\partial z} - \frac{\partial W}{\partial x},\ \omega_z = \frac{\partial V}{\partial x} - \frac{\partial U}{\partial y}. \tag{4.8}$$

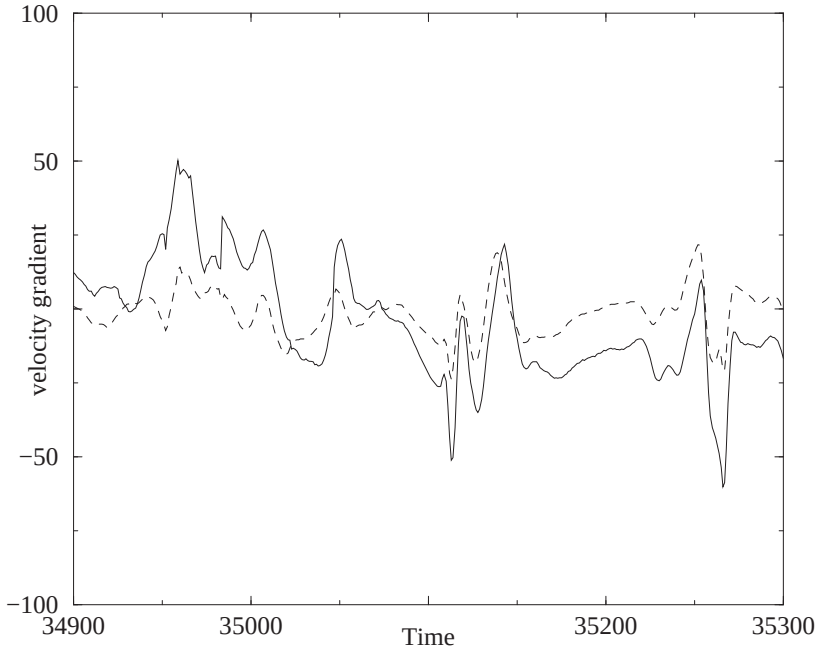

Figure 4.3: Time series of streamwise velocity gradient: $\partial U/\partial x(s^{-1})$ vs. $time(ms)$, from both Taylor's hypothesis and the continuity equation.

Then statistics of vorticity can be calculated.

The normalized root-mean-square values of the vorticity fluctuation components are plotted in Fig. 4.4. The curves are normalized by $(\Delta U^3/\nu\theta)^{1/2}$, which has the unit of s^{-1}.

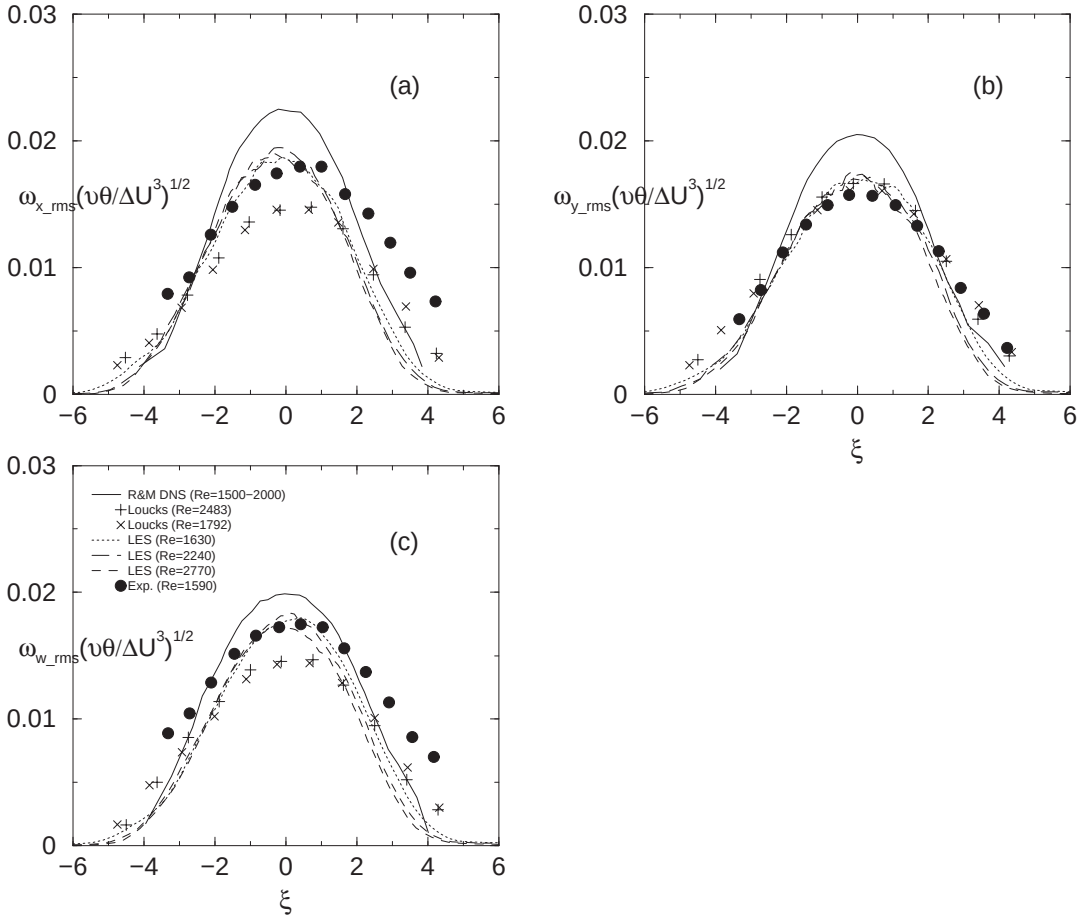

Figure 4.4: Normalized vorticity component root-mean-square values. (a) Streamwise component; (b) Cross-stream component; (c) Spanwise component.

All the vorticity rms profile peaks of Rogers and Moser's DNS temporally developing mixing layer results [62] are greater than the present experimental and

LES profiles. Three reasons why the temporally developing simulation vorticity fluctuation rms do not match well the spatially developing experimental values may be:

- The vorticity profiles at the trailing edge of the splitter plate are not the same for the numerical simulation and the experiments.
- The use of Taylor's hypothesis introduced uncertainties in determining the ω_y and ω_z fluctuations.
- The vorticity gradients in the experiment were determined from a first order finite difference approximation.

Although the present experimental and LES values agree with each other quite well, it should be borne in mind that neither resolves all the small scales and that the LES models them.

4.3 Scalar Concentration Field

Scalar concentration information was obtained experimentally by processing photographic images. Fifteen sets of images were acquired, corresponding to the 15 hot-wire measurement locations. For each set, 1200 photographs were taken. This is a rather small sample size (compared to the measurements of the velocity field, which sampled data for 3 minutes at each location at a frequency of 1K Hz). However, post-processing proved that this sample size is enough to obtain smooth concentration statistics as will be seen.

During the image processing stage, one vertical line of pixels was taken from each image with their gray scale values representing relative smoke concentrations

[73]. This line is in the cross-stream y-direction and just downstream of the tip of the hot-wire probe so that velocity-concentration correlations could be evaluated later. The square area in the illuminated plane corresponding to one pixel was $0.225mm$ on a side. Based on the dissipation rate at a similar Reynolds number found in [45], this is a resolution of about 0.6 Kolmogorov lengths. A pixel is also about 0.019 of the displacement thickness on the low-speed boundary layer at the trailing edge of the splitter plate.

Fig. 4.5 shows the experimental mean concentration profiles and concentration rms profiles. The curves (a) and (b) at the top of the figure are the raw data from 15 separate measurements. The curves share the same shape but have different peak values. This is due to the following factors:

- Smoke accumulated in the room and recirculated through the wind tunnel during the experiment, even with a filter in place at the end of the tunnel that partially removed the smoke.

- The light intensity possibly changed somewhat during the experiment.

Because the full run of the experiment took up to 12 hours, these effects were significant and could not be eliminated with the experimental facilities available. They had to be accounted for in post-processing.

A simple way to deal with this problem is to normalize each curve by its local maximum value. The results of this normalization are shown Fig. 4.5. Both the mean and rms profiles collapse fairly well, as seen parts (c) and (d) of the figure. Ideally the mean flux of scalar through a cross-stream plane should be constant. In fact, during the many hours of the experiment smoke accumulated and was recycled through the tunnel, so that the mean scalar flux was not constant. Thus,

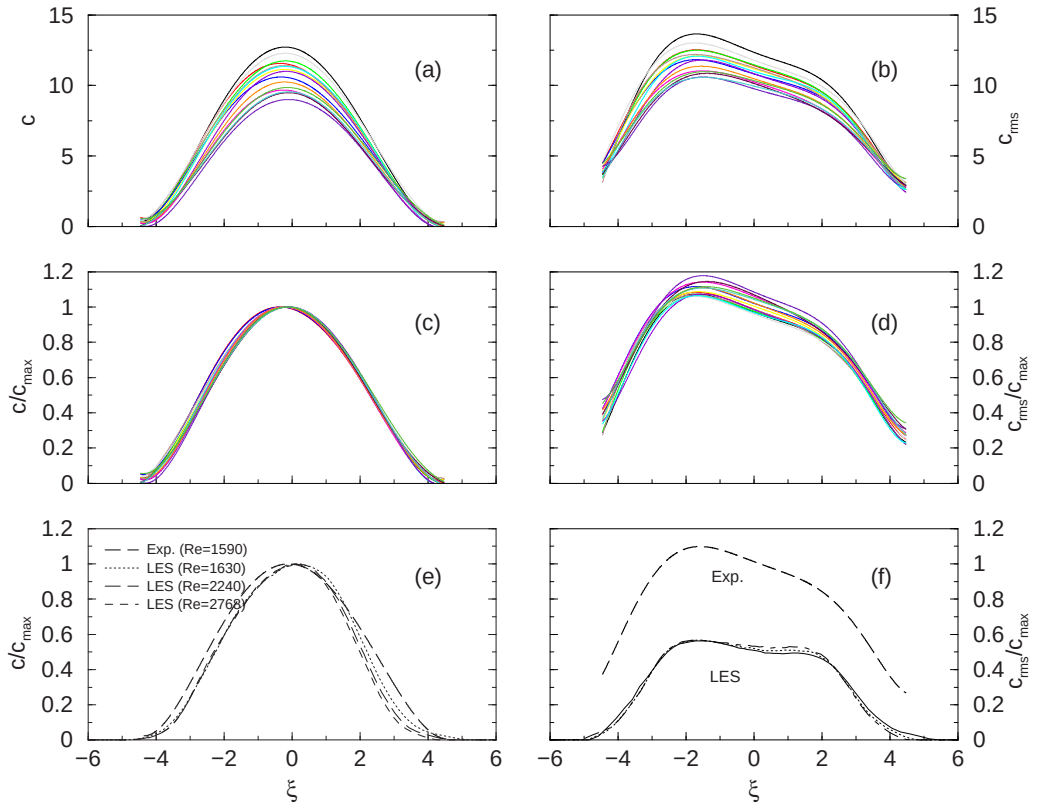

Figure 4.5: Mean and rms concentration profiles. (a) and (b) Measured raw mean and rms profiles across the mixing layer; (c) and (d) Mean and rms normalized by local maximum concentrations; (e) and (f) Averaged mean and rms concentration experimental profiles from the 15 sets of measurements and from the LES.

each profile should be rescaled by the mean scalar flux that occurred when it was measured. Actually the use of the local maximum concentration is an equivalent rescaling. To demonstrate this, the areas under the profiles shown in Fig. 4.5 (c) that have been rescaled by their local maxima, were determined. They are indeed very close to the same constant value (approximately 4.87) with a standard deviation of only 0.06, thus, verifying the equivalence of the normalization.

Shown in Fig. 4.5 (e) and (f) are the mean and rms profiles averaged over the 15 sets of measurements. Also shown there are the mean and rms profiles obtained from the LES. The experimental and LES mean profiles compare very well. However, although the shapes of the experimental and LES rms profiles are similar to each other and to those in [54], their magnitudes are quite different. This is likely due to two factors:

- First, the fact that the experimental profiles does not go to zero at the edges of the mixing layer reflects the low grey level noise of the camera (see Appendix B).

- Second, the light intensity of the smoke in the experiment, and from it the scalar concentration, is determined from a single pixel. This is a much greater spatial resolution than could be achieved by counting particles in an LES grid cell. In term of Kolmogorov length scale η, the experimental resolution is about 0.6η while the LES resolution is more than 30η near the mixing layer centerline where the grid is the finest. This lack of resolution in the simulations results in an attenuation in rms levels.

It is worth mentioning that the concentration rms profile is not symmetric. The peak intensity of the fluctuations occurs on the low-speed side of the mixing

layer. Also, in some of the experimental cases, slight inflection points can be observed in the middle of the curves, suggesting increased levels of concentration fluctuations away from the center plane of the mixing layer. This trend is more obvious in the LES results, where two peaks can be observed in some cases.

In order to support the conjecture that spatial resolution is responsible for the difference between the experimental and numerical concentration rms levels, the experimental data were spatially averaged over moving windows with widths of several pixels before averaging over the 1200 images (in time). In this way the spatial resolution was reduced by a factor of 8, in the cross-stream direction, to approximately match the spatial resolution of the hot-wire probe, which is about 5 Kolmogorov length. It was also reduced by a factor of 50 to match the spatial resolution of the smallest LES grid cell. As can be seen from Fig. 4.6, this spatial averaging dramatically reduces the C_{rms} levels. When averaging over 50 pixels, the rms levels were reduced by $30\% - 45\%$. It can also be seen that this reduction is not linear across the mixing layer. Thus the shape of the rms curves also changed, and became closer to the double-peak shape of the numerical results.

The LES concentration statistics can also be computed by determining the particle number density using a grid that is finer than the velocity mesh. Fig. 4.7 shows three cases where the particles at a given streamwise location ($x = 150$) are counted using different grids: one with the LES velocity grid, one with 1/2 streamwise grid spacing and one with 1/4 streamwise grid spacing. As can be seen, the concentration rms levels increase with the grid resolution. Furthermore the concentration rms profile loses its asymmetric shape for the finest resolution, probably due to the limited number of particles per cell. For the finest grid, on

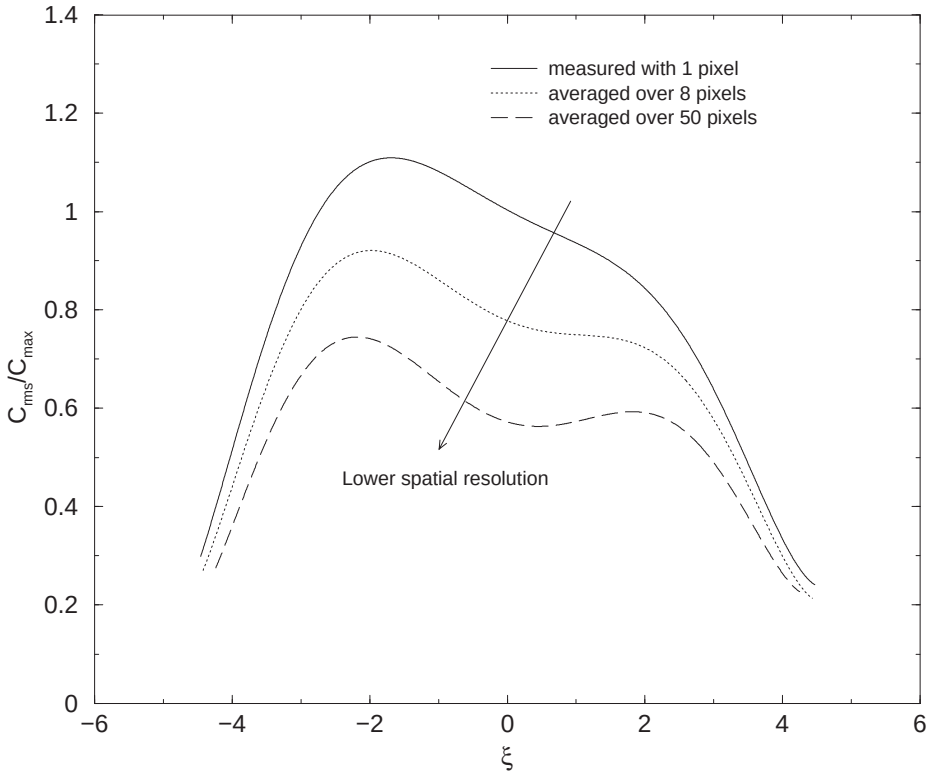

Figure 4.6: The dependence of the concentration rms levels on the spatial resolution of the experimental data.

average only 10 particles were located in each grid cell near $\xi = 0$. To provide spatial resolutions close to the experimental resolution, one must track much larger number of particles, which is practically not feasible.

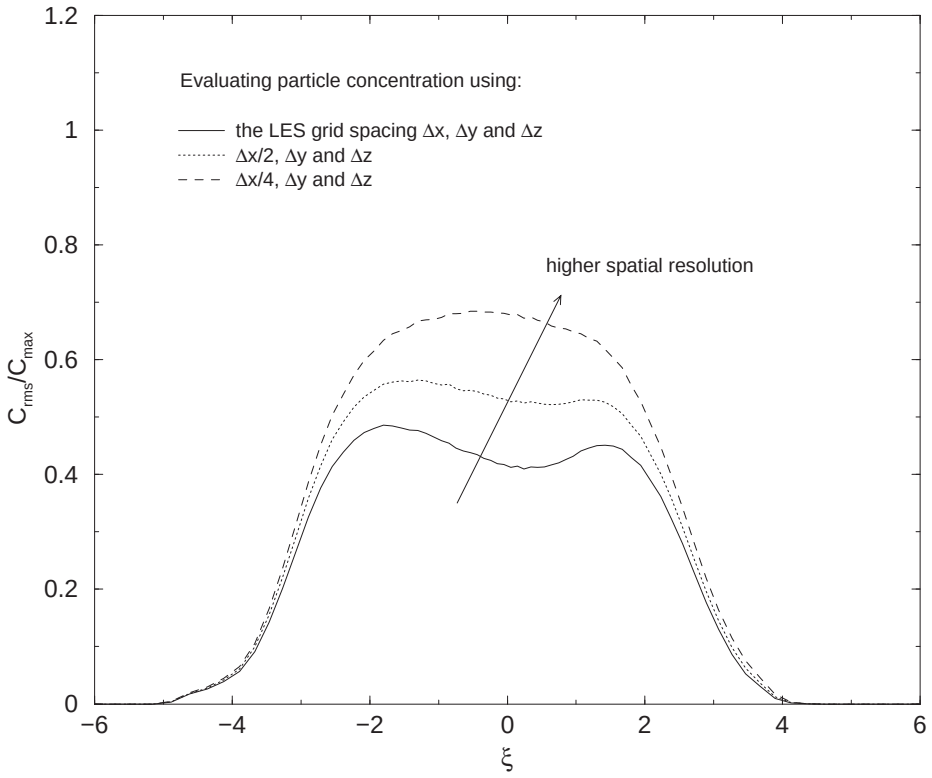

Figure 4.7: The dependence of the concentration rms levels on the spatial resolution in the simulations.

It is also worthwhile to point out that, as the numerical and experimental resolution for the computation of the concentration statistics approach each other, the shapes as well as the magnitudes of the rms profiles become similar.

4.4 Concentration Fluxes

To determine concentration fluxes, the velocity and concentration fluctuation information must be synchronized. As mentioned in chapter 2, the digital camera used in the current study has an output signal reporting its functional status. This signal was acquired simultaneously with the hot-wire anemometer output. Fig. 4.8 is a time series of raw data recorded by the data acquisition system

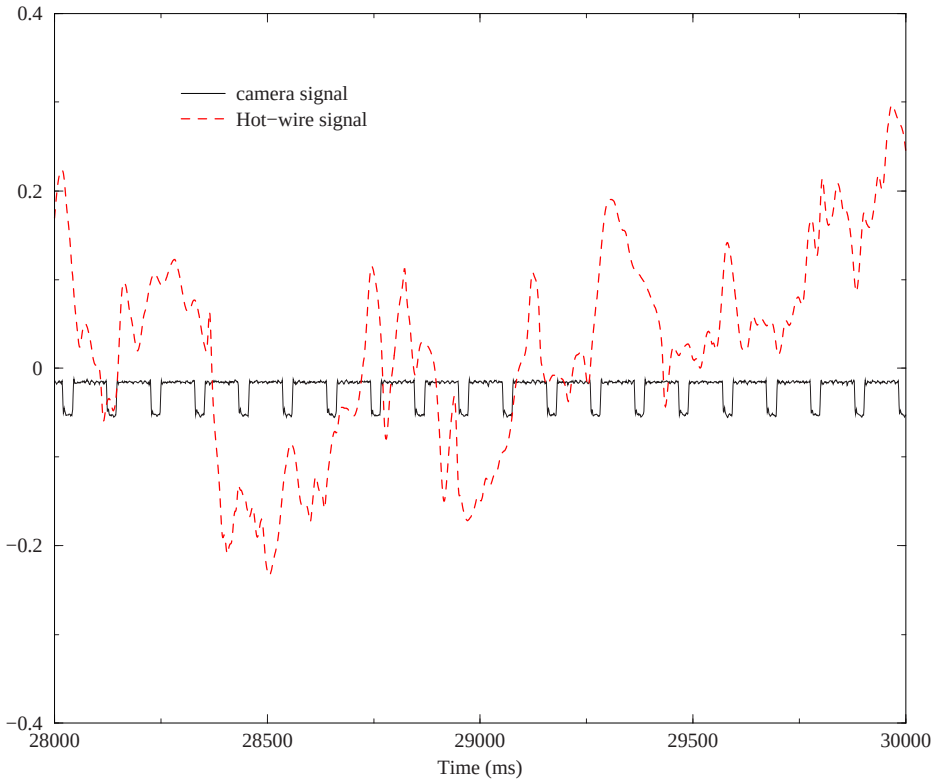

Figure 4.8: Synchronization of velocity and concentration information.

showing this synchronization. The dashed line is just a segment of turbulent hot-wire output voltage signal, while the solid line is the signal generated by the

digital camera. The pulses associated with each image capture are almost periodic and very easy to identify by a computer program. By extracting information from the camera signal, velocity data and concentration data could be properly aligned, and correlations between the velocity field and the concentration field, i.e. concentration fluxes, could be calculated. The correlations were calculated at times corresponding to the center points of the image pulses.

The sample size of the concentration measurements was considerably smaller than the sample size of the velocity measurements – only $1,200$ pairs of data values were available for concentration flux calculations. As a result, these statistics are not very smooth. The experimental concentration flux profiles of $\overline{uc}$ and $\overline{vc}$, along with the momentum flux (Reynolds shear stress) profile $\overline{uv}$, are plotted in Fig. 4.9.

Also plotted in Fig. 4.9 are the scalar and momentum flux values determined from the LES. In spite of the different type of errors in the determination from the experiment and from the LES of the C values used to obtain the scalar fluxes, the $\overline{uc}$ profiles agree rather well. The $\overline{vc}$ profiles agree much less well because of the small sample size of the C experimental measurements as explained in Appendix B. The shapes of the experimental and LES $\overline{vc}$ profiles are similar on the high-speed side of the layer, but their magnitudes are different. On the low-speed side the experimental data does not exhibit the anti-symmetry of the LES profile.

Though not very smooth, these curves do show some fundamental properties of scalar transport in this flow. Most important, mean gradient type of transport appears to be the major mechanism.

An illustration of the idea of mean gradient transport is shown in Fig. 4.10.

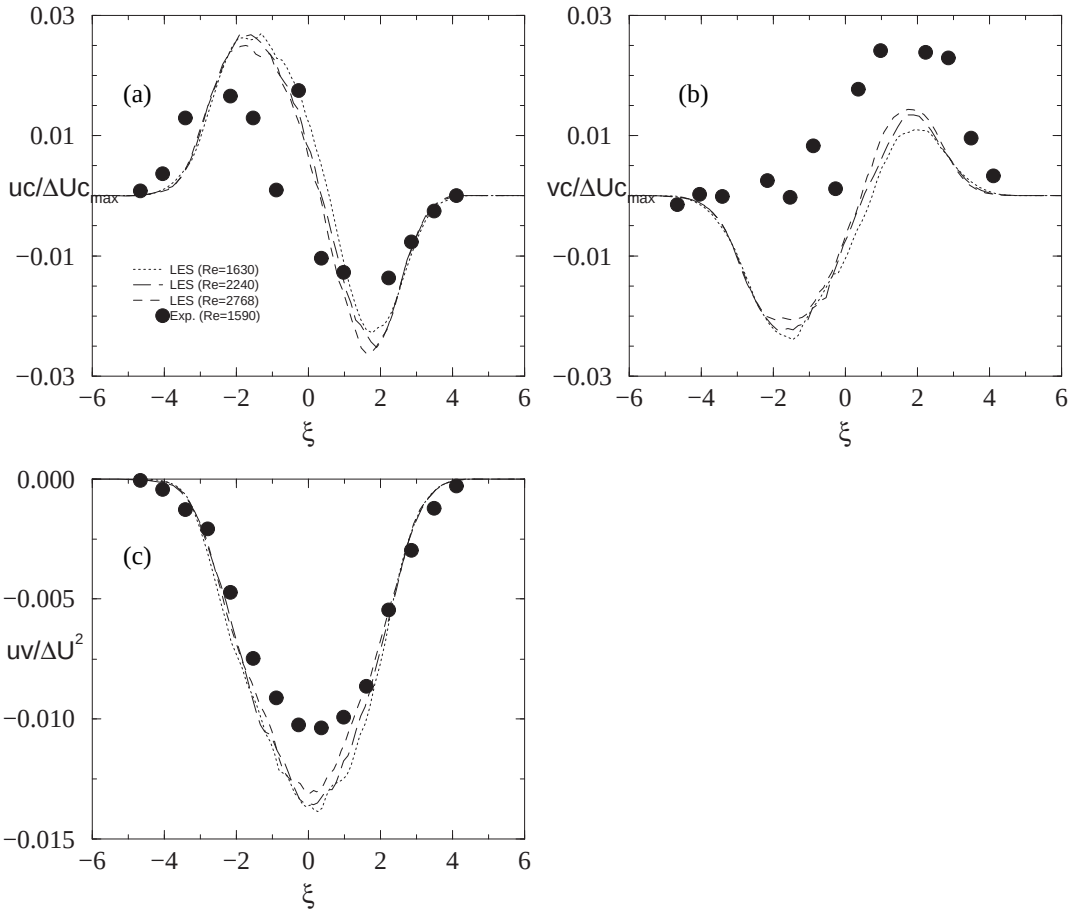

Figure 4.9: Concentration flux. (a) Streamwise flux $\overline{uc}$, and (b) Cross-stream flux $\overline{vc}$, normalized by $\Delta U c_{max}$. (c) Reynolds shear stress $\overline{uv}$, normalized by ΔU^2, for reference.

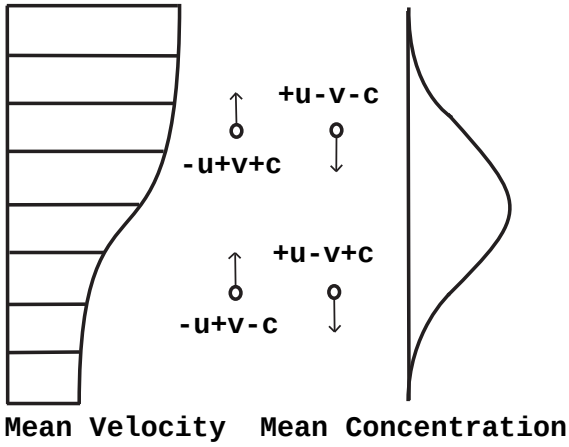

Figure 4.10: Combinations of $\pm u$, $\pm v$ and $\pm c$ that represent mean gradient transport.

Suppose that a fluid particle is moving in the cross-stream direction from the high-speed side toward the mixing layer centerline. Because the mean cross-stream velocity is nearly zero, the fluid particle must have a negative v velocity fluctuation. By looking at the mean streamwise velocity $\overline{U}$ and mean concentration $\overline{C}$ profiles, one can easily conclude that if the fluid particle moving toward the centerline carries its mean streamwise momentum and mean scalar concentration from its point of origin, it must experience a surplus of U and deficit of C when it arrives at a location with lower mean velocity and higher mean concentration near the centerline. Likewise a fluid particle moving from near the centerline toward the exterior of the high-speed side of the mixing layer will carry a deficit of U and a surplus of C when it arrives, from a mean gradient point of view. The combination of signs of these terms suggests that the $\overline{uc}$ flux is likely to have negative values on the high-speed side of the mixing layer, if the scalar transport is dominantly of the mean gradient type there. Similar analysis can be

performed for the low-speed side and on the $\overline{vc}$ flux as illustrated in Fig. 4.10.

The average momentum transport in the turbulent mixing layer is consistent with the mean gradient type, as is obvious from the Reynolds shear stress profiles in Fig. 4.9, where the values are negative across the layer. For scalar transport, Fig. 4.9 shows that the mean gradient transport is consistent with both the measured and LES scalar flux profiles, where the signs of the fluxes correctly follow Table 4.1 except for the $\overline{vc}$ flux experimental values on the low-speed side. This is shown to be due to the small data sample size as discussed in the Appendix B.

4.5 Octant Analysis

The basic idea of octant analysis is to sort the experimental data into categories (octants) by the combinations of signs of the velocity fluctuation u, v and concentration fluctuation c. This idea is an extension of the 'quadrant analysis' proposed by Wallace et al [77]. It has recently been successfully applied to a boundary layer flow to identify the major scalar transport mechanism [73] for that flow.

Table 4.1: Signs of flux terms based on mean gradient transport model for the mixing layer.

	$\overline{uv}$	$\overline{uc}$	$\overline{vc}$
high-speed side	-	-	+
low-speed side	-	+	-

Table 4.2: Definition of the eight octants based on the sign combinations of $\pm u$, $\pm v$ and $\pm c$.

I: +u, +v, +c	V: +u, -v, +c
II: -u, +v, +c	VI: -u, -v, +c
III: -u, +v, -c	VII: -u, -v, -c
IV: +u, +v, -c	VIII: +u, -v, -c

The octants are defined in Table 4.2. After the velocity and concentration data are properly aligned, one can easily sort the data based on the octants and calculate the following values for each octant:

- Frequency, which represents the fraction of the time the fluxes reside in each octant. The sum of these frequency fractions over all octants is 1.
- Fractional contribution, which represents the fractional contribution from each octant to the total fluxes. The sum of the fractional contributions over all octants is 1.
- Intensity, which represents the magnitude of the fluxes divided by their resident time in each octant.

Three positions were analyzed from the mixing layer data, one position on the high-speed-side, one position on the low-speed-side and one position from the center plane.

On the high-speed-side, octant II and octant VIII are of the mean gradient transport type. In the octant analysis results shown in Fig. 4.11, for both

scalar fluxes $< uc >$ and $< vc >$, octant VIII transport occurs most frequently (almost 30% of the time). However, the greatest contribution to the total flux is from octant II, which occurs relatively rarely but with very high intensity. The fractional contributions from the counter-gradient octants are all much smaller. This indicates that gradient transport of scalars is the dominate type for the high-speed side, although non-gradient transport can not be completely ignored.

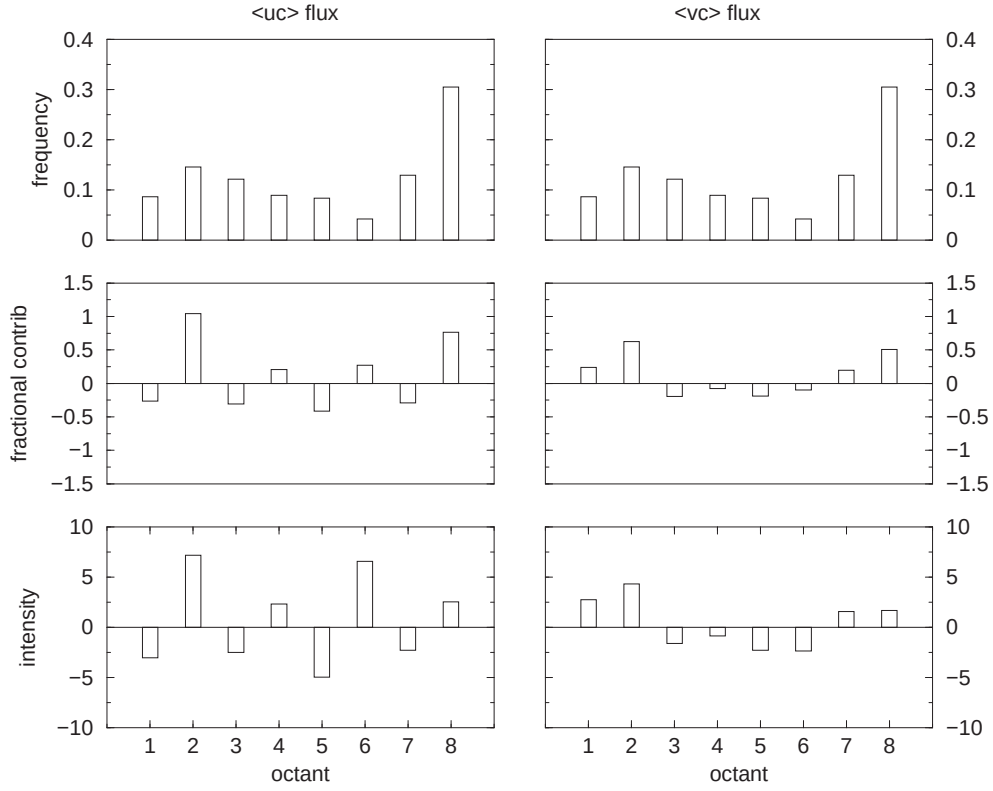

Figure 4.11: Octant analysis at $\xi = 2.1$ on the high-speed side of the mixing layer. Octant II and octant VIII are of the mean gradient type.

It is worth mentioning that the results above show the same trends as the octant analysis results [73] in the outer region of a turbulent boundary layer flow

over an obstacle with scalar released at the wall one obstacle height downstream. This is reasonable because the mean velocity and concentration profiles on the high-speed-side of the mixing layer are very similar to the mean velocity and concentration profiles in the outer flow zone in that flow.

On the low-speed-side, octant III and octant V are of the mean gradient transport type. From Fig. 4.12, it can be seen that Octant III occurs most frequently (25%), while octant V contributes the most to the total fluxes because of its high intensity. More so than the high-speed side, however, the contribution from other counter-gradient octants are very significant. For example, the fractional contributions of octants II and VIII are comparable to that of octant III. The flat shape of the $\overline{vc}$ flux curve on the low-speed side in Fig. 4.9 is a result of this apparent balance of the gradient and counter-gradient transport, although, as stated above, it is thought that this balance is a result of a too small sample size as discussed in detail in Appendix B.

At the center of the mixing layer, because the mean concentration profile reaches its maximum there, fluid particles from both sides are more likely to carry deficits of scalar concentration. Thus both octant III and octant VIII are sign combinations compatible with mean gradient transport. Fig. 4.13 shows that these two octants do occur most frequently. Octants II and V, however, also contribute a lot to the flux at this location. This may be because the peak concentration locations near the center line of the mixing layer were shifting somewhat with time (refer to Fig. 4.5 (a)).

In summary, the scalar transport octants that are compatible with mean gradient transport are the dominant contributors to the concentration fluxes across the mixing layer. Counter-gradient transport is also important throughout the

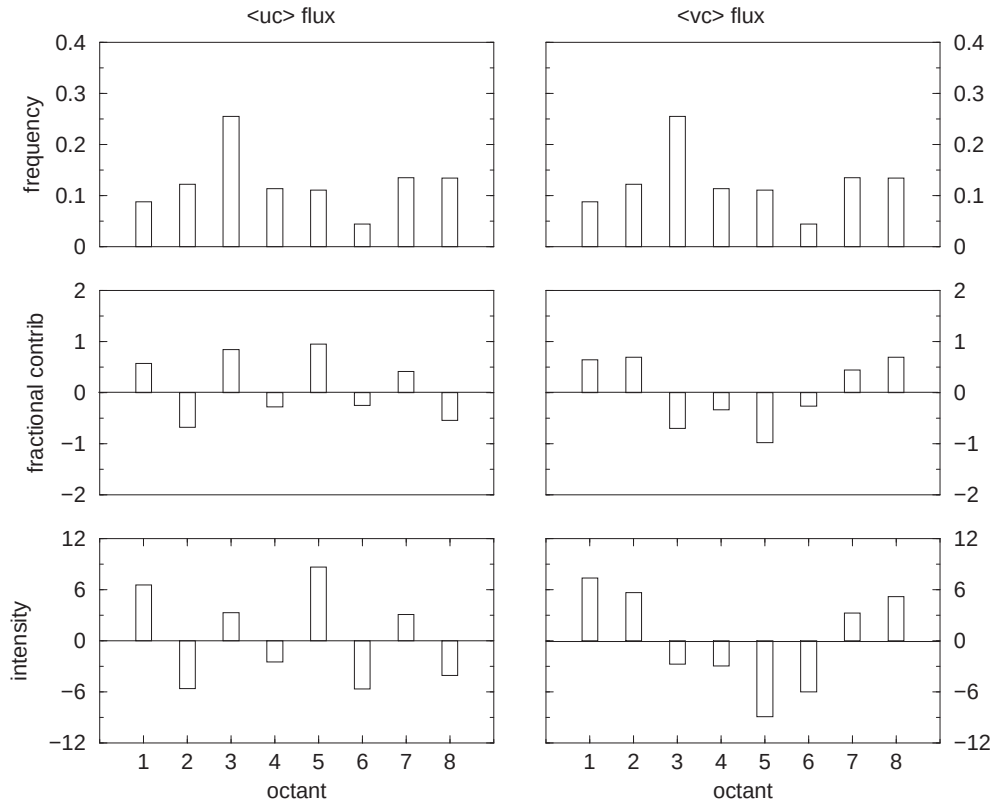

Figure 4.12: Octant analysis at $\xi = -2.2$ on the low-speed side of the mixing layer. Octant III and octant V are of the mean gradient type.

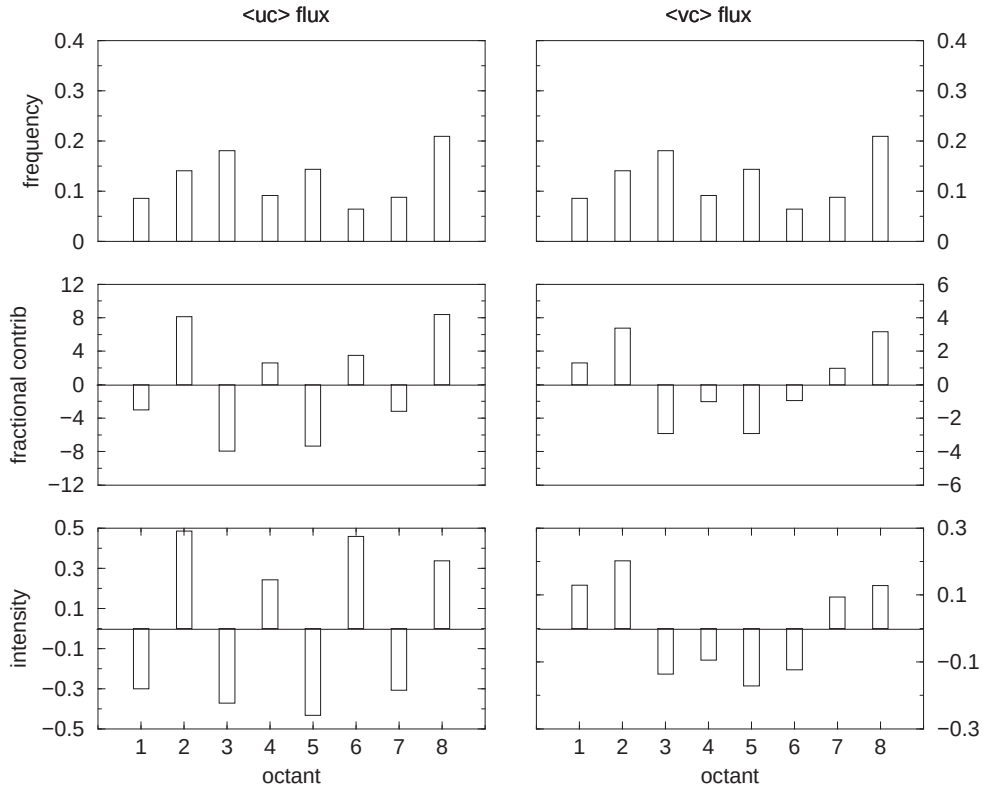

Figure 4.13: Octant analysis at the centerline of the mixing layer.

mixing-layer, especially on the low-speed side.

The difference in how mixing of scalar occurs between the high-speed and low-speed sides of the mixing layer has been referred as 'mixing imbalance' [55] and has other consequences, such as causing the asymmetric shape of the concentration rms profile.

4.6 Conditional Analysis

The purpose of the conditional analysis is to detect the coherent vortical structures in the mixing layer and to show how important transport properties are distributed spatially with respect to them.

It is well-known that coherent roller vortices exist in the turbulent mixing layer. During the present experiment, when the wind tunnel was running at a low speed and the smoke was illuminated by a two-dimensional light sheet, such coherent structures can be easily visualized. Fig. 1.1 on page 4 shows such a visualization taken in Loucks' experiment [45]. However, as the wind tunnel speed is increased, the flow becomes more turbulent and the smoke mixes more rapidly, making it more difficult to observe the coherent structures.

Furthermore, hot-wire experiments generally have the limitation that a limited amount of spatial information can be obtained. In the current experiment, only 15 locations along a vertical line across the mixing layer were traversed by the hot-wire probe. So to rebuild the spatial structure from the experimental data, conditional analysis had to be performed.

The passage of the rollers in a turbulent mixing layer is a quasi-periodic event. This fact can be used as a phase reference to perform the conditional analysis.

As suggested by earlier research [45], such events can be detected by placing a velocity measuring device (such as a single-sensor hot-wire probe) at the edge of the mixing layer and measuring the streamwise velocity, which provides a nearly periodic reference signal. This method is illustrated in Fig. 4.14, taken from Loucks [45].

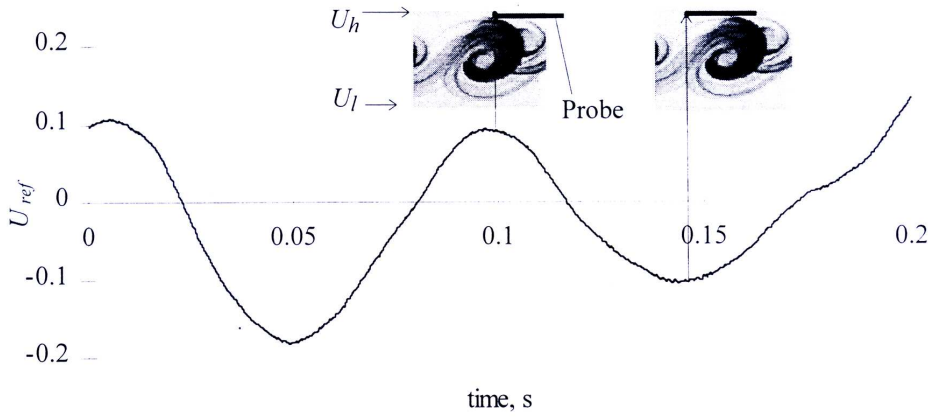

Figure 4.14: Passage of a roller with respect to a reference probe positioned at the outer edge of the mixing layer [45].

Note that the reference signal is not strictly periodic. The rollers do not just pass by the probe, one by one sequentially with a constant frequency. In a turbulent mixing-layer flow, their positions when intersecting the probe can vary because of their three-dimensional shapes. In addition, they undergo a process called 'pairing', which refers to the phenomenon that rollers upstream sometimes catch up to the rollers in front of them and form larger vortical structures. These variations make the roller-passing event quasi-periodic. However,

on average, rollers are convected downstream and the times between passages are corresponding to a relatively small frequency range.

In the current experiment, because of the additional complexity involved in measuring the concentration field, no effort was made to use an extra probe to provide a phase reference signal. However, it was possible to obtain a phase reference directly from the cross-stream velocity component of the mixing layer at each probe location.

From the mathematical point of view, if there is an inherent periodic frequency hidden in a signal, by performing an FFT and transforming the data into spectral space, the frequency can be detected. In the current experiment, the spectrum of the cross-stream velocity component displays such a small band of frequencies, at about $210Hz$, as seen in Fig. 4.15, indicating that a good phase reference can be extracted to perform the conditional analysis. This is the FFT of the cross-stream velocity signal at the high-speed free-stream. This frequency represents the roller-passage frequency in the mixing layer.

The procedure of Loucks [45] was used to identify the beginning and end of each event so that the data could be properly aligned to perform the conditional analysis. First, a sine wave signal was generated with its cyclic frequency chosen from the bump region of the v-component spectrum. The length of this test signal is taken to be the length of time in which three or four rollers pass by the measurement location. Then correlation coefficient between the test signal and the cross-stream velocity signal was calculated. The correlation coefficient was defined as:

$$R = \frac{\overline{u_{test} u_{ref}}}{\sqrt{\overline{u_{test}^2} \cdot \overline{u_{ref}^2}}}, \tag{4.9}$$

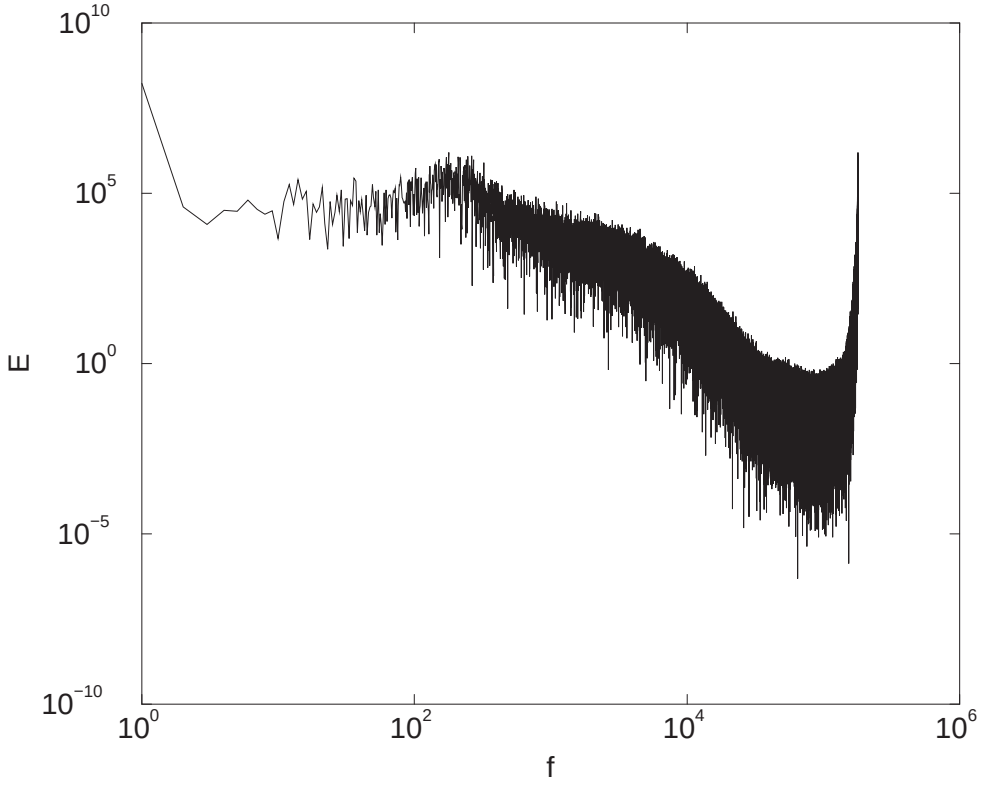

Figure 4.15: FFT of cross-stream velocity signal at $\xi = 4.2$ showing a bump that peaks at about $210Hz$ due to the roller passage event.

in which u_{ref} is the reference signal and u_{test} is the sine wave signal defined as:

$$u_{test} = sin(2\pi\omega t), \tag{4.10}$$

with ω the cyclic frequency. In Fig. 4.16 (a) is a sample of the raw cross-stream velocity signal. Note that this segment of signal is taken from the upper edge of the mixing layer at $\xi = 4.1$. Although the signal looks noisy and contains some turbulence, it does show some evidence of periodicity. The sine wave signal for event detection is also shown in Fig. 4.16(a). The correlation coefficient is calculated over a moving window, i.e., the test signal was shifted along the reference signal after each calculation, and is a function of time, as shown in Fig. 4.16(b).

The resulting correlation coefficient function is much smoother than the original velocity signal. The higher the correlation coefficient value, the greater the similarity between the segment of velocity signal and the test signal. It can be argued that each peak in the correlation corresponds to the time when the center of a roller core reaches the hot-wire probe. These peaks can be used as a phase reference to align the data for conditional averaging.

Before the conditional averaging, two additional steps were performed to make the procedure more effective. First, the frequency of the test sine wave signal was adjusted in order to maximize the correlation coefficient peak values. This allowed the value that best corresponds to the average roller-passing frequency to be found. Second, a threshold was used to filter the data associated with smaller peaks in the correlation coefficient function. This ensured that only those strong events were included in the conditional averaging.

After these steps, physical variables of interest were calculated and then

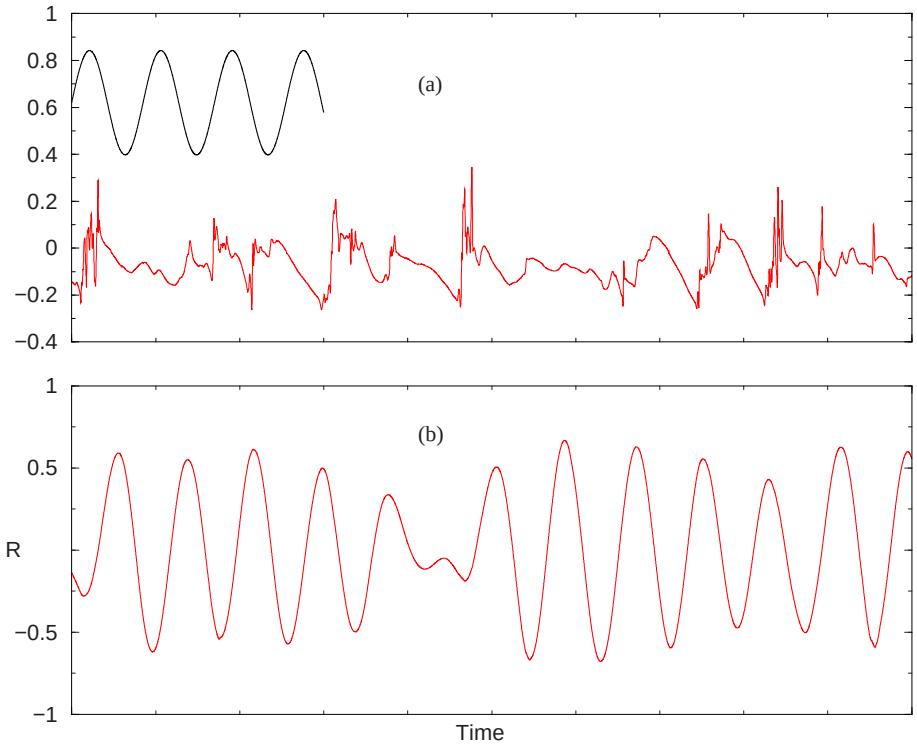

Figure 4.16: Detection of roller passage. (a) A sample of the cross-stream velocity signal at $\xi = 4.1$ and the test sine wave signals. (b) The correlation coefficient function between the velocity and test signals.

aligned based on the peak positions in the correlation coefficient function. Conditional averaging was then performed using the formula:

$$< a >= \frac{1}{N} \sum_{n=1}^{N} a(t_n + mdt), m = 1...M \tag{4.11}$$

where many segments of variable $a(t)$ of duration dt were collected and phase-aligned about t_n (where we have peak values in the correlation coefficient function), and averaged over N occurrences.

Note that mdt is chosen so that there were more than three rollers passing the probe during that interval. Thus an average two-dimensional flow field with several large structures in it was reassembled.

To provide a background field showing the existence of rollers, the streamwise velocity (u) and cross-stream velocity (v) components were first conditionally averaged in the manner described above and then assembled into a two-dimensional vector plot. To make the rollers more distinct, a roller convection velocity, U_c, defined in section 2.10 as the average of the high and low speed external stream velocities, was subtracted from every streamwise velocity value. This provides a viewpoint as if one were sitting on a fluid particle that travels at approximately the centerline speed of the mixing layer. Thus the high-speed-side fluid appears to be moving in the streamwise direction while the low-speed-side fluid appears to be moving in the upstream direction. Fig. 4.17(a) shows the velocity vector plot that is the outcome of this conditional analysis, where the large scale roller vortices are clearly evident. Based on the conditional velocity field, streamlines can be drawn, which illustrate the vortical structures even more clearly, as shown in Fig. 4.17(b).

Superimposed on this streamline plot, conditional averages of other variables

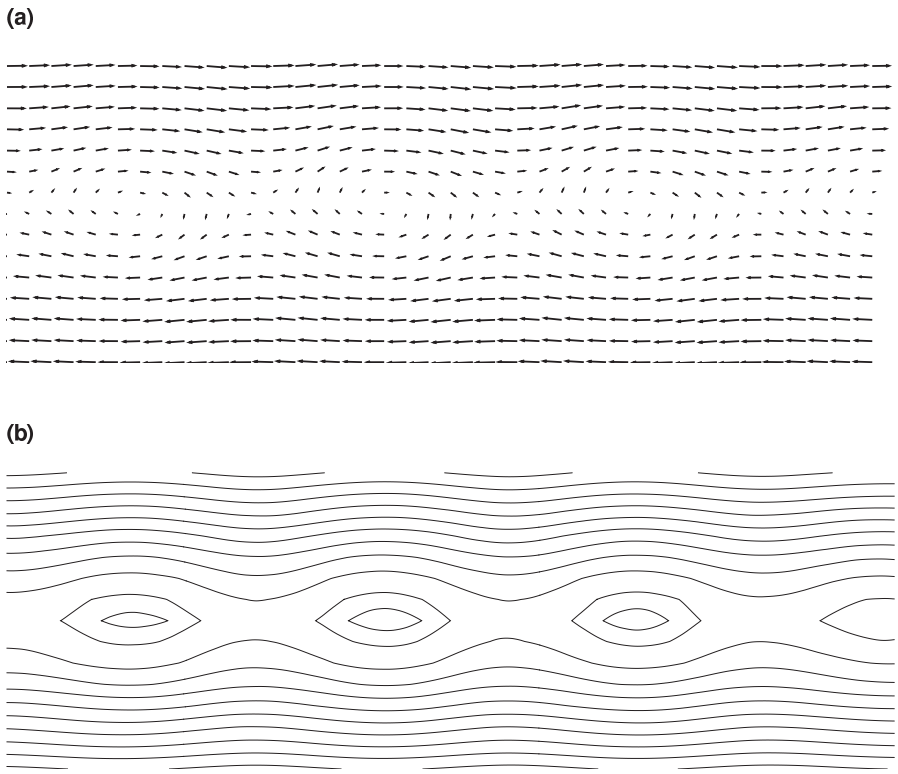

Figure 4.17: Large-scale roller vortex structures of the mixing layer flow (in an $x-y$ plane) revealed by the conditional analysis. (a) Vector map; (b) Streamline pattern. Flow is from left to right. A convective velocity has been subtracted from the streamwise velocity component to make the rollers distinct.

calculated in the manner of (4.11) can be plotted as color contours. This makes it easy to examine the spatial patterns of physical variables with respect to the position of the rollers.

For example, shown in Fig. 4.18 is the conditionally averaged Reynolds shear stress $< uv >$, which is an important part of turbulent kinetic energy production. From this figure, it is very clear that the phase-averaged correlation between u and v is always negative and the peak values occur in the regions where the braid[1] and roller meet. This agrees well with Loucks' experiment [45].

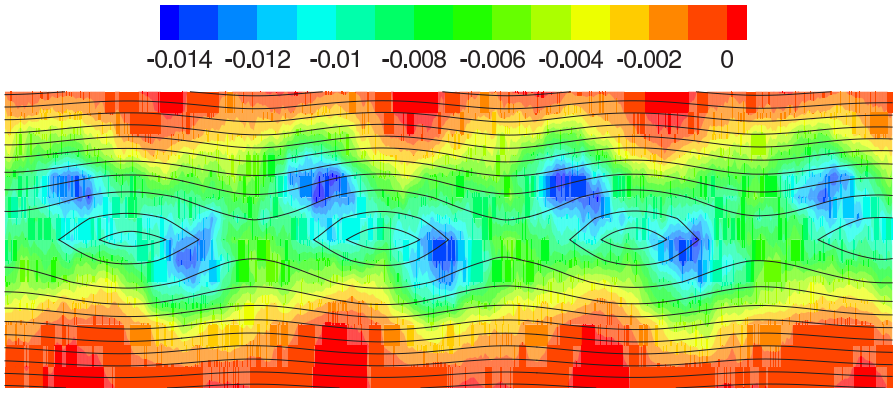

Figure 4.18: Conditional average of Reynolds shear stress ($< uv > /\Delta U^2$) showing its spatial distribution in relation to the positions of the roller vortices.

The same technique was applied to the concentration field, which yielded one of the major discoveries in the present study and gave new understanding about the scalar transport. Spatial patterns with respect to the positions of rollers were

[1]The braid refers to the region connecting the rollers. See Fig. 1.1 for a visualization.

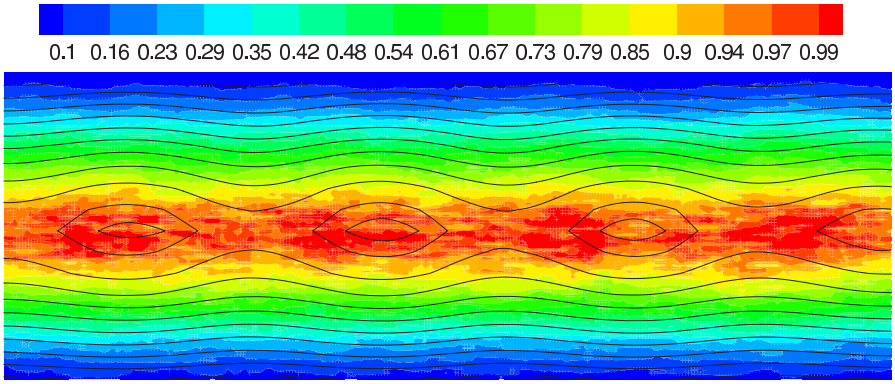

Figure 4.19: Conditional average of mean concentration, $< C > /C_{max}$.

detected in the mean concentration and concentration flux fields.

Fig. 4.19 shows the conditionally averaged mean concentration field. The scalar concentration is not uniformly distributed. The most concentrated regions in this mixing layer flow are at the downstream edges of rollers. While in the centers of rollers, the concentration is somewhat lower.

More interesting patterns appear in the concentration flux fields. Fig. 4.20 and Fig. 4.21 show the conditionally averaged concentration flux components, $< uc >$ and $< vc >$. It is evident that positive and negative values of concentration flux dominate in different regions. For the $< uc >$ distribution, the positive regions are more or less aligned with the cores of the rollers, with the highly positive regions (in red and yellow) below the rollers on the low-speed side. The negative fluxes occur mostly between the rollers and the highly negative regions are mainly on the high-speed-side. The $< vc >$ distribution is roughly opposite to $< uc >$. This is consistent with the negative correlation between the u and

v fluctuations as seen in Fig. 4.9 where the Reynolds shear stress distribution is shown. It is also consistent with the time averaged scalar flux peaks in that figure except for the $\overline{vc}$ flux on the low-speed side. The reason for this anomaly has already been discussed.

These conditional average results appear to be consistent with the time-averaged results in Fig. 4.5 (f). The positive peak $< uc >$ values and the negative peak $< vc >$ values all happen on the low-speed side, where the peak rms value of the concentration appears.

What remains to be done is to attempt to understand these concentration flux spatial distribution patterns. To do this the instantaneous LES flow fields must be examined.

Although the LES did not lend itself to a conditional analysis of this type, planes of data can be averaged across the span of an instantaneous three-dimensional realization of the flow to obtain somewhat similar results. Fig. 4.22 shows the spanwise averaged velocity vector field obtained in this manner. Superimposed on it are streamlines of the spanwise averaged flow field, and they reveal the presence of the roller vortices. The spatial distributions with respect to these vortices of the spanwise averaged $< uc >$ and $< vc >$ fluxes are seen in Fig. 4.23 and 4.24. Although these figures are not exactly comparable to the conditional averaged fluxes in Fig. 4.20 and Fig. 4.21, the spatial patterns are qualitatively similar.

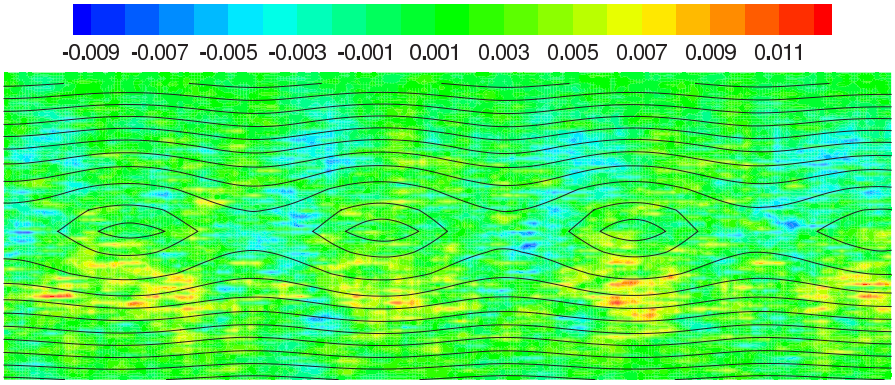

Figure 4.20: Conditional average of concentration flux $< uc > /\Delta UC_{max}$.

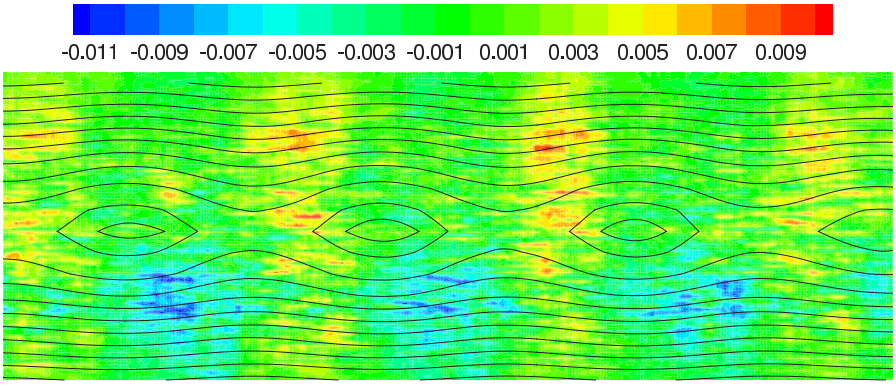

Figure 4.21: Conditional average of concentration flux $< vc > /\Delta UC_{max}$.

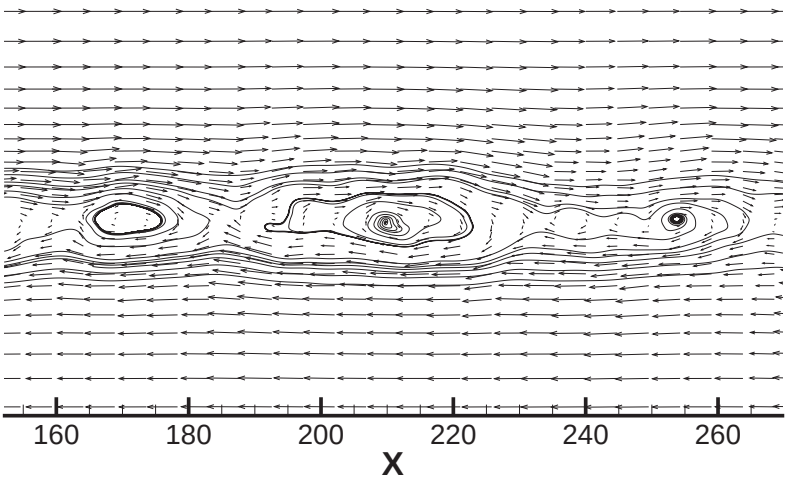

Figure 4.22: Spanwise-averaged instantaneous velocity vectors from the LES showing a few rollers.

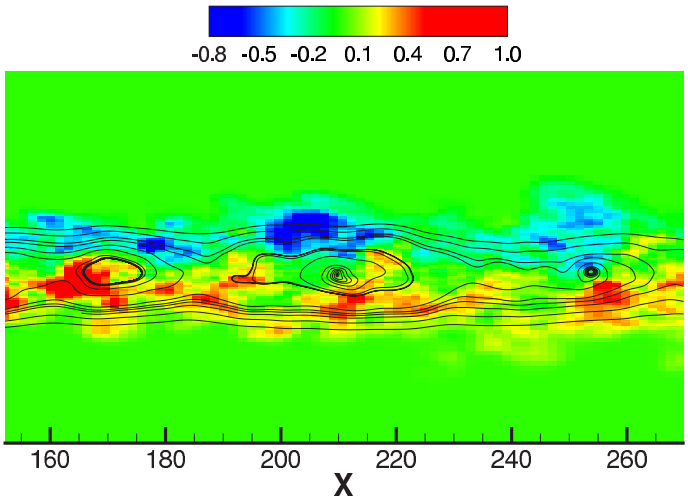

Figure 4.23: Spanwise-averaged instantaneous concentration flux $\overline{uc}/\Delta UC_{max}$ with respect to the rollers.

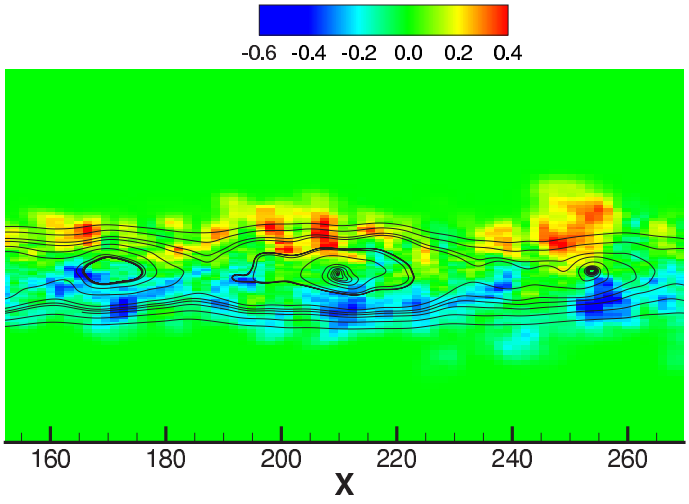

Figure 4.24: Spanwise-averaged instantaneous concentration flux $\overline{vc}/\Delta UC_{max}$ with respect to the rollers.

4.7 Scalar Transport Mechanisms

Today, it is established that mixing layers are dominated by large coherent structures. The LES conducted in the present study provide a good opportunity to study the dynamics of these structures and their effect on the scalar transport mechanisms. For this reason a series of instantaneous flow realization were examined. Initially the large spanwise rollers and the rib vortices in the braid regions were identified. Then, using the conditional averages extracted in the experiments as guidance, possible mechanisms describing how the dynamics of the rollers and rib vortices affect the scalar transport could be proposed.

Several criteria can be used to identify the coherent structures in turbulent flows. First, it was reported [60] that low pressure regions are often associated with vortex cores. This is especially effective to identify the large-scale spanwise rollers in the mixing layer flow, because these rollers are often spatially well organized with clear and strong core regions.

Fig. 4.25 is a typical plot showing iso-surfaces of low pressure regions of the mixing layer flow. It is a snapshot of flow field close to the splitter plate, where a few distinct big spanwise rollers can be observed. Due to the realistic inflow conditions and highly turbulent nature of the flow, the eddies are significantly twisted and deformed, with a lot of three-dimensionality in addition to the quasi-two-dimensional structure. The rollers downstream appear to experiencing the pairing process as they seem to interact with each other and form a larger structure.

Another useful identification criterion is the second invariant of the velocity

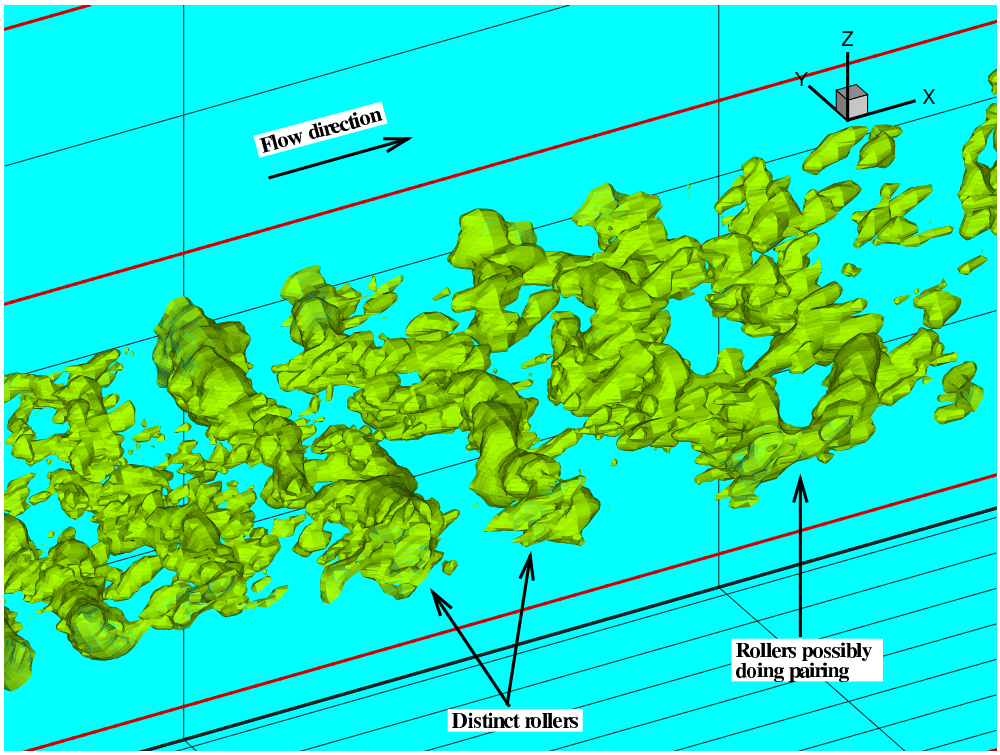

Figure 4.25: Iso-surfaces of low pressure regions highlighting the large-scale rollers in the mixing layer.

gradient tensor, defined as:

$$Q = -\frac{1}{2}\frac{\partial u_i}{\partial x_j}\frac{\partial u_j}{\partial x_i}. \tag{4.12}$$

Using the notation of the strain rate tensor S_{ij} and the rotation tensor Ω_{ij}, the mathematically equivalent form of (4.12) is:

$$Q = \frac{1}{2}(\Omega_{ij}\Omega_{ij} - S_{ij}S_{ij}), \tag{4.13}$$

which has a more obvious physical meaning. It is clear that positive Q represents regions where vorticity is due to rotation rather than to shear. It was reported [7] that the $Q > 0$ criterion is very effective in highlighting the streamwise rib vortices mainly occurring in the braid regions of the mixing layer.

Fig. 4.26 shows the iso-surfaces of $Q = 0.05$ on top of the roller structures identified by low pressure and shown in Fig. 4.25. Again, due to the highly turbulent and three-dimensional nature of the flow, these structures are complex in shape. However, many of them do have streamwise orientations, lying between the big rollers. They can be identified as rib vortices.

In this flow, one can also identify the rib vortices by looking at the distribution of streamwise vorticity, as shown in Fig. 4.27. In this case, iso-surfaces of two vorticity levels have to be plotted, one positive and one negative. These structures are also mostly aligning in streamwise direction. Different signs of this variable suggests that the rib vortices rotate in opposite directions, sometimes lying side by side.

After the detection of the vortical structures of the flow, the scalar transport mechanisms can be studied by observing planes in the instantaneous flow at locations of interest.

Fig. 4.28 is an idealized model to describe how rib vortices transport the

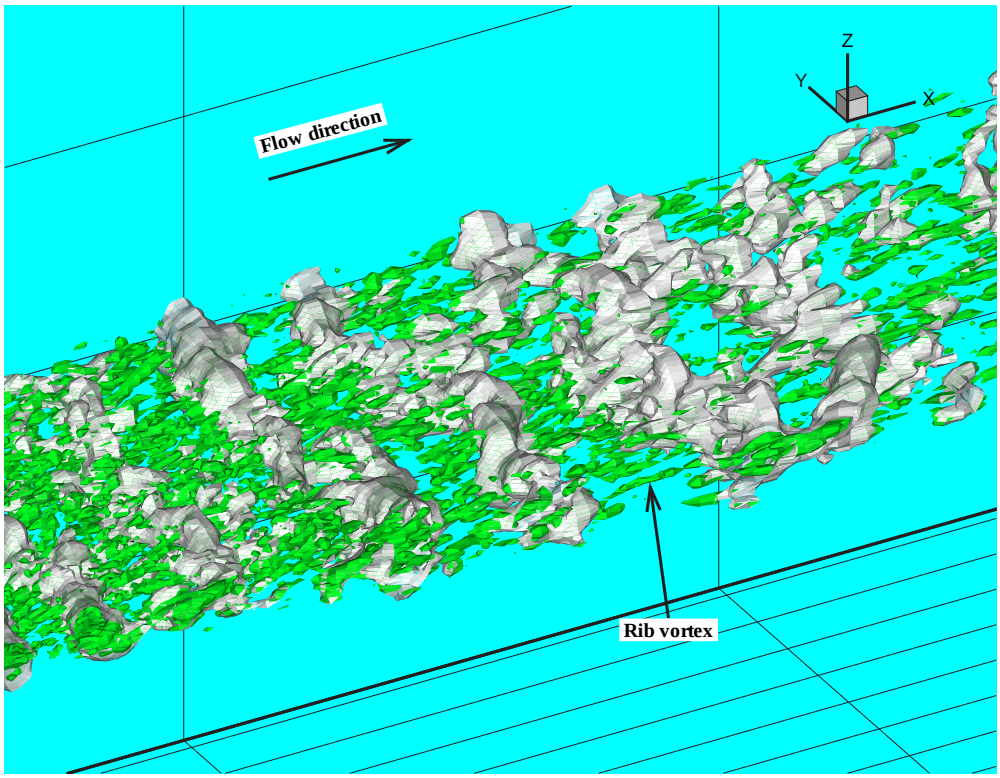

Figure 4.26: Iso-surfaces of positive Q highlighting the rib vortices in the mixing layer. The underlying white shade is the same low pressure isosurfaces as in Fig. 4.25.

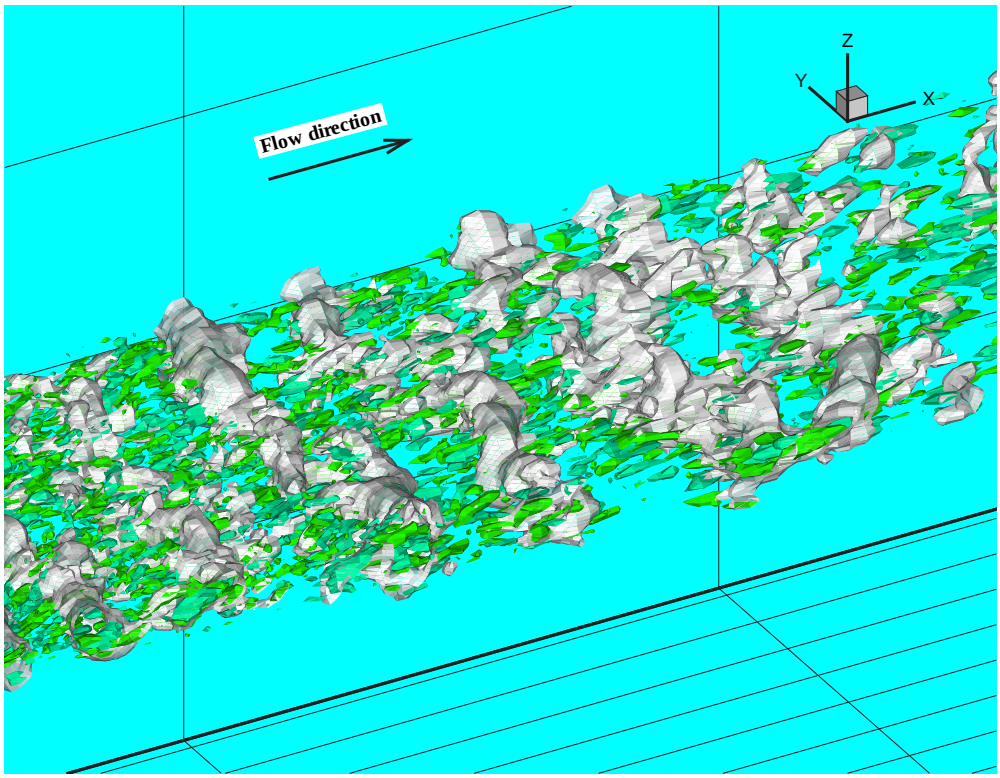

Figure 4.27: Iso-surfaces of streamwise vorticity highlighting the rib vortices in the mixing layer. Iso-surfaces of two vorticity levels are plotted, one positive (light green) and one negative (dark green).

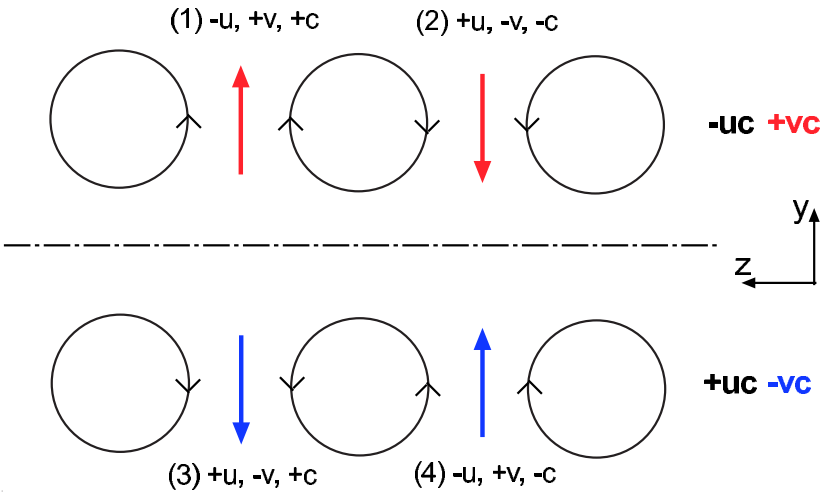

Figure 4.28: A model illustrating the scalar transport mechanism by idealized rid vortices. (1) through (4) are the possible mean gradient transport events, illustrating movement of particles away from or toward the center plane transporting an excess or deficit of scalar, respectively, with respect to their arrival locations.

scalar. In the braid region of the mixing layer, rib vortices are often found to be oriented more or less side by side in counter-rotating pairs. Using the idea of mean gradient transport, one can summarize all the possible events describing transport by particles carrying an excess or deficit of scalar away from or toward the mixing layer center in a $y-z$ plane: On the high-speed side, events 1 (-u,+v,+c) and 2 (+u,-v,-c) are of the mean gradient type, having $-uc$ and $+vc$ combinations. On the low-speed side, events 3 (+u,-v,+c) and 4 (-u,+v,-c) are of the mean gradient type, having $+uc$ and $-vc$ combinations. As will be seen shortly, all these event types can be found from the instantaneous visualization of the flow. Their effects on the spatial distribution of the uc and vc fluxes as well as the uv momentum flux can also be seen in the patterns of Fig. 4.18 through Fig. 4.21.

Fig. 4.29 shows an instantaneous $y-z$ plane from the simulation in the braid region at $x = 255$. The underlying vector plot clearly shows the existence of many rib vortices. The color contour of the top figure shows the concentration fluctuation c. The color contour of the bottom figure shows the vc flux[2]. A few obvious patterns are seen in this visualization:

- Most of the scalar is found in the neighborhood of rib vortices. The blue regions in the top figure, which are almost free of rib vortices, are mostly associated with very low scalar concentrations.

- The concentration levels just in the cores of the rib vortices appear to be

[2]The $y-z$ plane does not contain any information about the streamwise velocity U, so only the vc flux can be directly observed here. However, because u and v are negatively correlated, the trend of uc can also be inferred.

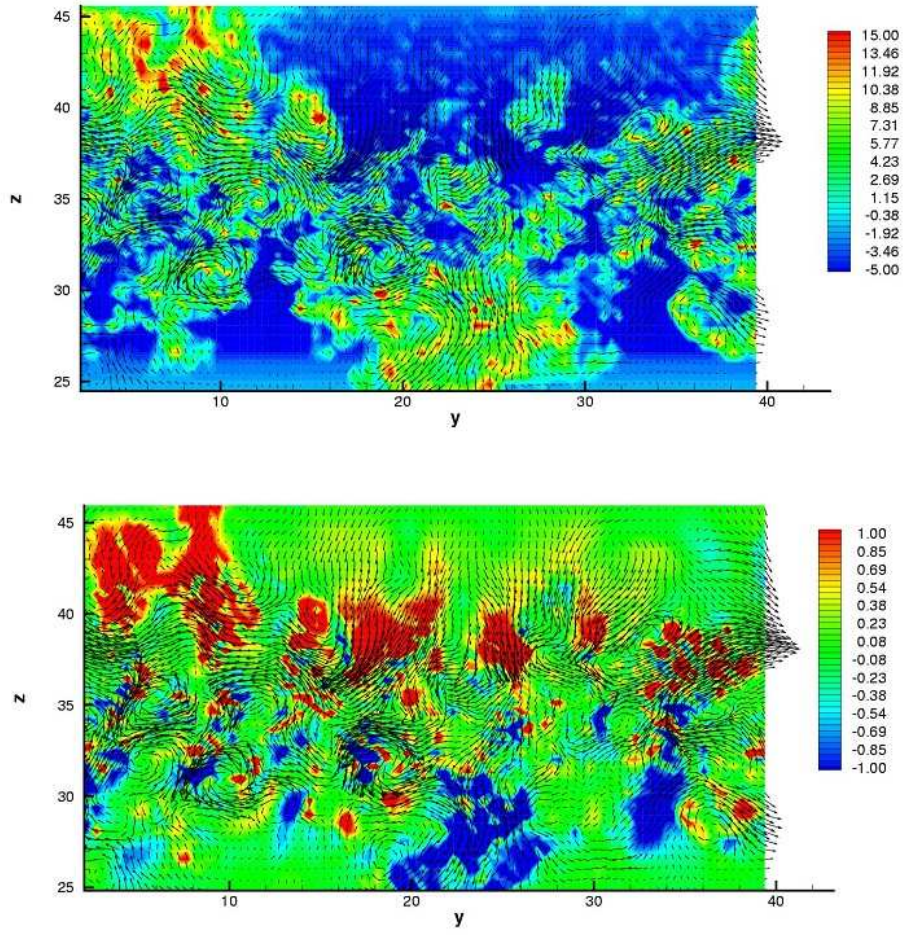

Figure 4.29: Instantaneous visualization of concentration fluctuation c (top) and vc flux (bottom) on a $y-z$ plane at $x = 255$. This plane is in the braid region where the streamwise rib vortices are strong.

smaller than in the surrounding areas.

- Most of the regions of positive vc flux are on the high-speed side and of negative vc flux on the low-speed side, consistent with the averaged results seen previously in Fig. 4.9, 4.21 and 4.24.

- Whenever two rib vortices reside side by side at about the same cross-stream level, the scalar flux vc between the vortices tends to be of one of the event types in the model shown in Fig. 4.28. One clear example is at the lower-left corner of the bottom plot at around $z = 30$. The rotation direction of this pair of rib vortices matches event 3 in Fig. 4.28, and the concentration flux between them indeed shows the expected sign given by the model.

Similarly, an idealized model for the spanwise roller vortices in a convective frame of reference is given in Fig. 4.30. Again 4 possible mean gradient scalar transport events can be identified at the corners of the roller vortices. The combination of signs suggests that the vc flux are likely to be positive on the high-speed side, and negative on the low-speed side and vice versa for the uc flux. This has already been confirmed and shown in Figs. 4.23 and 4.24 based on spanwise-average data.

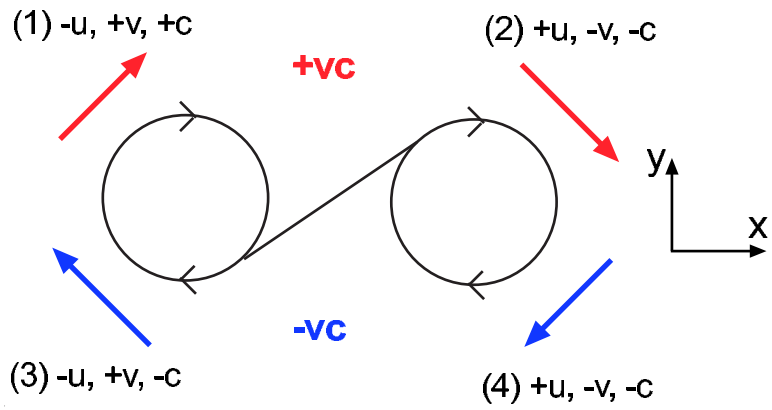

Figure 4.30: A model illustrating the scalar transport mechanism by idealized roller vortices in a convective frame of reference. (1) through (4) are the possible mean gradient transport events, illustrating movement of particles away from or toward the center plane transporting an excess or deficit of scalar, respectively, with respect to their arrival locations.

Chapter 5

Conclusions

Experimental and numerical studies of plane turbulent mixing layers with passive scalar were conducted. This chapter is a summary of the key aspects of these studies and the conclusions made from them.

- The experimental was performed in the low-speed wind tunnel of the Turbulent Research Laboratory at University of Maryland. A curved splitter plate built in the tunnel created a mixing layer with an approximately 2:1 velocity ratio.

- Smoke generated by burning incense was used as a passive scalar and was released into the high-speed side boundary layer of the splitter plate. Scalar concentration measurements were made by taking digital photographs of the smoke illuminated by a laser light sheet.

- Velocity and vorticity measurements of the flow field were performed using a 12-sensor hot-wire probe. The probe traversed 15 cross-stream locations during the experiment.

- The synchronization of flow field and scalar field information was achieved by sampling the hot-wire data and the digital images simultaneously. The digital camera provided a reference signal, which was recorded to provide phase information of the two data sets.

- The 12-sensor hot-wire was calibrated by exposing it to pre-determined flow conditions and recording its response. The calibration coefficients were then determined by solving a least-square system. The calibration was proved to be highly accurate after proper temperature correction. This provided good confidence in the measurements of the flow field.

- Two different data reduction methods were attempted to post-process the hot-wire data. The one developed by Vukoslavčević et al [76] performed better and was chosen to process the hot-wire data.

- From preliminary single-sensor hot-wire measurements, velocity profiles at a few streamwise locations (beginning at the splitter plate trailing edge) were obtained. The growth of the mixing layer was evaluated and the location of the beginnings of the self-similar state of the flow was identified.

- Large-eddy simulation of the mixing layer was performed. The concentration field was studied in the simulation by tracking massless fluid particles.

- The LES was performed by a finite difference code, based on the fractional step method, using 2nd order time advancement and 2nd order spatial discretization on a staggered grid. The Lagrangian-averaged dynamic eddy-viscosity subgrid scale model proved to be very effective for this flow.

- The boundary conditions for the LES were carefully implemented. Specially, the inflow condition was based on auxiliary simulations accelerated by a recycling technique. This new approach proved to be highly efficient. The introduced periodicity at the inflow plane was lost in a short streamwise distance after the inflow plane, and the downstream statistics were not affected.

- Three interpolation schemes were implemented to perform the particle tracking. Care was taken to evaluated each scheme's accuracy and efficiency. The tri-linear scheme, which has the best overall performance, was chosen to conduct the final simulation.

- The simulation appeared to be very sensitive to the inflow conditions. The inflow based on auxiliary simulations was carefully adjusted to match the experimental condition at the trailing edge of the splitter plate.

- The self-similar state of the flow was clearly identified from the integral properties of the flow: the growth of momentum thickness and the dissipation rate.

- Experimental and LES velocity statistics are in good agreement with each other and with other references. The vorticity statistics also agree reasonably well, despite the fact that Taylor's hypothesis introduced uncertainties in determining the experimental streamwise velocity gradients, and the small-scale eddies in the LES are only modelled.

- The experimental and LES mean concentration profiles compare well. The concentration rms curves have similar asymmetric shapes that peak on the

low-speed side. However the magnitude of the experimental concentration rms is higher than the LES rms because of the much greater spatial resolution of the experiment compared to the LES. The difference, however, was greatly reduced by filtering the experimental data and using finer grid to evaluate the particle concentration. The camera appeared to have a background grey level that also affected the concentrations.

- The LES concentration fluxes are consistent with the mean gradient transport model. The experimental fluxes also support this model, except that the vc flux on the low-speed side shows anomalous behavior. This has been determined to be likely due to the small sample size of the concentration measurements in the experiment (details provided in Appendix B).

- Octant analysis of the experimental data shows that the scalar transport octants that are compatible with mean gradient transport are the major contributors to the total flux. However the counter-gradient transport is also important, especially on the low-speed side.

- Conditional analysis of the experimental data was performed to reveal aspects of the flow structure. A phase reference for the roller vortex passings was found from the spectrum of the cross-stream velocity. Two-dimensional conditionally averaged pictures of the flow were reconstructed based on the phase information. These pictures exhibited clear patterns of both the momentum Reynolds shear stress and the scalar concentration fluxes. Similar patterns for the concentration fluxes were found from the spanwise averaged LES instantaneous data.

- The three-dimensional instantaneous flow fields from the LES were studied. Large-scale spanwise rollers and rib vortices were visualized by using proper criterion to filter the velocity field. Idealized mean gradient models of the momentum and scalar transport mechanisms by the roller vortices and rib vortices were proposed. Evidence supporting these models were found in the instantaneous LES field.

Appendix A

Implementation Details of Polynomial Interpolation

As mentioned in Chapter 3, the direction-by-direction 3D polynomial interpolation can be broken into a series 1D interpolations. The 1D interpolation subroutine *polint* was taken from Numerical Recipes, which is considered to be one of the fastest implementations of the Neville's algorithm. The signature of this subroutine is:

$$polint(xa, ya, n, x, y, dy), \tag{A.1}$$

where xa and ya are arrays of size n containing coordinates and function values of those tabulated points. Given an arbitrary x, this routine returns an interpolated value y, with error estimate dy. Minor changes were made to make the code more portable across different computer platforms.

Similarly, the 2D subroutine *polin*2 was also taken from the book, which perform seven 1D interpolations in a plane, with six in one direction and one in the other direction, as shown in Fig. A.1. The signature of this routine is:

$$polin2(x1a, x2a, ya, m, n, x1, x2, y, dy). \tag{A.2}$$

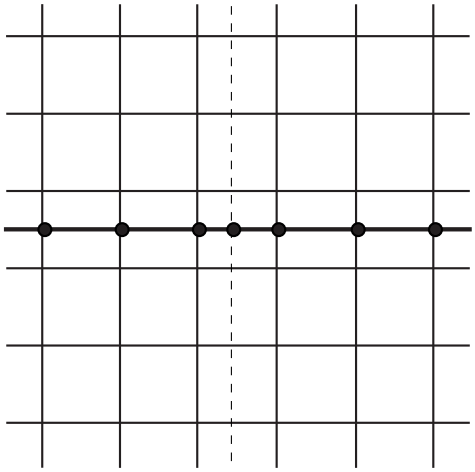

Figure A.1: Fifth order polynomial interpolation in a 2D plane.

The parameters have similar meanings as in the 1D case, except that two 1D arrays ($x1a$ and $x2a$) are used here to store coordinates and one 2D array (ya) is used to store function values of the tabulated points, so that

$$ya(j,k) = y(x1a(j), x2a(k)). \tag{A.3}$$

By emulating the way these routines are constructed, a 3D routine was developed, which contains 2D interpolations in six planes and one last 1D interpolation, as shown in Fig. A.2. The signature of the routine is similar:

$$polin3(x1a, x2a, x3a, ya, m1, m2, m3, x1, x2, x3, y, dy), \tag{A.4}$$

and the tabulated data points are stored to satisfy:

$$ya(i,j,k) = y(x1a(i), x2a(j), x3a(k)). \tag{A.5}$$

Note that the above implementations are quite general, in that the number of points involved does not have to be fixed. These numbers (n in the 1D case, m

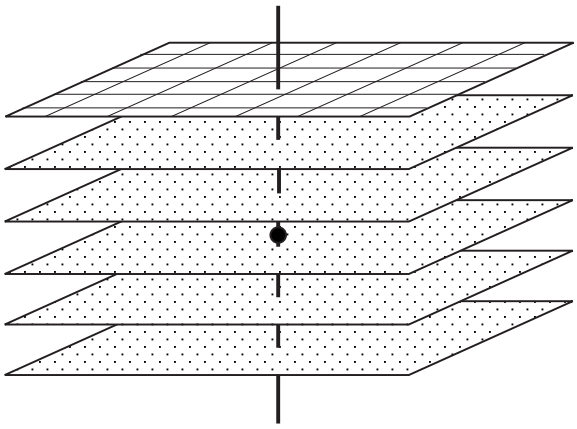

Figure A.2: Fifth order polynomial interpolation in a 3D domain.

and n in the 2D case, $m1$, $m2$ and $m3$ in the 3D case) can be chosen arbitrarily as needed. In practice, however, these numbers should not be too high, because higher order polynomials tend to have more oscillations between tabulated points and are not always more accurate.

Appendix B

Evaluation of the Experimental Errors

As mentioned in section 4.4 and seen in Fig. 4.9, the experimental concentration vc flux has an unexpected distribution on the low-speed side. There the values are almost zero in contrast to the LES result. Also, Fig. 4.5 shows that the concentration rms values do not go to zero at the free-stream on either side of the mixing layer. To investigate these anomalous behaviors, additional detailed analysis (mostly probability analysis) was performed on the experimental data sets. Two major problems were identified as the cause of the anomalies:

- The digital camera performing the concentration measurement has a limited sensitivity so that low concentrations below a floor threshold were truncated and assigned a small but non-zero grey level. Furthermore, this floor grey level varies somewhat with time, i.e. it has a certain random noise.

- The sample size of the concentration measurement was not large enough to give good converged values of the concentration fluxes. As a result, extreme values had great impacts on the total flux average values.

These issues will be discussed in detail.

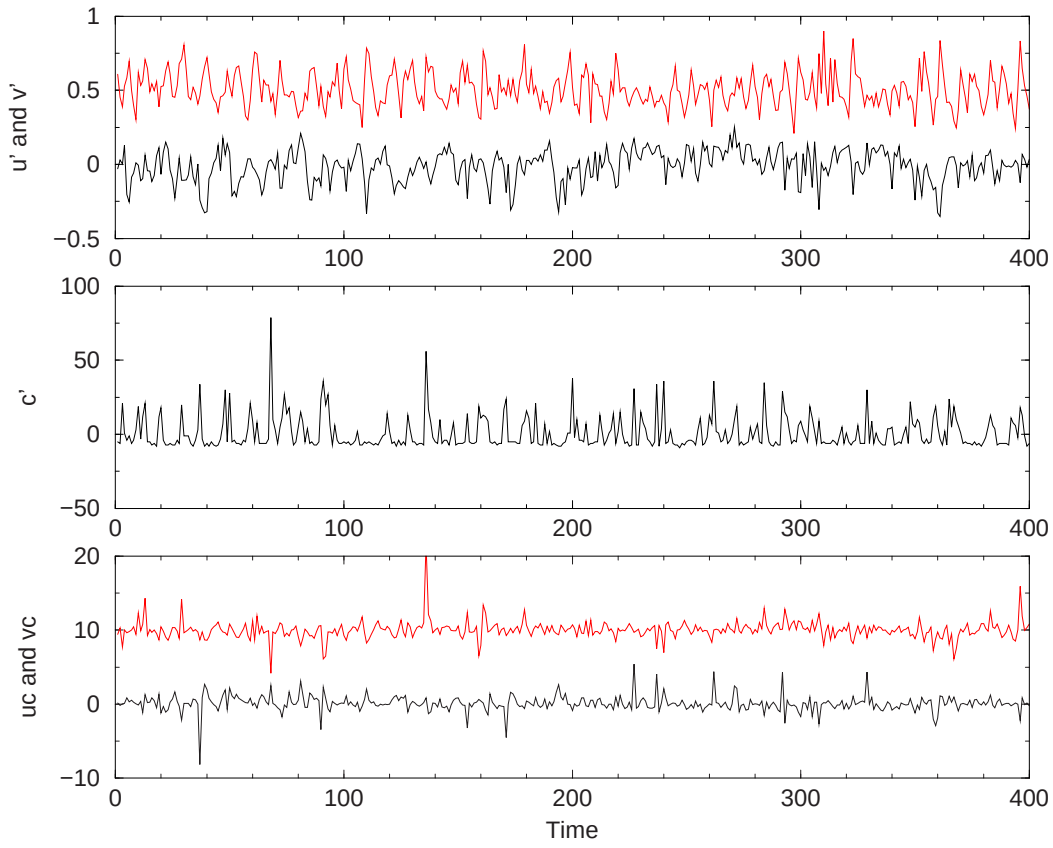

Figure B.1: Time series of velocity fluctuations, concentration fluctuations and concentration flux fluctuations at $\xi = 2.1$. v' and vc are shifted by 0.5 and 10 units, respectively, for clarity.

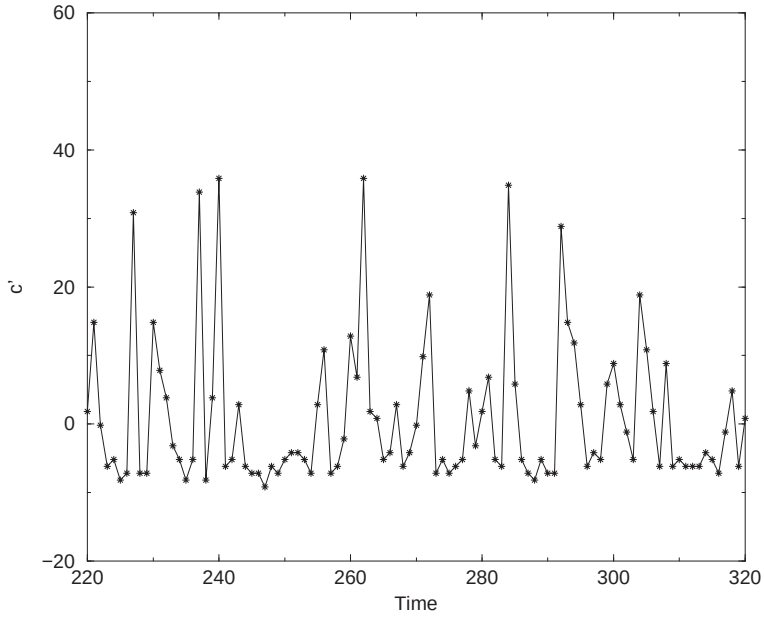

Figure B.2: A zoomed-in view of the concentration fluctuation time series clearly showing the variation of the concentration background itself.

First shown in Fig. B.1 are the time series of the u and v velocity fluctuations, the concentration fluctuations and the concentration flux fluctuations. They were taken from a high-speed side location at $\xi = 2.1$ in the mixing layer. The velocity signals appear to be normal turbulence. It is worth mentioning that the negatively correlated nature of the u and v fluctuations is quite apparent. For the concentration signal, one can clearly see a floor below which the lower concentrations, having negative fluctuations with respect to the mean, were truncated. That is to say, the light intensity below a threshold was recorded as the background light intensity. This background itself, as can be seen in the zoomed-in region shown in Fig. B.2, fluctuates somewhat with time. The non-zero concentration rms at the free-stream in Fig. 4.5, having a magnitude of about 0.2,

is the rms of this varying background. From the concentration flux signals in Fig. B.1, one can notice that some peaks of flux are very large, fluctuating about the mean more than 10 standard deviations. Only a few such extreme events were captured in each recording segment due to the limited sample size[1]. This inevitably affected the accuracy of the total flux.

The expected behavior of the concentration distribution can be seen by sampling the numerical simulation data. Fig. B.3 shows the scalar concentration probability density function of both the LES (left column) and the experiment (right column) at three comparable cross-stream locations. In (a) the solid line shows the cumulative sum of the histogram, indicating that it is indeed probability density. It can be seen that, at the centerline location of the mixing layer, the numerical pdf is almost symmetric, while the lower concentration pdf values of the experimental data are clustered in a few bins on the left side of the pdf where the low concentration is truncated. The truncation becomes more and more severe as one moves towards the edge of the mixing layer. At the edge of the mixing layer, the numerical pdf also has a clustering on the left side. However, this is due to the fact that the lowest concentration can only be zero while the highest concentration has no upper limit.

The effect of extreme values on the total average flux is well illustrated in Fig. B.4. The noisy red solid lines in this figure plot the values of $uc * p(uc)$ and $vc * p(vc)$, including their signs. The cumulative sum (blue long dashed line) of these quantities give information of how the total fluxes were contributed

[1]This was caused by limitation of the hardware – only up to 400 digital images could be stored in the image acquisition system memory at a time and had to be downloaded before another 400 images could be acquired.

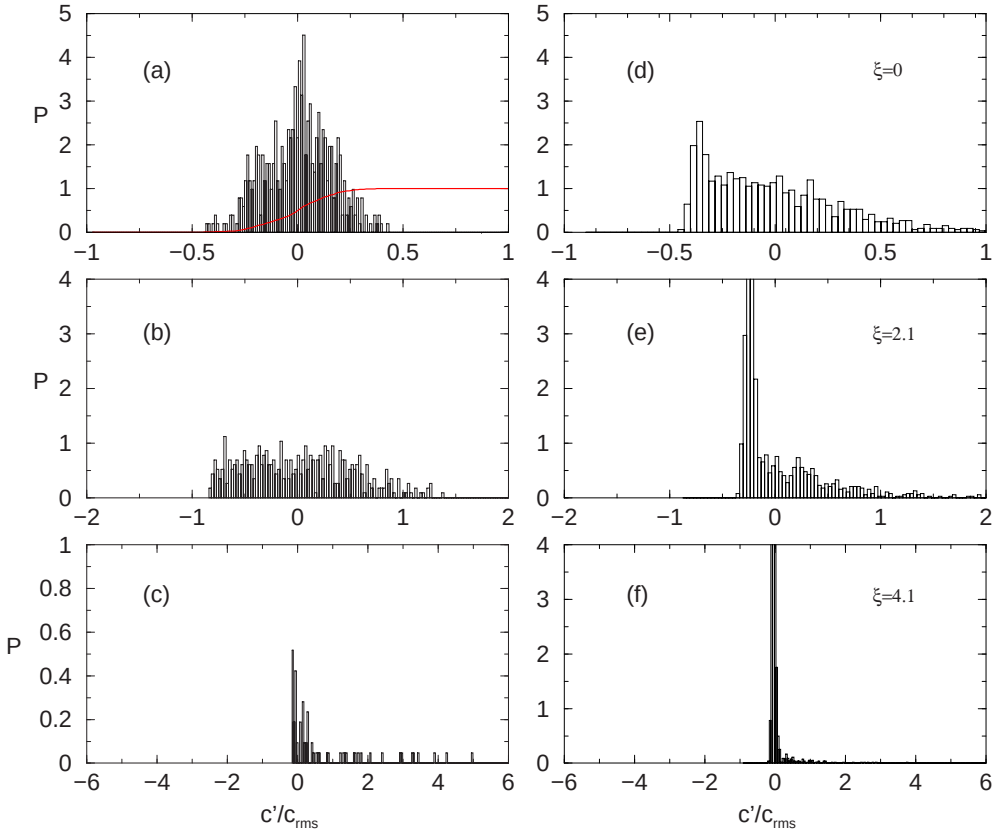

Figure B.3: Probability density function of the numerical (left column) and experimental (right column) concentration at three cross-stream locations. The solid line in (a) is the cumulative sum of the pdf. Center plane: (a) and (d); $\xi = 2.1$ (high-speed side): (b) and (e); $\xi = 4.1$ (high-speed side almost in free-stream): (c) and (f).

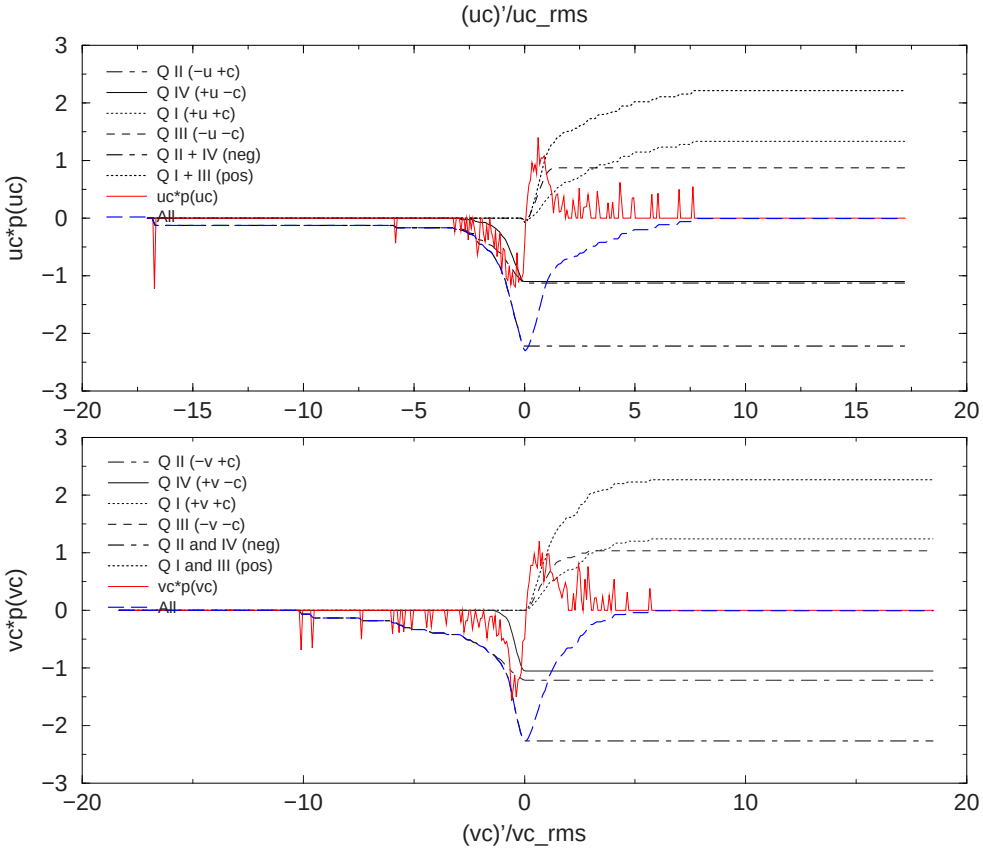

Figure B.4: Effect of extreme values on the total flux. Low-speed side position at $\xi = -2.2$. The cumulative sum of the weighted probably density function shows how the total flux converges. By further breaking down the data set into quadrants, the contribution from each quadrant to the total flux is shown.

by each individual element in the data set. The blue curves converge to the total flux values at right side, and the total flux value is quite close to zero. At the left side of the $uc * p(uc)$ curve, there is one extreme value captured by the experiment. From the cumulative curve it can be seen that this single data point itself brings down the total flux by a large amount. Because the sample size was small and the effect of the extreme values is quite significant, the total concentration flux results from present experimental study are subject to some degree of uncertainty. This is the major reason contributing to the abnormal distribution of the vc concentration flux profile in Fig. 4.9 on the low-speed side and to the general lack of smoothness of the data.

As a byproduct of the analysis shown in Fig. B.4, by further breaking down the data set into quadrants (according to the signs of the velocity and concentration fluctuations) and evaluating the contribution from each quadrant to the total flux, the octant analysis result in section 4.5 can be confirmed. For example, by looking at the uc case, one can see most of the positive extreme values are in quadrant I (+u,+c). This corresponds to the octant V event in the octant analysis, shown in Fig. 4.12, which indeed shows that octant V events occur rarely but have the highest intensity.

In summary, although part of the experimental scalar flux results suffer from errors stemming from the limitation of the image acquisition camera and the sample size, all the results are rationally explainable. Even though the magnitudes of the scalar fluxes are not completely reliable, they generally show the proper trends except on the low-speed side for vc. Furthermore, the scalar transport mechanisms discovered by the experimental conditional analysis were confirmed by the LES.

Recall that the non-zero concentration rms at the free-stream in Fig. 4.5 is the rms of the varying camera background grey level. It should be mentioned that this background affected the concentration statistics more in the free-stream toward the edges of the mixing layer than near the center plane. This is because the mean concentration is higher near the center of the mixing layer so that the number of concentration values truncated by the camera floor is fewer. To conclude this discussion, a more quantitative analysis of the camera resolution issue is documented here.

Suppose the camera floor grey scale is at i and is varying as $i \pm \epsilon$. The measured grey scale can then be written as:

$$I_{meas_1} = I_{true} \text{ if } I_{true} > i \pm \epsilon, \tag{B.1}$$

$$I_{meas_2} = i \pm \epsilon \text{ if } I_{true} \leq i \pm \epsilon. \tag{B.2}$$

Suppose also that there are N values above the floor and M values at or below the floor. Then the mean grey level can be written as:

$$\overline{I}_{meas} = \frac{1}{N+M}(\sum_1^N I_{meas_1} + \sum_1^M I_{meas_2}), \tag{B.3}$$

and the variance can be written as[2]:

$$\begin{aligned}
\overline{I'^2}_{meas} &= \frac{1}{N+M}(\sum_1^N I'^2_{meas_1} + \sum_1^M I'^2_{meas_2}) \\
&= \frac{1}{N+M}[\sum_1^N (I_{true} - \overline{I}_{meas})^2 + \sum_1^M (i \pm \epsilon - \overline{I}_{meas})^2] \\
&= \frac{1}{N+M}[\sum_1^N (I^2_{true} + 2I_{true}\overline{I}_{meas} + \overline{I}^2_{meas}) \\
&+ \sum_1^M (i^2 - 2i\overline{I}_{meas} + \epsilon^2 + \overline{I}^2_{meas})].
\end{aligned} \tag{B.4}$$

[2]In this step of the derivation, two cross-product terms are dropped by assuming that the variation of the camera background level follows a normal distribution.

If the camera has perfect resolution, i.e. $i \pm \epsilon = 0$, then the grey scale variance would be:

$$\overline{I'^2}_{meas} = \frac{1}{N+M}[I^2_{true} - 2I_{true}\overline{I}_{meas} + \overline{I}^2_{meas}]. \tag{B.5}$$

The difference between (B.4) and (B.5) is the error of the variance. It can be seen that at the center plane of the mixing layer, where the mean concentration reaches its maximum value and thus $N \gg M$, the error of the variance measurement is minimum. In Fig. 4.5 (f), the difference of concentration rms between the LES and the experiment is partly due to the camera background level discussed here and partly due to the much greater spatial resolution of the concentration field experimental measurements compared to the values obtained from the LES.

BIBLIOGRAPHY

[1] Akselvoll, K. and Moin, P., "Large-eddy simulation of turbulent confined coannular jets and turbulent flow over a backword-facing step." *Report TF-63, Thermosciences Div.*, Dept. Mech. Eng., Stanford University, 1995

[2] Arnal, M. and Friedrich, R., "Large-eddy simulation of turbulent flow with separation." *Turbulent Shear Flows 8*, edited by F. Friedrich, R. Durst, B. E. Launder and F. W. Schmidt (Springer, Heidelberg), pp. 169, 1992

[3] Artale, V., Boffetta, G., Celani, A., Cencini M. and Vulpiani, A., "Dispersion of passive tracers in closed basins: beyond the diffusion coefficient." *Physics of Fluids*, vol. 9, No. 11, pp. 3162, 1997

[4] Ashurst, W. T. and Meiburg, E., "Three-dimensional shear layers via vortex dynamics." *Journal of Fluid Mechanics*, vol. 189, pp. 87, 1988

[5] Balachandar, S. and Maxey, M. R., "Methods for evaluating fluid velocities in spectral simulations of turbulence." *Journal of Computational Physics*, vol. 83, pp. 96, 1989

[6] Balaras, E., "Large eddy simulation of high Reynolds number wall bounded shear layers." *Ph.D. Dissertation, Swiss Federal Institute of Technology*, 1995

[7] Balaras, E., Piomelli, U. and Wallace, J. M., "Self-similar states in turbulent mixing layers" *Journal of Fluid Mechanics*, vol.446, pp. 1, 2001

[8] Balint, J. -L., Wallace, J. M. and Vukoslavcevic, P., "The statistical properties of the vorticity field of a two-stream turbulent mixing layer." *Advances in Turbulence 2*, edited by H. H. Fernholz and H. E. Feidler, Springer-Verlag, Berlin 1989

[9] Balint, J. -L., Wallace, J. M. and Vukoslavcevic, P., "The velocity and vorticity vector fields of a turbulent boundary layer. Part 2, Statistical properties." *Journal of Fluid Mechanics*, vol. 228, pp. 53, 1991

[10] Batchelor, G. K., "Small scale variation of convected quantities like temperature in turbulent fluid." *Journal of Fluid Mechanics*, vol. 5, pp. 113, 1959

[11] Bell, J. H. and Mehta, R. D., "Development of a two-stream mixing layer from tripped and untripped boundary layers." *AIAA Journal*, vol. 28, pp. 2034, 1990

[12] Bell, J. H. and Mehta, R. D., "Measurements of the streamwise vortical structures in a place mixing layer." *Journal of Fluid Mechanics*, vol. 239, pp. 213, 1992

[13] Bell, J. H., Plensniak, M. W. and Mehta, R. D., "Spanwise averaging of plane mixing layer properties." *AIAA Journal*, vol. 30, pp. 835, 1992

[14] Bernal, L. P. and Roshko, A., "Streamwise vortex structure on plane mixing layers." *Journal of Fluid Mechanics*, vol. 170, pp. 499, 1986

[15] Breidenthal, R., "Structure in turbulent mixing layers and wakes using a chemical reaction." *Journal of Fluid Mechanics*, vol. 109, pp. 1, 1981

[16] Broadwell, J. E. and Breidenthal, R. E., "A simple model of mixing and chemical reaction in a turbulent shear layer." *Journal of Fluid Mechanics*, vol. 125, pp. 397, 1982

[17] Browand, F. K. and Troutt, T. R., "A note on spanwise structure in the two-dimensional mixing layer." *Journal of Fluid Mechanics*, vol. 97, pp. 771, 1980

[18] Brown, G. L. and Roshko, A., "On density effects and large structure in the turbulent mixing layers." *Journal of Fluid Mechanics*, vol. 64, pp. 775, 1974

[19] Chandrsuda, A., Mehta, R. D., Weir, A. D. and Bradshaw, P., "Effect of free-stream turbulence on large structure in turbulent mixing layer." *Journal of Fluid Mechanics*, vol. 85, pp. 693, 1978

[20] Chiang, K. -F., "Dispersion of contaminant released from a line source at the wall of a turbulent boundary layer." *Ph.D. Dissertation, University of Maryland College Park*, 1999

[21] Comte, P., Silvestrini, J. H. and Begou, P., "Streamwise vortices in large-eddy simulations of mixing layer." *Eur. J. Mech. B/Fluids*, Vol. 17. pp. 615, 1998

[22] Corcos, G. M. and Sherman, F. S., "The mixing layer: deterministic models of a turbulent flow. Part 1. Introduction and the two-dimensional flow." *Journal of Fluid Mechanics*, vol. 139, pp. 29, 1984

[23] Corcos, G. M. and Lin. S. J., "The mixing layer: deterministic models of a turbulent flow. Part 2. The origin of the three-dimensional motion." *Journal of Fluid Mechanics*, vol. 139, pp. 67, 1984

[24] Dimotakis, P. E. and Brown, G. L., "The mixing layer at high Reynolds number: large-structure dynamics and entrainment." *Journal of Fluid Mechanics*, vol. 78, pp. 535, 1976

[25] Druault, Ph., Lardeau, S., Bonnet, J.-P., Coiffet, F., Largeau, J.-F. and Perret, L., "The generation of realistic 3D unsteady inlet conditions for LES." *AIAA journal*, vol. 41, 2003

[26] Germano, M., Piomelli, U., Moin, P. and Cabot, W. H., "A dynamic subgrid-scale eddy viscosity model." *Physics of Fluids A*, vol. 3, pp. 1760, 1991

[27] Ghoniem, A. F. and Heidarinejad, G., "Effect of Damkohler number on the reactive zone structure in a shear layer" *Combustion and Flame*, vol. 83, pp. 1, 1991

[28] Hernan, M. A. and Jimenez, J., "Computer analysis of a high-speed film if the plane mixing layer." *Journal of Fluid Mechanics*, vol. 119, pp. 323, 1982

[29] Ho, C. -M. and Huang, L. S., "Subharmonic and vortex merging in mixing layer." *Journal of Fluid Mechanics*, vol. 119, pp. 443, 1982

[30] Huai, X., Joslin, R. D. and Piomelli, U., "Large-eddy simulation of transition to turbulence in boundary layers." *Theoretical and Computational Fluid Dynamics*, vol. 9, pp. 149, 1997

[31] Jimenez, J., "A spanwise structure in the plan shear layer." *Journal of Fluid Mechanics*, vol. 132, pp. 319, 1983

[32] Jorgensen, F. E. "Directional Sensitivity of Wire and Fiber Film Probes." *DISA Inform.*, vol. 11, pp. 31, 1971

[33] Kaltenbach, H. J., Fatica, M., Mittal, R., Lund, T. S. and Moin, P., "Study of flow in a planar asymmetric diffuser using large-eddy simulation." *Journal of Fluid Mechanics*, vol. 390, pp. 151, 1999

[34] Koochesfahani, M., Cohn, R. and MacKinnon, C., "Simultaneous whole-field measurements of velocity and concentration fields using a combination of MTV and LIF" *Measurement Science and Technology*, vol. 11, pp. 1289, 2000

[35] Koochesfahani, M. M. and Dimotakis, P. E., "Laser-induced fluorescence measurements of mixed fluid concentration in a liquid plane shear layer." *AIAA Journal*, vol. 23, pp. 1700, 1985

[36] Koochesfahani, M. M. and Dimotakis, P. E., "Mixing and chemical reactions in a turbulent liquid mixing layer." *Journal of Fluid Mechanics*, vol. 170, pp. 83, 1986

[37] Lardeau, S. "Direct numerical simulation of free-shear flows controlled by fluid injection." *Ph.D. Dissertation, University of Poitiers*, 2001

[38] Lang, D. B., "Laser Doppler velocity and vorticity measurements in turbulent shear layer." *Ph.D. Dissertation, California Institute of Technology*, 1985

[39] Lasheras, J. C., Cho, J. S. and Maxworthy, T., "On the origin and evolution of streamwise vortical structures in a plane, free shear layer." *Journal of Fluid Mechanics*, vol. 172, pp. 231, 1986

[40] Le, H., Moin, P. and Kim, J., "Direct numerical simulation of turbulent flow over a backward-facing step." *Journal of Fluid Mechanics*, vol. 330, pp. 349, 1997

[41] Lee, S., Lele, S. K. and Moin, P., "Simulation of spatially evolving turbulence and the applicability of Taylor's hypothesis in compressible flow." *Phys. Fluid A*, vol. 4, pp. 1521, 1992

[42] Li, N., Balaras, E. and Piomelli, U., "Inflow conditions for large-eddy simulations of mixing layer." *Physics of Fluids*, vol. 12, No. 4, pp. 935, 2000

[43] Liu, J., Piomelli, U. and Spalart, P. R., "Interaction between a spatially growing turbulent boundary layer and embedded streamwise vortices." *Journal of Fluid Mechanics*, vol. 326, pp. 151, 1996

[44] Lilly, D. K., "A proposed modification of the Germano subgrid-scale closure method." *Physics of Fluids A*, vol. 4, pp. 633, 1992

[45] Loucks, R. B. "An experimental examination of the velocity and vorticity fields in a plane mixing layer." *Ph.D. Dissertation, University of Maryland College Park*, 1998

[46] Lund, T. S., Wu, X. and Squires, K. D., "Generation of inflow data for spatially-developing boundary layer simulations." *Journal of Computational Physics*, vol. 140, pp. 233, 1998

[47] Meneveau, C., Lund, T. S. and Cabot, W. H., "A Lagrangian dynamic subgrid-scale model of turbulence." *Journal of Fluid Mechanics*. vol. 319, pp. 353, 1996

[48] Moser, R. D. and Rogers, M. M, "Mixing transition and the cascade to small scales in a plane mixing layer." *Physics of Fluid and Fluid Dynamics*, vol. 3, pp. 1128, 1991

[49] Moser, R. D. and Rogers, M. M, "The three-dimensional evolution of a plane mixing layer: pairing and transition to turbulence." *Journal of Fluid Mechanics*. vol. 247, pp. 275, 1993

[50] Murman, E. M. and Powell, K. G., "Trajectory integration in vortical flows." *AIAA Journal*, vol. 27, pp. 982, 1989

[51] Nguyen, P. N., "Simultaneous measurements of the velocity and vorticity fields in the turbulrnt near wake of a circular cylinder." *Ph.D. Dissertation, University of Maryland College Park*, 1993

[52] Orlanski, I., "A simple boundary condition for unbounded hyperbolic flows." *Journal of Computational Physics*, vol. 21, pp. 251, 1976

[53] Ong, L., "Visualization of turbulent flows with simultaneous velocity and vorticity measurements." *Ph.D. Dissertation, University of Maryland College Park*, 1992

[54] Pickett, L.M. and Ghandhi, J.B., "Passive scalar measurements in a planar mixing layer by PLIF of acetone" *Experiments in Fluids*, vol. 31, no. 3, pp. 309, 2001

[55] Pickett, L.M. and Ghandhi, J.B., "Passive scalar mixing in a planar shear layer with laminar and turbulent inlet conditions" *Physics of Fluids*, vol. 14, pp. 985, 2002

[56] Piomelli, U., Balint, J. -L. and Wallace, J. M., "On the validity of Taylor's hypothesis for wall-bounded turbulent flows.", *Physics of Fluids*, vol. 1, pp. 365, 1989

[57] Rai, M. M. and Moin, P., "Direct numerical simulation of transition and turbulence in a spatially evolving boundary layer." *Journal of Computational Physics*, vol. 109, pp. 169, 1993

[58] Reynolds, W. C., "The potential and limitation of direct and large eddy simulations" *Lecture notes in physics*357, Springer, pp. 313, 1990

[59] Riley, J. J. and Metcalf, R. W., "Direct numerical simulation of perturbed mixing layer." *AIAA Paper* 80-0274, 1980.

[60] Robinson, S. K., "The kinematics of turbulent boundary layer structure." *NASA TM-103859*, 1991

[61] Rogers, M. M and Moser, R. D., "The three-dimensional evolution of a plane mixing layer: the Kelvin-Helmhoitz rollup." *Journal of Fluid Mechanics*. vol. 243, pp. 183, 1992

[62] Rogers, M. M and Moser, R. D., "Direct simulation of a self-similar turbulent mixing layer." *Physics of Fluids* , vol. 6, pp. 903, 1994

[63] Sarghini, F., Piomelli, U. and Balaras E., "Scale-similar models for large-eddy simulations." *Physics of Fluids*, vol. 11, pp. 1596, 1999

[64] Shraiman, B.I. and Siggia, E.D., "Scalar turbulence." *Nature*, vol. 405, No. 6787, pp. 639, 2000

[65] Smagorinsky, J., "General circulation experiments with the primitive equations. I. The basic experiment." *Mon. Weather Rev.*, vol. 91, pp. 99, 1963

[66] Sotiropoulos, F., Ventikos, Y. and Lackey, T.C., "Chaotic advection in three-dimensional stationary vortex-breakdown bubbles: Sil'niltov's chaos and the devil's staircase." *Journal of Fluid Mechanics*, vol. 444, pp. 257, 2001

[67] Spalart, P. R., "Numerical study of sink-flow boundary layers." *Journal of Fluid Mechanics*, vol. 172, pp. 307, 1986

[68] Spalart, P. R., "Direct simulation of a turbulent boundary layer up to $R_\theta = 1410$." *Journal of Fluid Mechanics*, vol. 187, pp. 61, 1988

[69] Spalart, P. R. and Watmuff, J. H., "Experimental and numerical study of a turbulent boundary layer with pressure gradients." *Journal of Fluid Mechanics*, vol. 249, pp. 337, 1993

[70] Spalart, P. R. and Yang, K. S., "Numerical simulation of ribbon-induced transition in Blasius flow." *Journal of Fluid Mechanics*, vol. 187, pp. 61, 1987

[71] Stoer, J. and Bulirsch, R., "Introduction to Numerical Analysis" *Springer-Verlag*, New York, 1980

[72] Van Driest, E. R., "On the turbulent flow near a wall." *J. Aeronaut. Sci.*, vol. 23, pp. 1007, 1956

[73] Vincont, J. -Y., Simoens, S., Ayrault, M. and Wallace, J. M., "Passive scalar dispersion in a turbulent boundary layer from a line source at the wall and downstream of an obstacle." *Journal of Fluid Mechanics*, vol. 424, pp. 127, 2000

[74] Vreman, B., Geurts, B. and Kuerten, H., "Large-eddy simulation of the turbulent mixing layer" *Journal of Fluid Mechanics*, vol.339, pp.357, 1997

[75] Vukoslavcevic, P., Wallace, J. M. and Balint, J. -L., "The velocity and vorticity field of a turbulent boundary layer. Part1. Simutaneous measurement by hot-wire anemometry." *Journal of Fluid Mechanics*, vol. 228, pp. 25, 1991

[76] Vukoslavcevic, P., Wallace, J. M., "A 12-sensor hot-wire probe to measure the velocity and vorticity vectors in turbulent flow." *Measurement Science and Technology*, vol. 7, pp. 1451, 1996

[77] Wallace, J. M., Eckelmann, H. and Brodkey, R. S., "The wall region in turbulent shear flow." *Journal of Fluid Mechanics*, vol. 54, pp. 39, 1972

[78] Wang, Q., Squires, K. D. and Wu, X., "Lagrangian statistics in turbulent channel flow." *Atmospheric Environment*, vol. 29, pp. 2417, 1995

[79] Winant, C. D. and Browand, F. K., "Vortex pairing: the mechanism of turbulent mixing-layer growth at moderate Reynolds number." *Journal of Fluid Mechanics*, vol. 63, pp. 237, 1974